NTNU
Norwegian University of
Science and Technology

Electric Control of Skyrmion Dynamics and Spin Torque Oscillators in Magnetic Materials with Inversion Asymmetry

Øyvind Johansen

Master of Science in Physics and Mathematics
Submission date: June 2016
Supervisor: Jacob Rune Wüsthoff Linder, IFY

Norwegian University of Science and Technology
Department of Physics

Abstract

In this thesis the skyrmion velocity in the presence of spin-transfer torques, Rashba spin–orbit coupling and a constant electric field gradient is derived analytically based on a collective coordinate approach in the Thiele formalism. This analytical result is also derived in the presence of a phenomenological pinning force. The results show that the spin–orbit coupling can be effectively considered as a modification of the non-adiabatic spin-transfer torque. The electric field gradient causes a motion of the skyrmion along equipotential lines, in addition to a damped motion in the opposite direction of the gradient to a lower energy state. The analytical calculations are compared to a full numerical solution of the Landau–Lifshitz–Gilbert equation. We also study the effects of Rashba spin–orbit coupling on magnetic multilayer spin torque oscillators. It is discovered that the spin–orbit coupling can be compared to a modification of the Gilbert damping, to the extent that we can get an anti-damping term in the Landau–Lifshitz–Gilbert–Slonczewski equation. This anti-damping term can help destabilize collinear states, and increase the size of the oscillating phase. Moreover, we find an oscillating phase in both ferromagnetically and antiferromagnetically coupled magnetic moments, where the moments are of equal magnitude, which is a new result. The Rashba spin–orbit coupling also allows for a wider tunability of frequency spectra of the spin torque oscillators.

Samandrag

I denne masteroppgåva er skyrmionhastigheita i nærvær av spinnoverførande dreiemoment, Rashba spinn-bane-kopling og ein konstant elektrisk feltgradient utleda analytisk basert på ein kollektiv koordinattilnærming i Thiele-formalismen. Dette analytiske resultatet er også utleda i nærvær av ein fenomenologisk låsingkraft. Resultata visar at spinn-bane-koplinga kan effektivt bli sett på som ein modifisering av det ikkje-adiabatiske spinnoverførande dreiemomentet. Den elektriske feltgradienten førar til ei rørsle av skyrmionet langs ekvipotensiallinjar, i tillegg til ei dempa rørsle i motsatt retning av gradienten til ei lågare energitilstand. Dei analytiske utrekningane er samanlikna med ei full numerisk løysing av Landau–Lifshitz–Gilbert likninga. Vi studerar også effektane av Rashba spinn-bane-kopling på magnetiske fleirlags spinn-dreiemoment-oscillatorar. Det er oppdaga at spinn-bane-koplinga kan bli samanlikna med ei modifisering av Gilbert dempinga, i den grad at vi kan få eit antidempingsledd i Landau–Lifshitz–Gilbert–Slonczewski likninga. Dette antidempingsleddet kan hjelpe til å destabilisera kollineære tilstandar, og auke storleiken til den oscillerande fasen. Dessuten finn vi ein oscillerande fase i både ferromagnetiske og antiferromagnetiske kobla magnetiske moment, der momenta er av lik storleik, som er eit nytt resultat. Rashba spinn-bane-koplinga tillatar også ein større tunbarheit av frekvensspektruma til spinn-dreiemoment-oscillatorane.

Preface

This thesis on quantum condensed matter theory is the end result of a five year integrated master programme in Applied Physics and Mathematics at the Norwegian University of Science and Technology.

I would like to thank my supervisor Prof. Jacob Linder for excellent guidance. His insight into the field of quantum condensed matter theory and ability to find unexplored topics of interest have been extremely valuable to this thesis. I would also like to thank Jabir Ali Ouassou for helpful discussions and information concerning numerical simulations. Finally, I would like to thank my parents, sisters and fellow classmates for their support.

Øyvind Johansen
Trondheim, Norway
June 2016

Contents

1

Introduction

Most of the technological devices we use in our daily lives today are based on electronics, where we utilize the charge of the electron to transfer and process information. In recent decades an alternative to electronics has emerged, and its name is spintronics. Spintronic devices utilize the spin of the electron instead of its charge. These devices have several advantages over electronic devices, such as a lower power consumption and that the materials needed to realize the devices are fairly common metals [1], whereas electronic devices need rarer semiconductor materials to function. Spintronic devices are widely used in non-volatile memory applications, such as magnetoresistive random access memory (MRAM) [2, 3], racetrack memories [4] and spin-transfer torque magnetic random access memory (STT-MRAM) [5]. Most of these applications are based on the giant magnetoresistance effect (GMR), which is that the resistance of a spin-polarized electrical current passing through a magnetic multilayer system is dependent on the orientation of the magnetic layers. When the magnetic moments of the different layers are anti-aligned the resistance of the current passing through the layers is much greater than the resistance of a current passing through magnetic layers with aligned magnetic moments. The discovery of this effect by Fert [6] and Grünberg [7] in 1988 was awarded by the Nobel prize in physics in 2007. This effect makes it possible to use magnetic multilayers for information storage in the form of bits, as we have a high-resistance and a low-resistance state, which can be assigned to the values zero and one. In addition, this information is not necessarily lost in the absence of an applied electric current or magnetic field, as the magnetic layers can keep their orientation in an equilibrium state. This makes the spintronic devices particularly interesting for non-volatile memory applications.

While the prospect of storing information in magnetic systems is interesting in its own right, we also need to be able to read and write the information effectively. This is where magnetization dynamics comes into play, a topic that this thesis will mainly revolve around. While it is known that magnetic moments can be manipulated by magnetic fields, this method is often impractical for nano-scale devices due to the large fields required to manipulate the magnetic moments in a very localized region. It has been discovered, however, that the magnetization in a magnetic material can also be manipulated by electrical means. An experiment by Johnson and Silsbee in 1985 showed that the spin

direction of the electrons in a current passing through a magnetic layer was aligned with the magnetic moment in the layer [8]. The magnetization in the film must therefore have exerted a torque on the spins of the conduction electrons. It is then reasonable to think that the spins of the conduction electrons will also exert a torque on the magnetization in the magnetic layer. This was shown theoretically by Berger [9, 10, 11, 12] and Sloncewski [13], and later observed experimentally [14]. This torque, known as the spin-transfer torque, could be used to switch the magnetization direction of one of the magnetic layers in a multilayer system [15, 16, 17]. It is therefore a very useful mechanism in writing techniques in spintronic devices.

Spin-transfer torques have also been shown to induce a translational motion of magnetic textures, such as domain wall motion [18, 19]. This is very useful in information processing, as we can move the information encoded in magnetic domains without any motion of physical components. This is utilized in racetrack memories [4]. This motion of magnetic textures is not without problems, however. Ideally we would move these magnetic textures in a purely translational manner, but above some critical current strength the motion of magnetic domain walls has been shown to undergo a Walker breakdown [20]. This Walker breakdown is an excitation of a different type of dynamics of the domain wall, in the form of rotational motion. In addition, at the current density needed to move domain walls Joule heating becomes a concern [21], causing energy loss to heat generation and thermal effects in the domain wall motion. Another magnetic texture known as the magnetic skyrmion has been of considerable interest lately, however. This is due to the fact that the critical current necessary to move them has been shown to be as low as 10^6 A/m^2 [22, 23, 24], whereas domain walls have a critical current in the range $10^{10} - 10^{12}$ A/m^2 [25, 4]. This makes it possible to move them without considerable effects from Joule heating. In multiferroic materials it is even possible to create skyrmion based memory devices without any Joule heating effects at all [26], as they can be controlled by electric fields via coupling to the electric dipole moment of the skyrmion. The dynamics of skyrmions has also been shown to be controllable by electric fields even in ferromagnetic materials [27]. Skyrmions are topologically stable objects, meaning they are also suitable for non-volatile memory applications. They are also of particular interest due to their ability for an extremely dense storage of information [28], as a single skyrmion can span just a few nanometers. In addition, methods that would make it possible to nucleate skyrmions by injection of a spin-polarized current [29], spin-waves [30] or by applying mechanical stress [31] have been suggested. This ability to manipulate skyrmions makes them very attractive in memory applications. The downside of skyrmions with respect to magnetic domain walls is that the skyrmion velocities obtained so far are well below what is achievable with magnetic domain walls [28, 32].

A third use of the spin-transfer torque, in addition to magnetization switching and translation of magnetic textures, is the precession of magnetic moments it can induce in magnetic multilayer systems [33, 34, 35]. When the magnetic moments in a multilayer system precess with respect to one another, so the projection of one magnetic moment onto another varies in time, this will cause an oscillation in the resistance of a current passing through the system due to the giant magnetoresistance effect. A direct current passing through the multilayer system will then be transformed into an alternating current. Such a system with a self-sustained precession in the magnetic layers is known as a spin torque oscillator [36, 37]. These oscillators are able to generate a wide range of frequencies in the output signal, spanning the range of 100s of MHz to 100s of GHz [3, 36, 38]. In addition, the frequency obtained can easily be tuned by the strength of the applied current. This

type of self-sustained precession has been shown to occur in both ferromagnetically [39] and antiferromagnetically [40] coupled magnetic layers, although Ref. [39] was unable to reproduce the results of Ref. [40].

Both skyrmions and spin torque oscillators appear in systems with a broken inversion symmetry. Skyrmions appear in chiral magnets, while spin torque oscillators are based magnetic multilayer systems, which have a broken inversion symmetry at the interfaces of the different layers. When we have a system with broken inversion symmetry, Rashba spin–orbit coupling [41, 42] can arise and a current passing perpendicularly to the direction of the asymmetry will induce spin–orbit torques. This type of spin–orbit coupling has proven to cause interesting effects in many different areas [43], such as the appearance of an intrinsic spin Hall effect [44]. The spin–orbit coupling was also an important mechanism in the implementation of the spin field-effect transistor by Datta and Das [45]. One of the advantages of Rashba spin–orbit coupling is its ability to be modified by the application of an electric field via gate voltages [46, 47]. This way the strength of the inversion asymmetry can be controlled to some extent. A discovery that is of particular interest to us is that Rashba spin–orbit coupling can also contribute to magnetization switching and self-sustained oscillations in spin torque oscillators [48, 49].

In this thesis we will study the magnetization dynamics of a single skyrmion (which is driven by spin-transfer torques and inhomogenous electric fields) and spin torque oscillators, both in the presence of Rashba spin–orbit coupling. We first introduce the micromagnetic model and the Landau–Lifshitz–Gilbert equation as a foundation for our calculations. Before deriving the equations of motion for the skyrmion from the Thiele equation, we briefly discuss the structure, symmetries and dynamical properties of the skyrmion. The analytical solution of the Thiele equation is then compared to a full numerical solution of the Landau–Lifshitz–Gilbert equation. Lastly, we combine analytical and numerical calculations to find the spin torque oscillator state and its frequency spectrum based on the Landau–Lifshitz–Gilbert–Slonczewski equation.

2

The micromagnetic model

In this thesis we will base our work on the micromagnetic model. This model is a semi-classical theory that is conventionally used to describe both the equilibrium and dynamics of the magnetization in a material on a nanometer to micrometer length scale. This length scale is large enough to assume a continuum approximation, we can consider the magnetization as a smooth and continuously varying vector field in space, as it is greater than the typical atomic length scale. On this length scale it is also not necessary to do a full quantum mechanical treatment of the system, making it justifiable to primarily treat quantities as expectation values instead of operators. The length scale is small enough, however, to be able to successfully describe patterns in the magnetization that are observed in nature, such as magnetic domain walls and magnetic skyrmions. This model is also able to describe the motion of such magnetization patterns well, which makes it a highly attractive model in the field of magnetization dynamics.

2.1 Energy terms in micromagnetics

In conventional micromagnetics there are five contributions to the micromagnetic energy. These are the exchange energy, the anisotropic energy, the Zeeman energy, the demagnetization energy, and the magneto-elastic energy. Of these five energies we will only discuss the former three. The demagnetization energy is not considered as it is mainly dominant over larger length scales, and the length scale that we will primarily consider is on the nanometer length scale. The magneto-elastic energy is also neglected, as we will not consider elastic distortion of the lattice. We will, however, also consider energy contributions that are not included in conventional micromagnetics, such as the Ruderman–Kittel–Kasuya–Yosida interaction, Rashba spin–orbit coupling, the Dzyaloshinskii–Moriya interaction and pinning potentials. We will treat these energy contributions in the same manner, assuming a continuum model of the magnetization if applicable (the Ruderman–Kittel–Kasuya–Yosida interaction for example is an interaction between discrete magnetic moments, and a continuum model is therefore not suitable).

2.1.1   Exchange energy

Ferromagnetism occurs in materials where the spins tend to align with each other, and thereby being able to generate an observable magnetic field outside of the material. The mechanism behind this is the exchange interaction between the spins. In ferromagnetic materials the system can lower its energy by having parallel neighboring spins. This is described by the Heisenberg Hamiltonian,

$$H = -J \sum_{\langle i,j \rangle} \boldsymbol{S}_i \cdot \boldsymbol{S}_j, \tag{2.1}$$

with J being the exchange integral which is positive for ferromagnetic materials and $\boldsymbol{S}$ a dimensionless spin-vector. The spins can be expressed in terms of the magnetization, which is the average magnetic moment. As the magnetic moment and the spin of an electron are anti-parallel, this relation becomes

$$\boldsymbol{S}_i = -\frac{S}{M_s} \boldsymbol{M}_i, \tag{2.2}$$

with M_s being the saturation magnetization and S the magnitude of the spin. The magnetization is a classical vector, and in micromagnetism it is treated as a slowly varying smooth function. One can therefore perform a Taylor expansion of it. By doing that, one can show [50] that the energy density can be written as

$$\epsilon_{\text{EX}} = \frac{\mathrm{d}E_{\text{EX}}}{\mathrm{d}V} = -\frac{A}{M_s^2} \boldsymbol{M}(\boldsymbol{r}) \nabla^2 \boldsymbol{M}(\boldsymbol{r}) = \frac{A}{M_s^2} \partial_i \boldsymbol{M}(\boldsymbol{r}) \partial_i \boldsymbol{M}(\boldsymbol{r}), \tag{2.3}$$

with A being the exchange stiffness

$$A = \frac{JS^2}{2a} \tag{2.4}$$

and a being the lattice constant.

2.1.2   Zeeman energy

When turning on an external magnetic field in a magnetic material, the magnetic moments in the material tend to align with the magnetic field. This is due to the Zeeman interaction, which will go to a lower energy state if the magnetic moments and external field are aligned. The Zeeman interaction energy density is given by

$$\epsilon_{\text{Z}} = -\mu_0 \boldsymbol{M} \cdot \boldsymbol{H}_{\text{Z}}, \tag{2.5}$$

with $\boldsymbol{H}_{\text{Z}}$ being the external magnetic field.

2.1.3   Perpendicular magnetic anisotropy

In some magnetic materials we may have something known as magnetic anisotropy. As the name indicates, there is an anisotropy in the material that makes certain magnetization directions more energetically favorable than others. This mostly stems from the spin–orbit coupling. If one considers the rest frame of the electron instead of the proton, the proton is orbiting the electron and thereby causing a temporally varying electric field. Ampère's

circuital law then says that the electron observes a magnetic field proportional to the orbital motion of the proton. This magnetic field then interacts with the magnetic moment (proportional to the spin) of the electron like in the Zeeman interaction, except here due to internal fields, hence the name spin–orbit coupling. Taking this into consideration as well as the atomic structure in the material, one can see that one could end up with a material where the magnetic field the electrons experience from the spin–orbit coupling would allow one direction to be easier magnetized than others.

In some layered ultrathin film structures, such as Pd/Co [51], it has been discovered that the magnetization has a lower energy when it is perpendicular to the films. This means that the easy axis of the material is perpendicular to the films, and we then have something called perpendicular magnetic anisotropy (PMA). The anisotropic energy is independent of the direction the magnetization has along the easy axis, meaning the energy is the same if the magnetization points into or out of the films. Letting K be the anisotropy constant and θ the angle to the normal of the films, the anisotropic energy density can then be written as

$$\epsilon_{\mathrm{PMA}} = K \sin^2 \theta \tag{2.6}$$

to the lowest order in θ. Here we have normalized the energy density in such a way that if the magnetization points along the easy axis the energy density is zero.

2.1.4   Voltage induced magnetic anisotropy

One form of perpendicular magnetic anisotropy occurs at the interface between certain materials. This has been attributed to the exchange interaction between p- and d-oribitals at material interfaces, such as the $3d$ orbital in Fe and $2p$ orbital in O at an Fe/MgO interface [52]. As this is a magnetic anisotropy that only occurs at the surface of the material, it will only be of importance in ultra-thin magnetic films where surface effects are of a greater importance. It has also been discovered that one can modify the strength of this surface magnetic anisotropy with an external electric field. The reason for the change of strength in the magnetic anisotropy is the modification of the occupation number in the $3d$ orbitals in Fe, thereby affecting the p-d exchange interaction that is the origin of the magnetic surface anisotropy [53]. It was found that in a thin-film system with an Fe/MgO interface where the Fe layer consisted of only a few monoatomic layers a change of approximately 40% could be achieved in the magnetic surface anisotropy by application of an external electric field. As it is relatively easy to generate a localized electric field, one can therefore create an energy landscape to influence the dynamics of magnetization patterns. An example of this was shown by Upadhyaya *et al.* by guiding dipole-dipole interaction skyrmions with voltage gates [27].

As the voltage induced magnetic anisotropy behaves as PMA, the energy density must then have the same form as that of ϵ_{PMA} in (2.6) and be dependent on the electric field. If one assumes that the modification of the electric field on the PMA is linear in the electric field, the energy density can be written as

$$\epsilon_{\mathrm{EF}} = \eta E(\boldsymbol{r}) \sin^2 \theta, \tag{2.7}$$

where η is a materialistic constant describing the strength of the modification of PMA by the electric field, and the electric field strength $E(\boldsymbol{r})$ is the z-component of the electric field as a function of position in the thin film.

2.1.5 Ruderman–Kittel–Kasuya–Yosida interaction

In metals, there is also another type of exchange interaction between magnetic moments in addition to the one described in Section 2.1.1. This interaction between nuclear magnetic moments is an indirect interaction. First a conduction electron in the atom interacts with the nuclear magnetic moment (proportional to its spin) through the hyperfine interaction. The hyperfine interaction is similar to the spin–orbit coupling discussed in Section 2.1.3. Instead of being in the rest frame of the electron, however, we consider the magnetic field seen in the rest frame of the nucleus due to the orbital motion of the electron. In addition, as the electron carries with it an intrinsic magnetic moment, it will generate a magnetic field that will interact with the spin of the nucleus. In short, the hyperfine interaction consists of spin–orbit and spin–spin interactions seen from the rest frame of the nucleus. Going back to the conduction electron that has interacted with the nuclear magnetic moment through the hyperfine interaction, it can also interact with another nuclear magnetic moment after interacting with the first. It can therefore act as a mediating particle for the interaction between the magnetic moments of two different nuclei. This interaction is known as the Ruderman–Kittel–Kasuya–Yosida (RKKY) interaction [54, 55, 56, 57], and its Hamiltonian is given by

$$H_{\text{RKKY}} = \frac{\boldsymbol{I}_i \cdot \boldsymbol{I}_j}{4} \frac{|\Delta k_m k_m|^2 m^*}{(2\pi)^3 R_{ij}^4 \hbar^2} \left[2k_m R_{ij} \cos\left(2k_m R_{ij}\right) - \sin\left(2k_m R_{ij}\right) \right]. \tag{2.8}$$

Here $\boldsymbol{I}_i$ and $\boldsymbol{I}_j$ are the nuclear magnetic moments, R_{ij} the distance between the magnetic moments, k_m the wave number of the conduction electrons, m^* the effective mass of the electrons and $\Delta k_m k_m$ is a factor describing the strength of the hyperfine interaction. What is important to note here is that the RKKY Hamiltonian acts similarly to the exchange Hamiltonian (2.2) in a manner that it is a symmetric interaction between spins, and that the coupling strength between the spins is a function of distance. Moreover, unlike the exchange interaction, this function of distance can either be positive or negative depending on the value of $k_m R_{ij}$. This means that we can alter if two magnetic moments are ferromagnetically or antiferromagnetically coupled to each other by increasing or decreasing the distance between them. The way the interaction is formulated in (2.8) it is between two nuclear magnetic moments. However, the RKKY interaction can also occur in a multilayer system such as $F_1/N/F_2$ where F_i are thin uniformly magnetized magnetic metals and N is a non-magnetic metallic spacer, as shown by Parkin and Mauri in [58]. If one lets the magnetization in F_i be $\boldsymbol{M}_i$, the RKKY interaction energy in F_i can then be written as

$$H_{\text{RKKY}} = -\frac{J_{\text{RKKY}}(R_{ij})}{d_i M_s^2} \boldsymbol{M}_i \cdot \boldsymbol{M}_j, \tag{2.9}$$

with $J_{\text{RKKY}}(R_{ij})$ being the distance dependent coupling strength between the magnetic moments that can be both positive and negative, and d_i being the thickness of F_i. The magnetic layers will then have a ferromagnetic coupling when $J_{\text{RKKY}} > 0$ and an antiferromagnetic coupling when $J_{\text{RKKY}} < 0$.

2.1.6 The Rashba effect

In materials where the motion of the electrons is confined to a plane, and the inversion symmetry is broken along the axis perpendicular to that plane, there is a splitting of the

spin energy levels. Inversion symmetry can for example be broken at the interface between two materials [42]. The inversion asymmetry causes an electric field perpendicular to the plane of motion, as the gradient of the electrostatic potential becomes non-zero when inversion symmetry is broken ($V(\boldsymbol{r}) \neq V(-\boldsymbol{r})$). When particles move in an electric field, they experience a magnetic field which can be seen by performing a Lorentz transformation into the particles' restframe. This magnetic field is proportional to $\boldsymbol{v} \times \boldsymbol{E}$. Because of the magnetic field the energy levels become spin dependent, as the field couples to the spin. This is described by the Rashba Hamiltonian [41]

$$H_{\mathrm{R}} = \frac{\alpha_{\mathrm{R}}}{\hbar}\boldsymbol{\sigma} \cdot (\boldsymbol{p} \times \hat{\boldsymbol{n}}) = \alpha_{\mathrm{R}}(\boldsymbol{\sigma} \times \boldsymbol{k}) \cdot \hat{\boldsymbol{n}}. \tag{2.10}$$

Here α_{R} is the Rashba parameter, $\boldsymbol{p} = \hbar\boldsymbol{k}$ the momentum of the electrons, $\hat{\boldsymbol{n}}$ a unit vector perpendicular to the plane of motion (along the direction of broken inversion symmetry) and $\boldsymbol{\sigma}$ is a vector of the Pauli matrices. This can be seen as the magnetic field points along the direction $\boldsymbol{v} \times \boldsymbol{E}$, and as $\boldsymbol{p} \propto \boldsymbol{v}$ and $\boldsymbol{E}$ points along the direction of broken inversion symmetry given by $\hat{\boldsymbol{n}}$, the magnetic field therefore points along $\boldsymbol{p} \times \hat{\boldsymbol{n}}$. According to the Zeeman energy the energy should be then proportional to $\boldsymbol{\sigma} \cdot (\boldsymbol{p} \times \hat{\boldsymbol{n}})$, and this proportionality constant is given by α_{R}, the value of which contains the physics of the broken inversion symmetry. This effect is a form of spin–orbit interaction, as the spin of the electron ($\propto \boldsymbol{\sigma}$) interacts with its own motion ($\boldsymbol{v}$). This effect is therefore also called Rashba spin–orbit coupling (RSOC).

### 2.1.7 The Dzyaloshinskii–Moriya interaction

The Dzyaloshinskii–Moriya interaction (DMI) is an antisymmetric exchange coupling between spins, given by the Hamiltonian

$$H_{\mathrm{DM}} = \sum_{\langle i,j \rangle} \boldsymbol{D}_{ij} \cdot (\boldsymbol{S}_i \times \boldsymbol{S}_j). \tag{2.11}$$

This interaction only occurs in materials where the inversion symmetry is broken. The magnitude of $\boldsymbol{D}_{ij}$ depends on the material properties, and the direction of $\boldsymbol{D}_{ij}$ depends on the symmetry of the atomic structure in the material. Moriya showed [59] that if there is an n-fold axis (with $n \geq 2$) along the axis between the particles with spins $\boldsymbol{S}_i$ and $\boldsymbol{S}_j$, $\boldsymbol{D}_{ij}$ will be parallel to that axis. Using that in a Taylor expansion of (2.11), it can be shown [50] that the energy density becomes

$$\epsilon_{\mathrm{DM}}^{(\mathrm{bulk})} = \frac{D}{M_s^2}\boldsymbol{M} \cdot (\nabla \times \boldsymbol{M}). \tag{2.12}$$

On the other hand, if there is a mirror plane located at the center of the line between the particles with spins $\boldsymbol{S}_i$ and $\boldsymbol{S}_j$ that is perpendicular to the axis intersecting them, the vector $\boldsymbol{D}_{ij}$ lies in the mirror plane. In a more specific case where the interaction between the spins $\boldsymbol{S}_i$ and $\boldsymbol{S}_j$ is mediated by a third magnetic particle (different from the other two) located in the mirror plane, $\boldsymbol{D}_{ij}$ is perpendicular to the triangle spanned by the three particles as illustrated in Figure 2.1. We now assume that the magnetic particles with spins $\boldsymbol{S}_i$ and $\boldsymbol{S}_j$ are located in the xy-plane, and that the mediating magnetic particle of a different type lies above them. According to symmetry, the vector $\boldsymbol{D}_{ij}$ is then given by $\boldsymbol{D}_{ij} = D/a\hat{\boldsymbol{y}}$ if i and j are nearest neighbours in the x-direction, and $\boldsymbol{D}_{ij} = -D/a\hat{\boldsymbol{x}}$ if i and j are nearest neighbours in the y-direction. Here a is the lattice constant and D
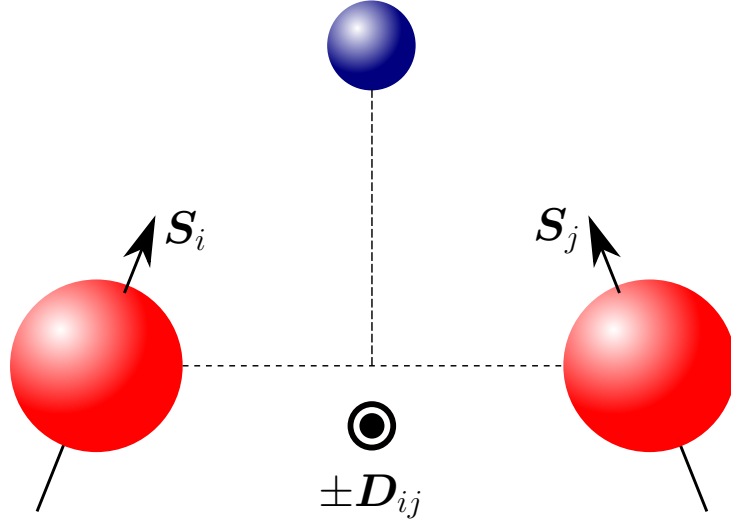
Figure 2.1. An illustration of the geometry of an interfacial DMI. The antisymmetric interaction between the spins $\boldsymbol{S}_i$ and $\boldsymbol{S}_j$ is mediated by a third magnetic particle in blue. The direction of $\boldsymbol{D}_{ij}$ is then perpendicular to the plane spanned by the three particles.

a constant that can be both positive and negative. We have for simplicity assumed an equal interaction in all directions in the xy-plane. Using this result, we explicitly derive the expression for the interfacial DMI energy density for reasons we will see in Section 3.2.2. As the spin can be written in terms of the magnetization as $\boldsymbol{S} = -\boldsymbol{M}S/M_s$, the Dzyaloshinskii–Moriya Hamiltonian can be written as

$$H_{\text{DM}} = \frac{1}{M_s^2} \sum_{\langle i,j \rangle} \boldsymbol{D}_{ij} \cdot (\boldsymbol{M}_i \times \boldsymbol{M}_j) \tag{2.13}$$

where the S^2 has been included in the magnitude of $\boldsymbol{D}_{ij}$. As mentioned earlier, we can do a Taylor expansion of the magnetization as it is a continious function in the micromagnetic model. To first order this Taylor expansion becomes

$$\boldsymbol{M}_{i+1} \approx \boldsymbol{M}_i + a\frac{\partial \boldsymbol{M}_i}{\partial x} \tag{2.14}$$

in the x-direction. An entirely equivalent expansion can also be done in the y-direction. The expansion in the z-direction is ignored as $\boldsymbol{D}_{ij}$ does not have a z-component. The energy density can then be calculated to be

$$
\begin{aligned}
\epsilon_{\text{DM}}^{\text{(interface)}} &= \frac{D}{M_s^2} \left[\hat{y} \cdot \left(\boldsymbol{M} \times \frac{\partial \boldsymbol{M}}{\partial x} \right) - \hat{x} \cdot \left(\boldsymbol{M} \times \frac{\partial \boldsymbol{M}}{\partial y} \right) \right] \\
&= \frac{D}{M_s^2} \left[\left(M_z \frac{\partial M_x}{\partial x} - M_x \frac{\partial M_z}{\partial x} \right) (\hat{\boldsymbol{y}} \cdot (\hat{\boldsymbol{z}} \times \hat{\boldsymbol{x}})) \right. \\
&\qquad \left. - \left(M_y \frac{\partial M_z}{\partial y} - M_z \frac{\partial M_y}{\partial y} \right) (\hat{\boldsymbol{x}} \cdot (\hat{\boldsymbol{y}} \times \hat{\boldsymbol{z}})) \right] \tag{2.15a} \\
&= \frac{D}{M_s^2} \left[M_z(\nabla \cdot \boldsymbol{M}) - (\boldsymbol{M} \cdot \nabla)M_z \right]. \tag{2.15b}
\end{aligned}
$$

The observant reader may have noticed that both the Rashba spin–orbit coupling and Dzyaloshinskii–Moriya interaction occur in materials with inversion asymmetry. Dzyaloshinskii first introduced DMI based on a phenemenological reasoning [60] to describe what had

been observed experimentally, and Moriya later proposed that the microscopic mechanism behind this was spin–orbit coupling [59]. In thin-film systems it is then reasonable to assume that Rashba spin–orbit coupling can be the mechanism behind DMI. This was in fact shown mathematically by Kim *et al.* [61]. They started with the model Hamiltonian

$$H = H_{\text{kin}} + H_{\text{R}} + H_{\text{EX}} = \frac{\boldsymbol{p}^2}{2m_e} + \frac{\alpha_{\text{R}}}{\hbar}\boldsymbol{\sigma} \cdot (\boldsymbol{p} \times \hat{\boldsymbol{n}}) + J\boldsymbol{\sigma} \cdot \hat{\boldsymbol{M}} \tag{2.16}$$

for the conduction electrons that includes the kinetic energy of electrons confined to a plane, a Rashba spin–orbit coupling and the symmetric exchange energy between the spins and the local magnetization. A unitary transformation was then performed on the Hamiltonian to remove the explicit Rashba Hamiltonian from the model, so that the transformed Hamiltonian could be written as $H' = U^{\dagger}HU = H_{\text{kin}} + H'_{\text{EX}} + \mathcal{O}(\alpha_{\text{R}}^2)$. This unitary transformation, defined by

$$U = \exp\left[-i\frac{\alpha_{\text{R}}m_e}{\hbar^2}\boldsymbol{\sigma} \cdot (\boldsymbol{r} \times \hat{\boldsymbol{n}})\right], \tag{2.17}$$

does not change the eigenvalues of the system, and the physics in the transformed Hamiltonian is therefore the same as the original model Hamiltonian. It was then shown that the transformation could be written as a rotation of the local magnetization. Plugging this transformed magnetization into the exchange energy density (2.3) in Section 2.1.1, an interfacial DMI term appears in addition to the symmetric exchange energy density. This DMI is characterized by an interaction strength D given by

$$D = \frac{4\alpha_{\text{R}}m_e A}{\hbar^2}. \tag{2.18}$$

2.1.8 Pinning potentials

With the exception of the RKKY interaction and voltage induced magnetic anisotropy, the free energy terms discussed so far are not explicitly dependent on position, but rather dependent on the magnetization profile $\boldsymbol{M}(\boldsymbol{r})$. If we were then to consider a system where the RKKY interaction and voltage induced magnetic anisotropy do not contribute to the free energy, and only the remaining energy terms discussed do, a given magnetization pattern $\boldsymbol{M}(\boldsymbol{r})$ will have the same free energy independent of where in the material it is localized. In other words, $\boldsymbol{M}(\boldsymbol{r})$ and $\boldsymbol{M}(\boldsymbol{r} - \boldsymbol{r}_0)$ have the same energy for any choice of $\boldsymbol{r}_0$. However, a realistic material will have impurities, and with the impurities local energy variations that are known as pinning centers appear. These pinning centers can make a certain position in the material for a magnetization pattern such as a domain wall or a magnetic skyrmion (which we will discuss in the next chapter) more energetically favorable to be localized. When considering the dynamics of magnetization patterns that are pinned in these pinning centers, one will need to supply a certain amount of energy for the magnetization pattern to move across the energy barrier that keeps the pattern localized in the pinning center [25, 4, 22]. There are several mechanisms that can cause these local energy variations to occur. In [62] Liu and Li proposed that by modifying the local density of itinerant electrons the exchange stiffness A and DMI strength D could become spatially dependent. When this is done the free energy becomes explicitly dependent on position, and due to the damping in the system any magnetization pattern will relax to its local minimum in the free energy. Another way to introduce pinning centers is to have spatial variations in the perpendicular magnetic anisotropy. This can

be realized by having notches in the surface of the magnetic material [29]. It is also possible to have pinning centers in the material by having a hole in the magnetic material [63], where for example certain atoms in a crystalline magnetic material are removed or replaced by non-magnetic atoms.

2.2 The Landau–Lifshitz–Gilbert equation

The key equation in the micromagnetic model is the Landau–Lifsthitz–Gilbert equation, which is based on the behavior of magnetic moments in magnetic fields. Magnetic moments are known to precess around magnetic fields when they are not perfectly aligned. This is known as Larmor precession. The magnetization in a magnet will therefore also perform Larmor precession, as the magnetization is the magnetic moment in a unit volume. This precession can be described by

$$\frac{\mathrm{d}\boldsymbol{M}}{\mathrm{d}t} = -\gamma \boldsymbol{M} \times \boldsymbol{H}, \tag{2.19}$$

where γ is the gyromagnetic ratio defined by

$$\gamma = \frac{g_e \mu_0 \mu_B}{\hbar} \tag{2.20}$$

where $g_e \approx 2$ is the g-factor, μ_0 the vacuum permeability and μ_B is the Bohr magneton. In addition to performing a precessing motion around the magnetic field, the magnetization will eventually relax parallel to the field to minimize the energy of the system. This can be modeled by introducing a damping term that is perpendicular to the magnetization and the precession of the magnetization. The precessional and damped precessional motions are illustrated in Figure 2.2. Originally Landau and Lifshitz proposed [64] a damping term of the form
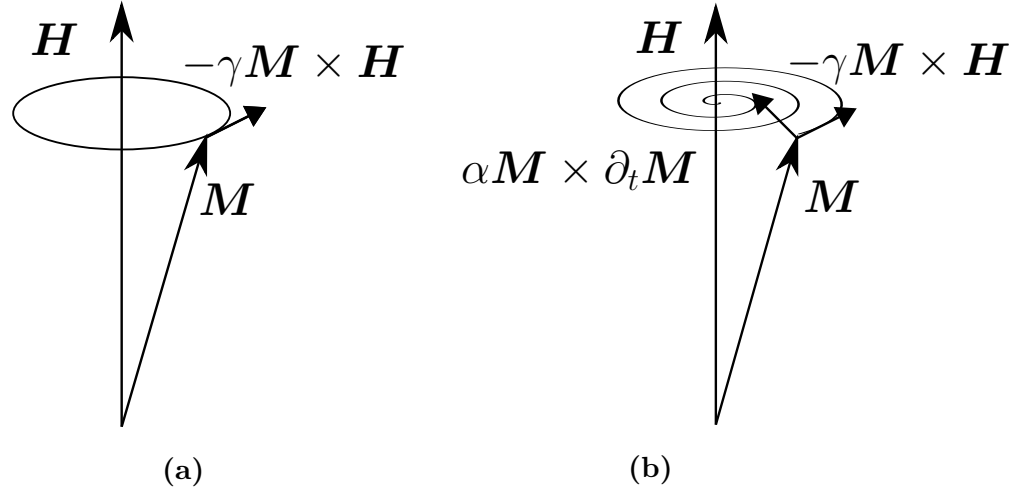
$$\frac{\mathrm{d}\boldsymbol{M}}{\mathrm{d}t} = -\gamma \boldsymbol{M} \times (\boldsymbol{H} + \frac{\alpha}{M_s} \boldsymbol{M} \times \boldsymbol{H}), \tag{2.21}$$

but it was discovered that this did not agree well with experiments in systems with a large damping parameter α. Therefore Gilbert proposed a damping term that included the time-derivative of the magnetization instead [65], which agreed much better with experiments [66], of the form

$$\frac{\mathrm{d}\boldsymbol{M}}{\mathrm{d}t} = -\gamma \boldsymbol{M} \times \boldsymbol{H} + \frac{\alpha}{M_s} \boldsymbol{M} \times \frac{\mathrm{d}\boldsymbol{M}}{\mathrm{d}t}. \tag{2.22}$$

This is known as the Landau–Lifshitz–Gilbert equation, and is the equation that governs the dynamics in the micromagnetic model. It should be noted that the magnetic field $\boldsymbol{H}$ that the magnetization precesses around is not only an external magnetic field applied to the system, but it is the effective magnetic field experienced locally by the magnetization. The direction of this magnetic field represents the direction in which the magnetization will have a minimum in the micromagnetic energy, and the effective field can therefore be written in terms of the micromagnetic energy. The effective field in the absence of an external field is given by

$$\begin{aligned} \boldsymbol{H}_{\text{eff}} &= -\frac{1}{\mu_0} \frac{\delta \epsilon[\boldsymbol{M}]}{\delta \boldsymbol{M}} \\ &= \frac{2A}{\mu_0 M_s} \nabla^2 \boldsymbol{m} + \frac{2(K + \eta E)}{\mu_0 M_s} m_z \hat{\boldsymbol{z}} + \frac{2D}{\mu_0 M_s} \left(\frac{\partial m_z}{\partial x} \hat{\boldsymbol{x}} + \frac{\partial m_z}{\partial y} \hat{\boldsymbol{y}} - (\nabla \cdot \boldsymbol{m}) \hat{\boldsymbol{z}} \right), \end{aligned} \tag{2.23}$$

Figure 2.2. The precession of the magnetization vector around a magnetic field. In **(a)** the precession is undamped and so the magnetization performs counter-clockwise circular rotations around the magnetic field. In **(b)** the damping component pointing towards the magnetic field causes a spiralling motion of the magnetization vector that eventually aligns the magnetization with the magnetic field.

with $\boldsymbol{m}$ being a unit vector in the direction of the magnetization. Here the symmetric exchange interaction, perpendicular and voltage induced magnetic anisotropy and interfacial DMI have been taken into consideration in the effective field.

Another thing to notice about the LLG equation is that only the direction of the magnetization $\boldsymbol{M}$ and not its magnitude changes with time. This can be seen by multiplying (2.22) by $\boldsymbol{M}$ from the left:

$$\boldsymbol{M} \cdot \frac{\mathrm{d}\boldsymbol{M}}{\mathrm{d}t} = \frac{1}{2}\frac{\mathrm{d}}{\mathrm{d}t}\boldsymbol{M}^2 = \boldsymbol{M} \cdot \left(-\gamma \boldsymbol{M} \times \boldsymbol{H} + \frac{\alpha}{M_s}\boldsymbol{M} \times \frac{\mathrm{d}\boldsymbol{M}}{\mathrm{d}t}\right) = 0. \qquad (2.24)$$

In other words the LLG equation conserves the magnitude of the magnetization, meaning $\frac{\mathrm{d}M_s}{\mathrm{d}t} = 0$.
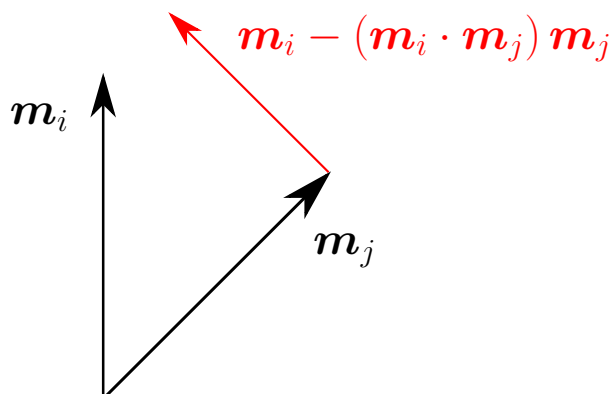
2.3 Spin-transfer torques

The LLG equation presented in (2.22) describes the dynamics of magnetic moments in the presence of external magnetic fields and internal effective fields that try to minimize the energy of the system. However, there are also other means of inducing dynamics of the magnetization in a material. The LLG equation can be extended to include these effects by adding torques to the right hand side of the equation (note that these torques will not have the same units as a mechanical torque, but the effect is well described by the term torque as it appears as a rotation of the magnetization direction). One method that has shown promise in inducing magnetization dynamics is the spin-transfer torque. In [9] Berger noted that when you apply a current through a magnetic domain wall, the main effect was not a scattering of the electrons, but that the domain wall tended to follow the motion of the electrons. When a spin-polarized current is passing through a magnetic material, the conduction electrons will want to align their magnetic moments with the local magnetization in the material to reduce their energy. The way the electrons reach a lower energy state is by the torque acting on them from the local magnetization due

to the fact that they are not aligned (or anti-aligned). Since the conduction electrons experience a torque when passing through a magnetization not parallel to their own magnetic moments, Newton's third law dictates that there must be an equal and opposite torque acting on the local magnetization. In other words, through a means of conserving angular momentum the conduction electrons transfer some of their spin to the local magnetization, hence the term spin-transfer torque (STT). Slonczewski introduced this torque in the LLG equation for the case of STT acting on a magnetic multilayer system [13]. This torque was observed experimentally a few years after the publications by Berger and Slonczewski [14, 15].

2.3.1   Adiabatic spin-transfer torque

To start the introduction of spin-transfer torques we will first discuss them qualitatively in what is known as the adiabatic regime. In this regime it is assumed that the magnetic moments of the conduction electrons passing through the magnetic material relaxes fast enough to always follow the local magnetization. If we then consider a current passing through a magnetic layer with a magnetization direction $\boldsymbol{m}_i = \boldsymbol{M}_i/M_s$, the magnetic moment of the electrons will be parallel to $\boldsymbol{m}_i$. Not long after passing through $\boldsymbol{m}_i$, the electrons pass through another magnetic material with a magnetization direction $\boldsymbol{m}_j$ which is tilted with respect to $\boldsymbol{m}_i$. Since the electrons have a magnetic moment that is not aligned with $\boldsymbol{m}_j$, this magnetization will lead to a torque acting on the conduction electrons to make their magnetic moments relax to be aligned with $\boldsymbol{m}_j$ instead of $\boldsymbol{m}_i$. As we mentioned earlier, there is then an equal torque acting on $\boldsymbol{m}_j$ in the opposite direction, attempting to align it with the magnetic moment of the electrons, which is $\boldsymbol{m}_i$ at the time of incidence. If we then assume that the magnitude of $\boldsymbol{M}_i$ and $\boldsymbol{M}_j$ are equal, the torque acting on $\boldsymbol{m}_j$ must then be proportional to the component of $\boldsymbol{m}_i$ which is perpendicular to $\boldsymbol{m}_j$. This means that the torque is proportional to $\boldsymbol{m}_i - (\boldsymbol{m}_i \cdot \boldsymbol{m}_j)\boldsymbol{m}_j$, as illustrated in Figure 2.3.

Figure 2.3. The adiabatic spin-transfer torque acting on a magnetic moment $\boldsymbol{m}_j$ from a spin-polarized current having passed through the magnetic moment $\boldsymbol{m}_i$ is proportional to the component of $\boldsymbol{m}_i$ perpendicular to $\boldsymbol{m}_j$.

This discussion was for two discrete magnetic moments. Let us now consider a case where the magnetization in a material varies slowly in a way that can be described by a function of position, such as a magnetic domain wall. We can still use the result from before, but instead of $\boldsymbol{m}_j$ being a magnetic moment in a direction independent of the direction of $\boldsymbol{m}_i$, there is only an infinitesimal change in $\boldsymbol{m}_j$ from $\boldsymbol{m}_i$. So when the

electrons arrive at the magnetization at a position $x+\mathrm{d}x$ (here assuming the electrons flow in the positive x-direction), their magnetic moments are aligned with the magnetization at the position x. Since the magnetization varies slowly, we can do a Taylor expansion to approximate the magnetization at position $x+\mathrm{d}x$ as a function of the magnetization at position x:

$$\boldsymbol{m}(x+\mathrm{d}x) \approx \boldsymbol{m}(x) + \mathrm{d}x\partial_x\boldsymbol{m}(x). \tag{2.25}$$

Typically $\mathrm{d}x$ would be on the length scale of the lattice constant. Using this expansion we can then find the direction of the torque acting on the magnetization at $x+\mathrm{d}x$ from the current which has a polarization along the magnetization at x:

$$
\begin{aligned}
&\boldsymbol{m}(x) - [\boldsymbol{m}(x) \cdot \boldsymbol{m}(x+\mathrm{d}x)]\,\boldsymbol{m}(x+\mathrm{d}x) \\
&\approx \boldsymbol{m}(x) - [1+\mathrm{d}x\boldsymbol{m}(x) \cdot \partial_x\boldsymbol{m}(x)]\,[\boldsymbol{m}(x)+\mathrm{d}x\partial_x\boldsymbol{m}(x)] \\
&= -\,\mathrm{d}x\partial_x\boldsymbol{m}(x).
\end{aligned}
\tag{2.26}
$$

Here we have used that $\boldsymbol{m}(x) \cdot \partial_x\boldsymbol{m}(x) = 0$ as the magnitude of $\boldsymbol{M}(x)$ is assumed to be constant for all positions. As we can see the result is somewhat different than for the two discrete magnetic moments as we have a differential in the torque, but the physical interpretation of the result is still the same. When the magnetic moments of the conduction electrons follow the local magnetization, their magnetic moment is adjusted from $\boldsymbol{m}(x)$ to $\boldsymbol{m}(x)+\mathrm{d}x\partial_x\boldsymbol{m}(x)$. The direction of the torque acting on the magnetization at $x+\mathrm{d}x$ must then be in the opposite direction of this change, along $-\mathrm{d}x\partial_x\boldsymbol{m}(x)$. Remember that what we have discussed so far has only been the direction of the torque acting on the local magnetization, and not its magnitude. A pre-factor must then be included that reflects how much spin is transferred from each electron to the local magnetization, the frequency of each electron passing through the magnetization, and how many of these electrons that are polarized of the magnetization at the previous position. Each electron has a magnetic moment $\boldsymbol{\mu} = \mu_B\boldsymbol{m}$, with $\boldsymbol{m}$ being a unit vector in the direction of the magnetization. The frequency of the electrons passing through the magnetization can be expressed in terms of the current, and since the magnetization is a volume average of the magnetic moments in the material, we want the current density to describe the rate of change to the magnetization. Letting the current passing through per cross-sectional area be j, the current density is j/d_j with d_j being the thickness of the material with magnetization $\boldsymbol{M}_j$. Assuming a portion P of the electrons in the current are polarized, the frequency of each electron transferring its magnetic moment to the magnetic material per volume unit is $jP/(-ed)$, where we have divided the current by its charge carrier. The adiabatic spin-transfer torque acting on a magnetization $\boldsymbol{M}_j$ after a current passing through a magnetization $\boldsymbol{M}_i$ is then

$$\boldsymbol{T}_{\mathrm{STT}}^{(\mathrm{adiabatic})} = -\frac{\mu_B jP}{ed_j}(\boldsymbol{m}_i - (\boldsymbol{m}_i \cdot \boldsymbol{m}_j)\boldsymbol{m}_j) = -\frac{\gamma\hbar jP}{2e\mu_0 d}\boldsymbol{m}_j \times (\boldsymbol{m}_i \times \boldsymbol{m}_j). \tag{2.27}$$

In a material with a slowly varying magnetization, the thickness of the magnetization goes from d_j to $\mathrm{d}x$. Using the expression found in (2.26) and that the current is moving in the direction $\hat{\boldsymbol{j}}$, the adiabatic STT in this case becomes

$$\boldsymbol{T}_{\mathrm{STT}}^{(\mathrm{adiabatic})} = \frac{\mu_B jP}{eM_s}(\hat{\boldsymbol{j}} \cdot \nabla)\boldsymbol{M}(\boldsymbol{r}). \tag{2.28}$$

These torques can then be included in the right hand side of the LLG equation in (2.22) to describe the dynamics of adiabatic STTs.

2.3.2 General spin-transfer torque

So far we have discussed how STT terms would appear in the LLG equation if the magnetic moments of the conduction electrons follow the local magnetization adiabatically. We will now derive the STT terms for a slowly varying magnetization more rigidly based on the spin continuity equation. This will be done for a more general case where the magnetic moments of the conduction electron can have a small component perpendicular to the local magnetization. This derivation mainly follows the derivation by Zhang and Li [67]. We start by considering the spin continuity equation. This is based on the continuity equation for an arbitrary quantity ρ,

$$\partial_t \rho + \nabla \hat{J}_\rho = 0, \tag{2.29}$$

with $\hat{J}_\rho$ being the current of the quantity ρ. This continuity equation assumes that the quantity ρ is conserved, but this is not the case for the spins in our system. The spins of the conduction electrons interact with the local magnetization, and in addition they can be scattered by the material. To reflect this we introduce sources and sinks on the right hand side of the continuity equation, so that it is given by

$$\partial_t \boldsymbol{s} + \nabla \hat{J} = \frac{1}{i\hbar} [\boldsymbol{s}, H_{sd}] - \boldsymbol{\Gamma}(\boldsymbol{s}). \tag{2.30}$$

Here $\boldsymbol{s}$ is the spin operator for the conduction electrons, $\hat{J}$ the spin-current operator, $\boldsymbol{\Gamma}(\boldsymbol{s})$ the relaxation rate of the conduction electrons due to scattering, and H_{sd} the s-d Hamiltonian

$$H_{sd} = -J_{\text{ex}} \boldsymbol{s} \cdot \boldsymbol{S} \tag{2.31}$$

which describes the (anti)ferromagnetic coupling between the itinerant spins $\boldsymbol{s}$ and local spins $\boldsymbol{S}$ depending on the sign of the coupling strength J_{ex}. In the micromagnetic model we are in a semi-classical limit, and we will therefore not treat the local spins quantum mechanically as operators, but as expectation values. The spins of the conduction electrons, however, we will still treat as operators for now. We proceed by calculating the commutator

$$[\boldsymbol{s}, H_{sd}]_i = -J_{\text{ex}} [s_i, s_j S_j] = -J_{\text{ex}} [s_i, s_j] S_j. \tag{2.32}$$

Here we assume the Einstein summation convention. Note that S_j can be pulled out of the commutators as it is not treated as an operator. The spin operators satisfy the commutation relation

$$[s_i, s_j] = i\hbar \varepsilon_{ijk} s_k, \tag{2.33}$$

which can be obtained from the Pauli matrix commutation relation as $s_i = \hbar \sigma_i / 2$. We then find that

$$\frac{1}{i\hbar} [\boldsymbol{s}, H_{sd}] = -J_{\text{ex}} \boldsymbol{S} \times \boldsymbol{s}. \tag{2.34}$$

From now on we will also treat the remaining operators as expectation values. We make the ansatz that the spin density $\boldsymbol{m}$ of the conduction electrons are mainly parallel to the local magnetization $\boldsymbol{M}$, but allow a small perpendicular component $\delta\boldsymbol{m}$:

$$\boldsymbol{m} = \langle \boldsymbol{s} \rangle = \frac{m_0}{M_s} \boldsymbol{M} + \delta\boldsymbol{m}. \tag{2.35}$$

Note here that the ratio m_0/M_s is very small, as the magnetization of the current is far below saturation. Moving on to the expectation value of the spin-current, we can write this as a tensor product between the velocity of the electrons, and their spin: $\langle \hat{J} \rangle = \boldsymbol{v} \otimes \boldsymbol{s}$. Instead of writing this expectation value in terms of the velocity $\boldsymbol{v}$ and spin $\boldsymbol{s}$, we want to write it in terms of the current density and magnetization. Using that $\boldsymbol{s} \approx \mu_B \boldsymbol{M}/M_s$ and following a similar approach as in the last section to rewrite the velocity in terms of the current j per unit area, we find that

$$\langle \hat{J} \rangle = -\frac{\mu_B P}{e M_s} \boldsymbol{j} \otimes \boldsymbol{M}. \tag{2.36}$$

Note that here we have assumed the spin current is adiabatic. To be exact one needs to include a non-adiabatic spin-current term $\delta \langle \hat{J} \rangle$, but it is assumed this is negligible. The product $\hat{\nabla} \langle \hat{J} \rangle$ in the spin continuity equation then becomes

$$\hat{\nabla} \langle \hat{J} \rangle = -\frac{\mu_B P}{e M_s} \left(\boldsymbol{j} \cdot \nabla \right) \boldsymbol{M} \tag{2.37}$$

when one assumes a uniform charge current density $\boldsymbol{j}$. Lastly, we approximate the relaxation rate due to scattering $\boldsymbol{\Gamma}(\boldsymbol{s})$ by the expectation value

$$\langle \boldsymbol{\Gamma}(\boldsymbol{s}) \rangle \approx \frac{\delta \boldsymbol{m}}{\tau_{\text{sf}}}, \tag{2.38}$$

with τ_{sf} being the spin-flip relaxation time. The spin continuity equation then becomes

$$\partial_t \boldsymbol{m} - \frac{\mu_B P}{e M_s} \left(\boldsymbol{j} \cdot \nabla \right) \boldsymbol{M} = -\frac{J_{\text{ex}} S}{M_s} \boldsymbol{m} \times \boldsymbol{M} - \frac{\delta \boldsymbol{m}}{\tau_{\text{sf}}} = -\frac{1}{\tau_{\text{ex}} M_s} \delta \boldsymbol{m} \times \boldsymbol{M} - \frac{\delta \boldsymbol{m}}{\tau_{\text{sf}}} \tag{2.39}$$

where we have introduced the spin relaxation $\tau_{\text{ex}} = (J_{\text{ex}} S)^{-1}$ time due to the exchange interaction. This is a time-scale that indicates how fast the spins of the conduction electrons align with the local spins, and this time-scale becomes smaller the stronger the exchange interaction ($\sim J_{\text{ex}}$) is. The first term appearing on the right hand side is a torque acting on the spin of the electrons due to an interaction with the local magnetization. As we have discussed earlier, Newton's third law then dictates that there must be an equal torque acting on $\boldsymbol{M}$ in the opposite direction, leaving us with the spin-transfer torque

$$\boldsymbol{T}_{\text{STT}} = \frac{1}{\tau_{\text{ex}} M_s} \delta \boldsymbol{m} \times \boldsymbol{M}. \tag{2.40}$$

To determine this torque we must first find $\delta \boldsymbol{m}$. We can do this based on (2.39), but first we find an expression for $\delta \boldsymbol{m} \times \boldsymbol{M}$, which we can obtain by taking the cross product of (2.39) with $\boldsymbol{M}$ from the right. We then find that

$$\delta \boldsymbol{m} \times \boldsymbol{M} = \tau_{\text{sf}} \left[\frac{m_0}{M_s} \boldsymbol{M} \times \partial_t \boldsymbol{M} - \frac{\mu_B P}{e M_s} \boldsymbol{M} \times (\boldsymbol{j} \cdot \nabla) \boldsymbol{M} + \frac{M_s}{\tau_{\text{ex}}} \delta \boldsymbol{m} \right] \tag{2.41}$$

where we have neglected the time derivative of $\delta \boldsymbol{m}$. Inserting the expression for $\delta \boldsymbol{m}$ from (2.39) into the expression above, we finally find that the total spin-transfer torque becomes

$$\boldsymbol{T}_{\text{STT}} = \frac{1}{1 + \beta^2} \left[\frac{\beta m_0}{M_s^2} \boldsymbol{M} \times \partial_t \boldsymbol{M} - \frac{m_0}{M_s} \partial_t \boldsymbol{M} + \frac{\mu_B P}{e M_s} (\boldsymbol{j} \cdot \nabla) \boldsymbol{M} - \frac{\beta \mu_B P}{e M_s^2} \boldsymbol{M} \times (\boldsymbol{j} \cdot \nabla) \boldsymbol{M} \right],$$
$$\tag{2.42}$$

where we have introduced the ratio $\beta = \tau_{\mathrm{ex}}/\tau_{\mathrm{sf}}$. The first two terms on the right hand side are on a form that already appear in the LLG equation, and introduce no new physics. In addition, they are proportional to m_0/M_s, and are therefore negligible. The third term we recognize being the adiabatic STT term in (2.28) that we found in the previous section, with an additional factor $(1 + \beta^2)^{-1}$. The last term is of particular interest, as it is on a form that we have not seen before. As we can see, the term is perpendicular to the adiabatic STT and contains an additional factor β. In the adiabatic regime, which we considered in the previous section, $\beta \to 0$ as the spin-flip relaxation time is much greater than the exchange relaxation time when the conduction electrons follow the local magnetization adiabatically. The last term therefore only appears when we are not in the adiabatic regime, and is therefore called the non-adiabatic STT. This torque, which is caused by the magnetic moments of the itinerant electrons that are not aligned with the local magnetization, will twist the magnetization out of the plane spanned by the magnetization in that area.

3

Skyrmions: symmetries and dynamics

The micromagnetic model introduced in the previous chapter is able to describe many different magnetization patterns that are static solutions of the LLG equation, one of them being magnetic skyrmions which we will introduce in this chapter. Here we will discuss their topology, what mechanisms are needed to stabilize them, and symmetry considerations of both the skyrmion profile and the LLG equation. Moreover, we will introduce the Thiele equation, which is a simplification of the LLG equation under the ansatz that the skyrmion moves rigidly. The Thiele equation is an algebraic vector equation in the velocity components of the skyrmion, making it much easier to solve than the LLG equation which is a partial differential equation. We also touch upon the subject of Berry phases and the topological Hall effect to describe some of the dynamical properties of skyrmions, but save the full analytical and numerical solution of the skyrmion velocity for Chapter 4.

3.1 Skyrmions

In certain types of materials, such as chiral magnets, an exotic magnetization pattern has been found to occur. This magnetization pattern, known as a skyrmion, is a vortex-like magnetization structure with non-trivial topology. The term skyrmion originates from the physicist Tony Skyrme, who described baryons and mesons as topological solitons [68]. While Skyrme had nothing to do directly with magnetic skyrmions, which we consider in this thesis, his name was used because the skyrmion has a non-trivial topology and is therefore also a topological soliton. By a non-trivial topology we mean that the magnetization of the skyrmion wraps around the unit sphere, so that it has a non-zero skyrmion number [69]

$$N_{\mathrm{sk}} = \frac{1}{4\pi} \int \hat{\boldsymbol{M}} \cdot (\partial_x \hat{\boldsymbol{M}} \times \partial_y \hat{\boldsymbol{M}}) \, \mathrm{d}x \, \mathrm{d}y. \tag{3.1}$$

Skyrmions have an integer skyrmion number, while vortices have a half-integer skyrmion number [70]. Skyrmions have been of particular interest in recent time, they were only first observed experimentally in 2009 [71]. The reason for the interest for magnetic skyrmions

in spintronics is that it has been shown skyrmions can be moved with a current density several orders of magnitude smaller than the critical current density needed to move magnetic domain walls [22]. In addition, due to the non-trivial topology of the skyrmion, which acts as a knot in the magnetization, it will require a significant amount of energy to untie this knot and destroy the skyrmion, which makes it a stable information carrier. The information can be encoded by the direction of the magnetization in the skyrmion core, which can be up or down, and therefore acts as a bit. Skyrmions can also be useful for a compact data storage in form of skyrmion crystals [28], as the typical length-scale of skyrmions can be on the nanometer scale, depending on the stabilizing mechanism [72].

The magnetization of the skyrmion can be written in cartesian coordinates as

$$\boldsymbol{M}(r, \phi) = M_s \begin{pmatrix} \cos \Phi(\phi) \sin \theta(r) \\ \sin \Phi(\phi) \sin \theta(r) \\ \cos \theta(r) \end{pmatrix}. \tag{3.2}$$

As the out-of-plane component (here the z-component) of the magnetization in the skyrmion is rotationally symmetric around the skyrmion's core, the out-of-plane angle θ can be written as a function of r only, with r being the distance to the skyrmion's core. The in-plane magnetization angle Φ is assumed to be a linear function of the azimuthal angle ϕ, such that

$$\Phi = m\phi + \psi. \tag{3.3}$$

An illustration of the angle Φ is shown in Figure 3.1. Due to the periodical nature of the
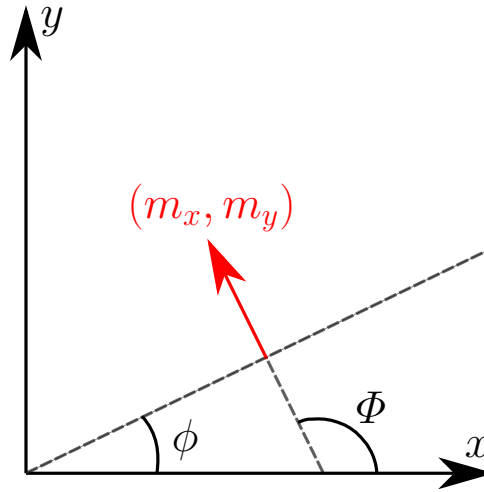
Figure 3.1. The definitions of the angles Φ and ϕ. In this case $\Phi = \phi + \pi/2$, in other words it can be described by $\Phi = m\phi + \psi$ with $m = 1$ and $\psi = \pi/2$.

angles, m is constrained to be an integer. The phase difference ψ between Φ and $m\phi$ is a constant called the helicity of the skyrmion. If one plugs in the ansatz (3.2) into (3.1), one finds that

$$N_{\text{sk}} = \frac{m}{4\pi} \int_0^{2\pi} \mathrm{d}\phi \int_0^\infty \mathrm{d}r \sin \theta(r) \frac{\partial \theta(r)}{\partial r} = -\frac{m}{2} \cos(\theta(r))|_{(r=0)}^{(r=\infty)}. \tag{3.4}$$

Unless m is an even number, one must require that $\theta(r = 0) = 0$ and $\theta(r = \infty) = \pi$, or $\theta(r = 0) = \pi$ and $\theta(r = \infty) = 0$ for the skyrmion number to be an integer and not a half-integer.

The skyrmion needs a certain type of physical mechanism in the material to be a stable state. This mechanism will allow a lower energy state by having the neighbouring spins not be entirely parallel to each other, like the symmetric exchange interaction wants them to be. One of these mechanisms is the Dzyaloshinskii–Moriya interaction, which is the stabilizing mechanism of skyrmions we will consider in this thesis. Other mechanisms that can also cause the magnetic skyrmion to be a stable state are long-ranged magnetic dipolar interactions [73], frustrated exchange interactions [74] and four-spin exchange interactions [69]. If we consider the interfacial DMI energy density in (2.15b) and plug in our ansatz for the magnetization of the skyrmion, one finds that

$$\epsilon_{\mathrm{DM}}^{(\mathrm{interface})} = D\cos((m-1)\phi + \psi)\left(\frac{\partial\theta}{\partial r} + \frac{m}{r}\sin\theta\cos\theta\right). \tag{3.5}$$

For the DMI to have a net energy contribution, we must remove the dependence on ϕ as the average of a harmonic function over the plane will be zero. We therefore require that $m = 1$, which is not an even number, meaning we must apply the boundary conditions for $\theta(r)$ mentioned earlier. The helicity ψ is then chosen to minimize the energy contribution from DMI, which leaves us with the two options $\psi = 0$ and $\psi = \pi$, depending on the sign of D and the θ profile. Due to the boundary conditions for θ, the magnetization in the core of the skyrmion points in the opposite direction of the magnetization far away from the skyrmion core. The magnetization direction far away from the core must therefore be a stable direction in the energy. This can be done in a system with an easy axis parallel to that direction. If we consider a skyrmion in a thin film, which makes sense with our choice of interfacial DMI, the easy axis must be perpendicular to that film. In other words, we need a thin-film system with perpendicular magnetic anisotropy. Finally, as our system is ferromagnetic, we also need to include the symmetric exchange interaction. This is also a mechanism that allows us to treat the skyrmion in the micromagnetic model, where we assume that the magnetization can be estimated by a smooth and slowly varying function. This assumption was for example used in the Taylor expansion of the DMI Hamiltonian. Our model then has the energy density given by

$$\epsilon = \epsilon_{\mathrm{EX}} + \epsilon_{\mathrm{PMA}} + \epsilon_{\mathrm{DM}}^{(\mathrm{interface})}$$
$$= A\left[\left(\frac{\partial\theta}{\partial r}\right)^2 + \frac{\sin^2\theta}{r^2}\right] + K\sin^2\theta + D\cos\psi\left(\frac{\partial\theta}{\partial r} + \frac{\sin\theta\cos\theta}{r}\right), \tag{3.6}$$

assuming a magnetization profile given by (3.2). The energy is independent of ϕ due to our choice of m, but it remains a function of θ and r. As the skyrmion is a ground state, we can find the function $\theta(r)$ by minimizing the energy. Using the condition

$$\frac{\delta\epsilon(\theta, r)}{\delta\theta(r)} = \frac{\partial\epsilon}{\partial\theta} - \frac{\mathrm{d}}{\mathrm{d}r}\frac{\partial\epsilon}{\partial(\frac{\partial\theta}{\partial r})} = 0 \tag{3.7}$$

and introducing the dimensionless length $\tilde{r} = rD/A$, one ends up with the following differential equation for $\theta(r)$:

$$\frac{\partial^2\theta}{\partial\tilde{r}^2} + \frac{1}{\tilde{r}}\frac{\partial\theta}{\partial\tilde{r}} - \frac{\sin\theta\cos\theta}{\tilde{r}^2} + \cos\psi\frac{\sin^2\theta}{\tilde{r}} - \frac{AK}{D^2}\sin\theta\cos\theta = 0. \tag{3.8}$$

Defining the ratio AK/D^2 as a parameter C, one can solve this equation numerically for a given C. Some numerical solutions are shown in Figure 3.2 when the boundary conditions $\theta(r = 0) = \pi$ and $\theta(r = \infty)$ have been used. It should be noted that this differential

equation only has a solution when $\cos \psi = 1$ for the chosen boundary conditions. The solutions for the different helicities $\psi_1 = 0$ and $\psi_2 = \pi$ have a simple relation, however. This relation can be verified to be

$$\theta_{\psi_1}(r) = \pi - \theta_{\psi_2}(r), \tag{3.9}$$

as $\cos \psi$ is antisymmetric under a swap in helicities, and $\frac{\partial^2 \theta}{\partial \tilde{r}^2}$, $\frac{\partial \theta}{\partial \tilde{r}}$, $\cos \theta_{\psi_i}$ are all antisymmetric under the relation above. The two different skyrmions for the two different choices
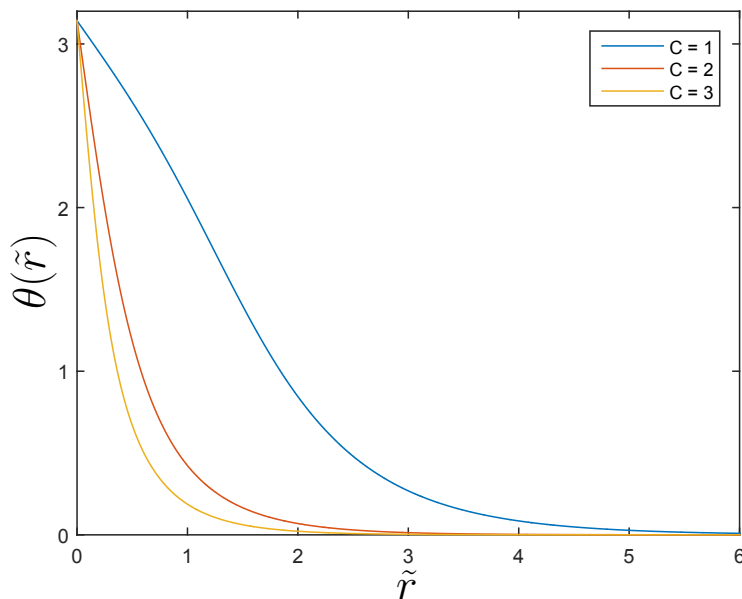
Figure 3.2. The solution of the out-of-plane angle θ of the skyrmion profile for different values of C.

in helicities ψ are illustrated in Figure 3.3. This type of skyrmions is called a hedgehog skyrmion, due to the magnetization pattern that curves into or away from the core.

The results shown so far are based on a system that is stabilized by the interfacial form of DMI. Skyrmions can also be stabilized by the bulk form of DMI, however. Using the ansatz of the skyrmion magnetization profile in (3.2) in the expression for bulk DMI given by (2.12), we find the same energy density as for the interfacial DMI $\epsilon_{\text{DM}}^{(\text{interface})}$ with the substitution $\cos \psi \to \sin \psi$. In other words, the skyrmion stabilized by the bulk DMI will have helicities $\psi = \pm \pi/2$, and the $\theta(r)$ profile will be the same as for the hedgehog skyrmions stabilized by the interfacial DMI. These types of skyrmions are called spiral skyrmions, as the in-plane magnetization either spirals clockwise or counter-clockwise around the core. From now on we will mostly consider hedgehog skyrmions stabilized by the interfacial form of DMI, as that is the form of DMI that is found in layered thin-film systems that we will study.

3.2   Symmetries

Before moving on to the dynamical properties of the skyrmions we will take a brief interlude to discuss the symmetries of the skyrmion and the LLG equation. This will help
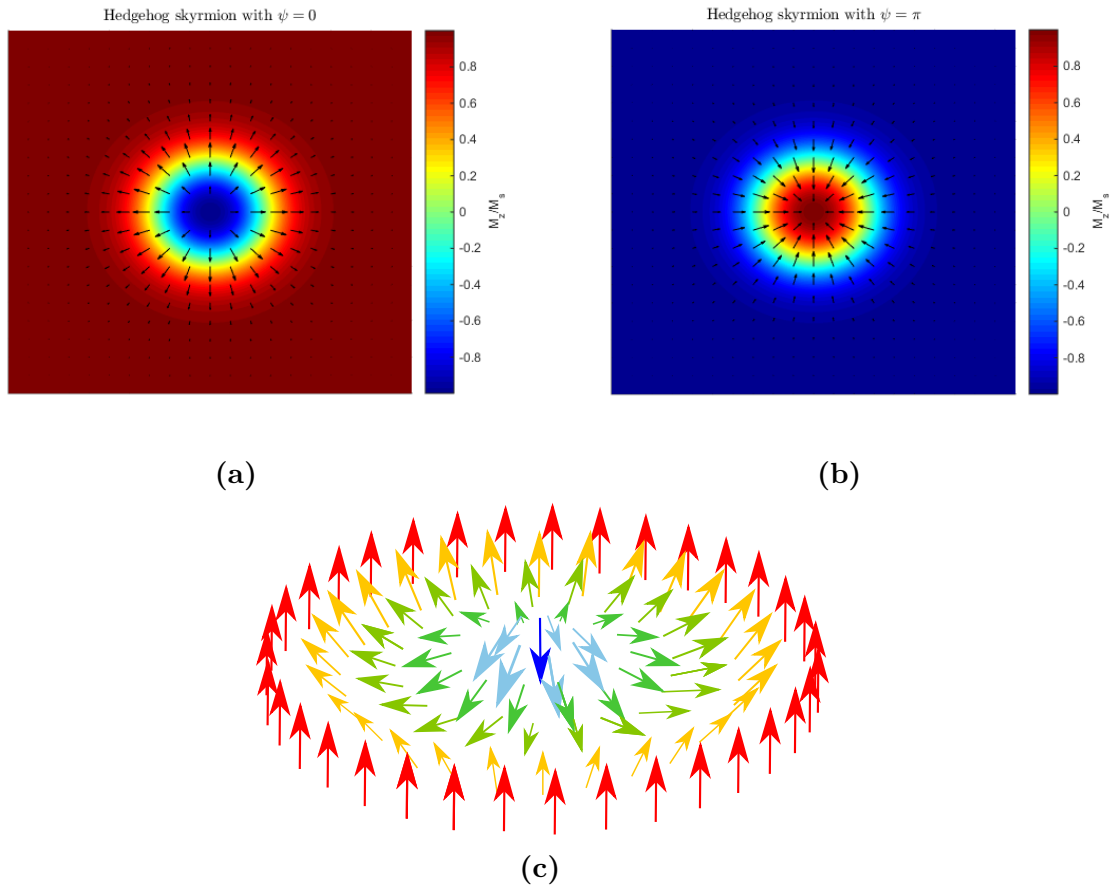
Figure 3.3. A hedgehog skyrmion with a helicity **(a)** $\psi = 0$ and **(b)** $\psi = \pi$. The in-plane component of the magnetization is visualized by the vectors, while the z-component is shown in the background color. A 3D representation of a hedgehog skyrmion with $\psi = 0$ is shown in **(c)**, this figure is based on a figure in [75].

us to get further insight into how the different terms in the LLG equation work, and how the skyrmion solutions are related to each other.

3.2.1 Time reversal

Time reversal (or T-symmetry) is a transformation where one reverses the time ($t \rightarrow -t$) as the name indicates. Physical laws that are symmetric under time reversal are reversible processes, while physical laws that break the time reversal symmetry are irreversible processes. Physical variables are either even or odd during time reversal. If they are even they are symmetric under time reversal, and if they are odd they are asymmetric during time reversal. To discuss whether the LLG equation breaks time reversal we need to know how the magnetization $\boldsymbol{M}$ and the magnetic field $\boldsymbol{H}$ transform (the constants α, M_s and γ are all even under time reversal, as they are scalars unrelated to the weak force). It turns out that both $\boldsymbol{M}$ and $\boldsymbol{H}$ are odd during time reversal [76]. If we then apply the time reversal transformation to the LLG equation, we end up with

$$\frac{\mathrm{d}\boldsymbol{M}}{\mathrm{d}t} = -\gamma \boldsymbol{M} \times \boldsymbol{H} - \frac{\alpha}{M_s} \boldsymbol{M} \times \frac{\mathrm{d}\boldsymbol{M}}{\mathrm{d}t}. \tag{3.10}$$

Comparing this to the LLG equation in (2.22) we see that the LLG equation breaks T-symmetry due to the damping term proportional to α. The damping is a dissipative

motion, and is therefore an irreversible process. The precession of the magnetization around the magnetic field on the other hand does not break T-symmetry, and is therefore a reversible process.

3.2.2 Parity and chirality

Parity is a transformation operation which changes the sign of all three cartesian coordinates simultaneously ($\boldsymbol{r} \rightarrow -\boldsymbol{r}$), in other words it is a point reflection through the origin. To dicuss parity we first introduce the notion of pseudovectors and pseudoscalars. Normally, vectors are odd under a parity transformation, meaning the transformation changes the sign of the vector, while scalars are even under a parity transformation. Pseudovectors and pseudoscalars behave the opposite way, however. A pseudovector will behave as a vector during a rotation, but during a reflection it behaves differently. An example of a pseudovector is the antisymmetric cross-product between two vectors, which is illustrated in Figure 3.4. A pseudoscalar is the symmetric dot-product between a pseudovector and a
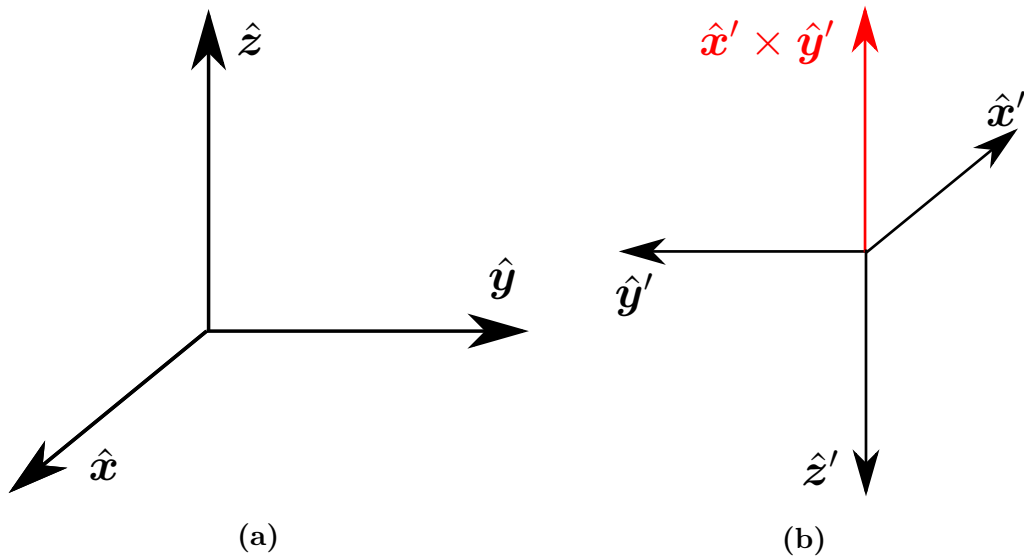
Figure 3.4. An illustration of how cross-products do not transform as vectors under parity. In **(a)** we see a cartesian coordinate system. Performing a parity transformation on this right-handed coordinate system gives us the left-handed coordinate system in **(b)**. The pseudovector $\hat{\boldsymbol{x}} \times \hat{\boldsymbol{y}}$, which in our right-handed system is equal to $\hat{\boldsymbol{z}}$, is even under the parity transformation, while the vector $\hat{\boldsymbol{z}}$ is odd.

vector. When studying the parity of an expression, the folowing relations may be useful:

$$\text{vector} \times \text{vector} = \text{pseudovector}, \tag{3.11a}$$

$$\text{vector} \times \text{pseudovector} = \text{vector}, \tag{3.11b}$$

$$\text{pseudovector} \times \text{pseudovector} = \text{pseudovector}, \tag{3.11c}$$

$$\text{vector} \cdot \text{vector} = \text{scalar}, \tag{3.11d}$$

$$\text{vector} \cdot \text{pseudovector} = \text{pseudoscalar}, \tag{3.11e}$$

$$\text{pseudovector} \cdot \text{pseudovector} = \text{scalar}. \tag{3.11f}$$

Now we must consider how the vectors in our equations transform under a parity operation. The relevant vectors are $\boldsymbol{M}$, $\boldsymbol{H}$, $\boldsymbol{E}$, ∇, $\hat{\boldsymbol{x}}$, $\hat{\boldsymbol{y}}$ and $\hat{\boldsymbol{z}}$. The magnetization and magnetic field are both pseudovectors, and are even under a parity transformation [76].

The unit vectors in cartesian coordinates are ordinary vectors, and therefore odd under a parity transformation. As a consequence, the components of the magnetization M_x, M_y and M_z are all pseudoscalars, which can be seen from (3.11e). The electric field is also odd under a parity transformation [76], which means that the electric field components behave as scalars, as seen from (3.11d). Lastly the ∇ operator also transforms as a vector, and is therefore odd under parity.

We now have all the results we need to consider the parity of the LLG equation, the effective field, the micromagnetic energy and the skyrmion magnetization. Starting off with the LLG equation (2.22), we see that it does not break parity explicitly as long as $\boldsymbol{H}$ is even under a parity transformation by using the relation in (3.11c). When considering the micromagnetic energy terms, all are found to be even under a parity transformation with the exception of the DMI terms (which holds true for both the bulk form of DMI in (2.12) and the interfacial form in (2.15b)). At first glance, however, it may seem like the interfacial form of the DMI energy density in (2.15b) is even under parity. The reason for this is that while going from the original expression in (2.11) (which is seen to break parity from (3.11c) as $\boldsymbol{D}_{ij}$ is a vector and $\boldsymbol{S} \propto \boldsymbol{M}$ is a pseudovector) we have eliminated a cross product. As one can see in (2.15a) we have terms that go as $\hat{\boldsymbol{x}} \cdot (\hat{\boldsymbol{y}} \times \hat{\boldsymbol{z}})$ and $\hat{\boldsymbol{y}} \cdot (\hat{\boldsymbol{z}} \times \hat{\boldsymbol{x}})$. In (2.15b) these vector expressions are simplified to be unity, which is correct, but hides some of the information when we want to study parity. As $\hat{\boldsymbol{y}} \times \hat{\boldsymbol{z}}$ and $\hat{\boldsymbol{z}} \times \hat{\boldsymbol{x}}$ are pseudovectors, $\hat{\boldsymbol{x}} \cdot (\hat{\boldsymbol{y}} \times \hat{\boldsymbol{z}})$ and $\hat{\boldsymbol{y}} \cdot (\hat{\boldsymbol{z}} \times \hat{\boldsymbol{x}})$ are in fact pseudoscalars which we can see from (3.11e). So in reality there is a unity pseudoscalar lurking in the expression in (2.15b), making it seem like it is even under parity while in reality it is not. This same pseudoscalar is carried onwards to the DMI term in the effective field in (2.23), making part of the effective field odd under parity and thereby violating parity in the LLG equation.

Moving on to the skyrmion magnetization pattern we use that $\boldsymbol{M}$ is even under parity, while its components M_x, M_y and M_z are not. Remembering that $\hat{\boldsymbol{M}} = (\cos\Phi\sin\theta, \sin\Phi\sin\theta, \cos\theta)$ we see that all the components are odd under parity if Φ transforms as $\Phi \to \Phi \pm \pi$ and θ transforms as $\theta \to \pi - \theta$. This is reminiscent of something we have seen earlier. In Section 3.1 we noted that the solutions for the two different helicities were related by (3.9), which is the same as the way θ transforms under parity. In addition, the two possible helicities for the individual types of skyrmions (hedgehog or spiral) are always a phase $\pm\pi$ apart. The term $\pm\pi$ in the transformation of Φ under parity can then be included in the helicity, meaning the parity transformation changes the helicity of the skyrmion. The two possible solutions of the skyrmions, such as the hedgehog skyrmions in Figure 3.3a and 3.3b, are therefore related to each other via parity. If the skyrmion in 3.3a is the solution in a right-handed coordinate system, the skyrmion in 3.3b is the same solution in a left-handed coordinate system, and vice versa.

As a final comment on the symmetries of the skyrmions, we want to discuss their chirality. An object is defined to be chiral if its mirror image or reflection is impossible to align with the original object. The most common example of chirality is hands. When holding your right hand in front of a mirror, the image you see in the mirror is that of a left hand. Obviously, a right hand and a left hand are distinct, and can therefore not be aligned with each other. Hands are then chiral objects. When we are considering a mirror image of a skyrmion, we need to be careful regarding what we take the mirror image of. The mirror image of a skyrmion is *not* the mirror image of the skyrmion magnetization vector field. The magnetization of the skyrmion stems from the average magnetic moment inside a small volume, and the magnetic moment is proportional to the spinning of the electron. As we see in Figure 3.5, when we mirror the spinning motion of the electron
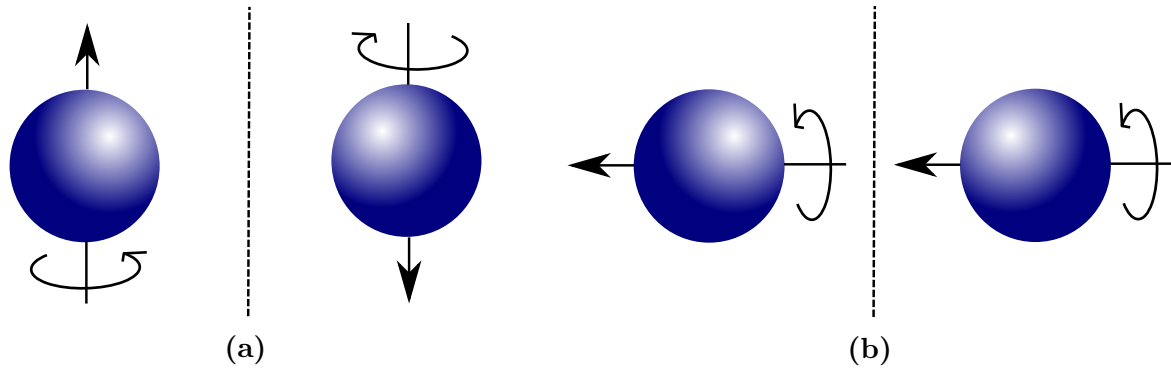
Figure 3.5. An electron that has a spin vector parallel to a mirror plane will have its spin reversed in its mirror image, as shown in **(a)**. An electron with a spin perpendicular to the mirror plane, however, will have the same spin as its mirror image as shown in **(b)**.
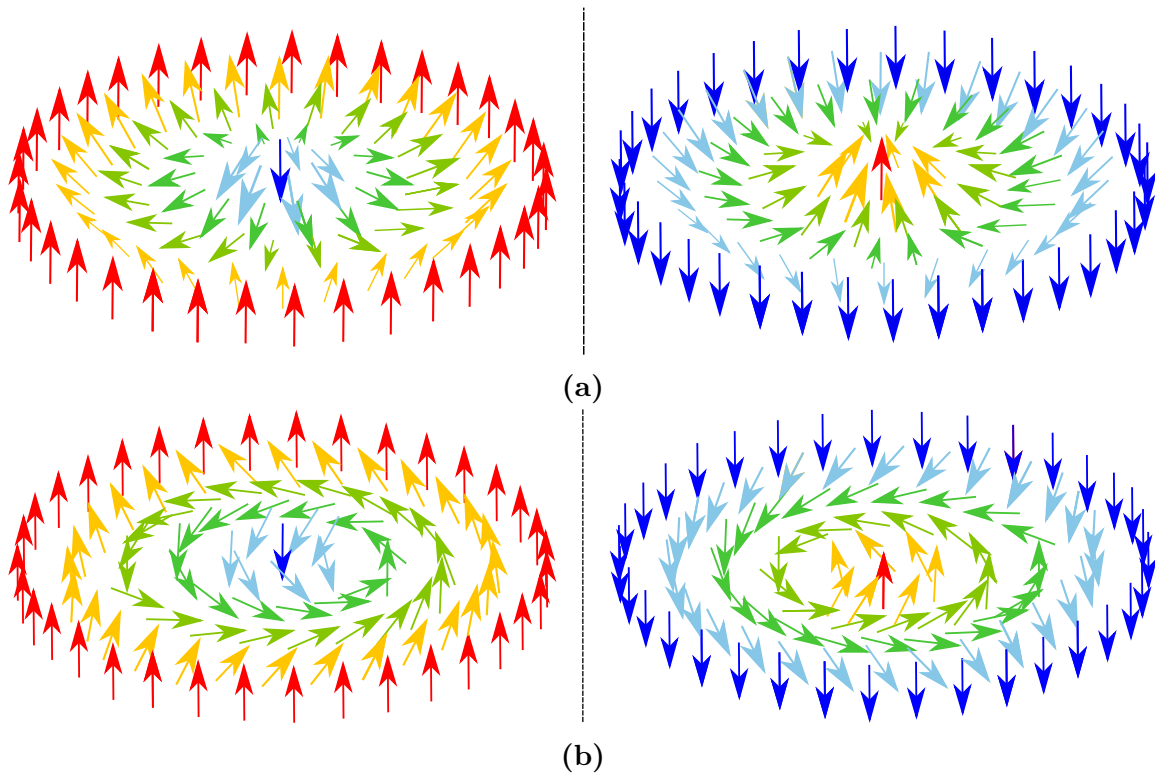
Figure 3.6. The mirror images of **(a)** a hedgehog skyrmion, and **(b)** a spiral skyrmion. The mirror images can not be aligned with the original image, and the skyrmions are therefore chiral objects. The skyrmion figures are based on the figures in [75].

the spin vector is not its mirror image. The component of the spin vector parallel to the mirror plane is flipped, while the perpendicular component is the same for both the original electron and its mirror image. In both cases this is the opposite behavior of the mirror image of a regular vector, and this behavior is general for pseudovectors (also known as axial vectors). We also note that this reflection is only in one coordinate, whereas parity in three dimensions is a reflection in all coordinates. The spin is therefore still invariant under parity, even if it is not under a reflection parallel to the spin. A parity transformation would correspond to two reflections parallel to the vector (as in Figure 3.5a) and one reflection perpendicular to the vector (as in Figure 3.5b). The sum of these reflections would then be an identity transformation, as we have an even number

of parallel reflections that invert the direction of the spin. For a regular vector the sum would be an inversion, as it is the perpendicular reflection (as in Figure 3.5b, but now with the mirror image of the spin vector itself and not the rotation of the electron) that inverts the vector, and the number of perpendicular reflections is odd.

The magnetization is a pseudovector, and the mirror images of the skyrmion profiles will therefore behave in the same manner as in Figure 3.5. The resulting mirror images of the skyrmion magnetization are then as shown in Figure 3.6. No matter how one rotates the mirror images of the skyrmion magnetization, one can not align them with the original skyrmion. The skyrmions are therefore chiral. This is a consequence of the broken parity of the skyrmion magnetization profile due to the Dzyaloshinskii–Moriya interaction. If the parity transformation of an object is not an identity transformation, it is a chiral object.

3.3   The Thiele equation

In the special case of a time-dependent magnetization pattern that can be written as $\boldsymbol{M}(\boldsymbol{r} - \boldsymbol{R}(t))$, Thiele recognized [77] that the time derivative can be written as

$$\frac{\mathrm{d}\boldsymbol{M}}{\mathrm{d}t} = \frac{\partial \boldsymbol{R}}{\partial t}\frac{\partial \boldsymbol{M}}{\partial \boldsymbol{R}} = \frac{\partial \boldsymbol{R}}{\partial t}\left(-\frac{\partial \boldsymbol{M}}{\partial \boldsymbol{r}}\right) = -(\boldsymbol{v} \cdot \nabla)\boldsymbol{M}. \tag{3.12}$$

The form $\boldsymbol{M}(\boldsymbol{r} - \boldsymbol{R}(t))$ indicates that the magnetization pattern performs a translation without deformation of the original magnetization profile. Once the equilibrium profile at some time t_0 is known, the motion of the entire magnetization pattern can be described by the time-dependent position of some distinct part of the magnetization pattern, like the skyrmion core. If one replaces all time derivatives with Thiele's relation as given above in the LLG equation, one can rewrite the LLG equation to the Thiele equation (as shown by Krüger in [78]):

$$\boldsymbol{F} + \boldsymbol{G} \times (\boldsymbol{v} + b_J\hat{\boldsymbol{j}}_e) - D(\alpha\boldsymbol{v} + \beta b_J\hat{\boldsymbol{j}}_e) = 0. \tag{3.13}$$

This is a force equation with the definitions

$$\boldsymbol{F} = -\frac{\partial E}{\partial \boldsymbol{R}} = -\mu_0 \int \mathrm{d}V \sum_k (\nabla M_k)(H_k), \tag{3.14a}$$

$$\boldsymbol{G} = \frac{2\pi M_s \mu_0 d}{\gamma'} \left[\cos\theta\right]_{\theta(r=0)}^{\theta(r=\infty)} \hat{\boldsymbol{z}}, \tag{3.14b}$$

$$D = \frac{\pi M_s \mu_0 d}{\gamma'} \int_0^\infty \mathrm{d}r \left(r\left(\frac{\partial \theta}{\partial r}\right)^2 + \frac{\sin^2\theta}{r} \right), \tag{3.14c}$$

where d is the thickness of the film. The vector $\boldsymbol{F}$ is a force originating from an inhomogenous energy landscape or a magnetic field that is not parallel to the local magnetization (in other words a field not aligned with the magnetization). $\boldsymbol{G}$ is a gyrovector that only depends on the direction of the magnetization in the skyrmion core and far away from the core. The force in the Thiele equation that is dependent on $\boldsymbol{G}$ is often called the Magnus force, and is a counter force to the Lorentz forces from emergent electromagnetic fields around the skyrmion [79], which we will discuss in the next section. Lastly, D denotes the strength of a dissipative force that moves the skyrmion in the direction of the electron flow and it is dependent on the radial profile of the out-of-plane angle θ of the skyrmion.

An illustration of the force balance in the Thiele equation is shown in Figure 3.7. The Thiele equation is less rigid than the LLG equation due to the ansatz that there is an absence of deformation of the skyrmion, but in the case of a purely translational motion of the skyrmion the Thiele and LLG equations are entirely equivalent.
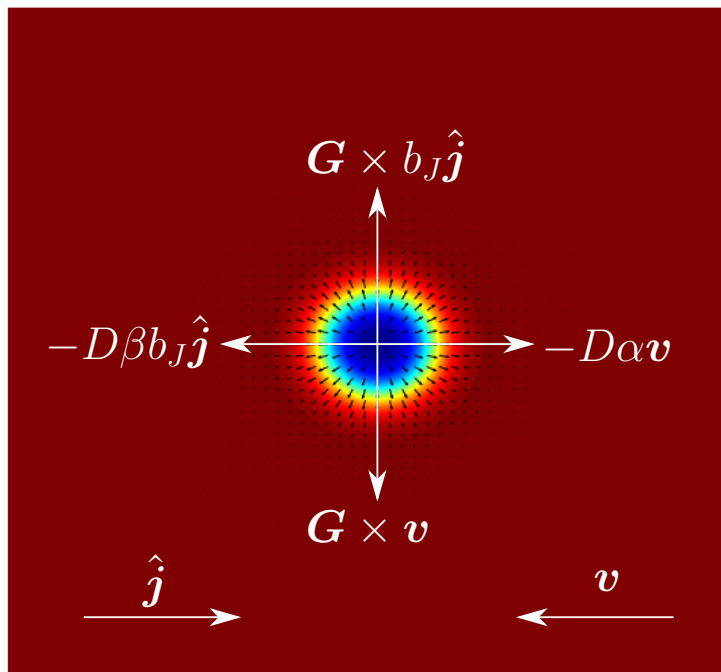

Figure 3.7. An example of the forces in the Thiele equation. In the example shown $\alpha = \beta$ and $\boldsymbol{v} = -b_J\hat{\boldsymbol{j}}$. The force vectors are only there to show direction, and not magnitude. The goal of the Thiele equation is finding a velocity $\boldsymbol{v}$ that makes all the forces add up to zero.

3.4   Berry phase, emergent fields, and the topological Hall effect

When discussing the dynamics of skyrmions, it will be useful to have some knowledge of Berry phases. The Berry phase [80], also known as a geometric phase, is a rotational angle gained by a vector when it undergoes parallel transport on a closed path on a curved surface, as illustrated in Figure 3.8. If the closed path was in a plane, however, the vector will not gain a rotation along its cycle. Skyrmions are magnetization patterns that can be located in a plane, so why is then the Berry phase of interest when electrons move in that plane? When we first started discussing skyrmions, we said that the skyrmion wraps around the unit sphere. In other words, while the magnetization of the skyrmion is located in a plane, the topology of the magnetization pattern behaves in a way so that it can be described as lying on a spherical surface [79]. This is illustrated in Figure 3.9. So despite the fact that the conduction electrons from an applied current are moving in a two-dimensional plane, their magnetic moment will still gain a Berry phase when following the magnetization of the skyrmion adiabatically, as the magnetization of the skyrmion points in all three spatial directions [81, 82]. When moving through the skyrmion magnetization, the conduction electrons path is then bent away from the initial direction of the current. This can be seen as a force acting on the conduction electrons, and then there must
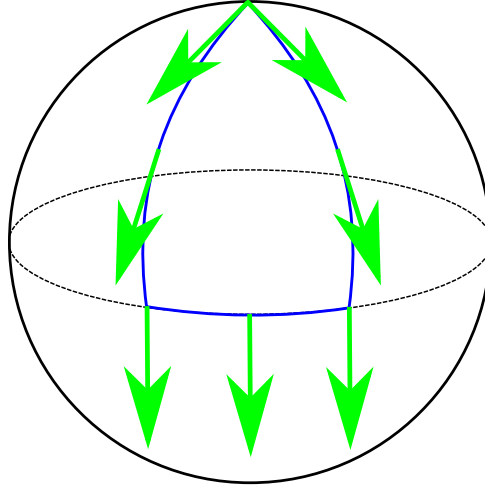
Figure 3.8. When a vector undergoes a parallel transport along a closed path on a sphere, it will not be in the same state when arriving back at its starting point. It is rotated in respect to the initial vector, and this rotational angle is known as the Berry phase.

(a)   **(b)**
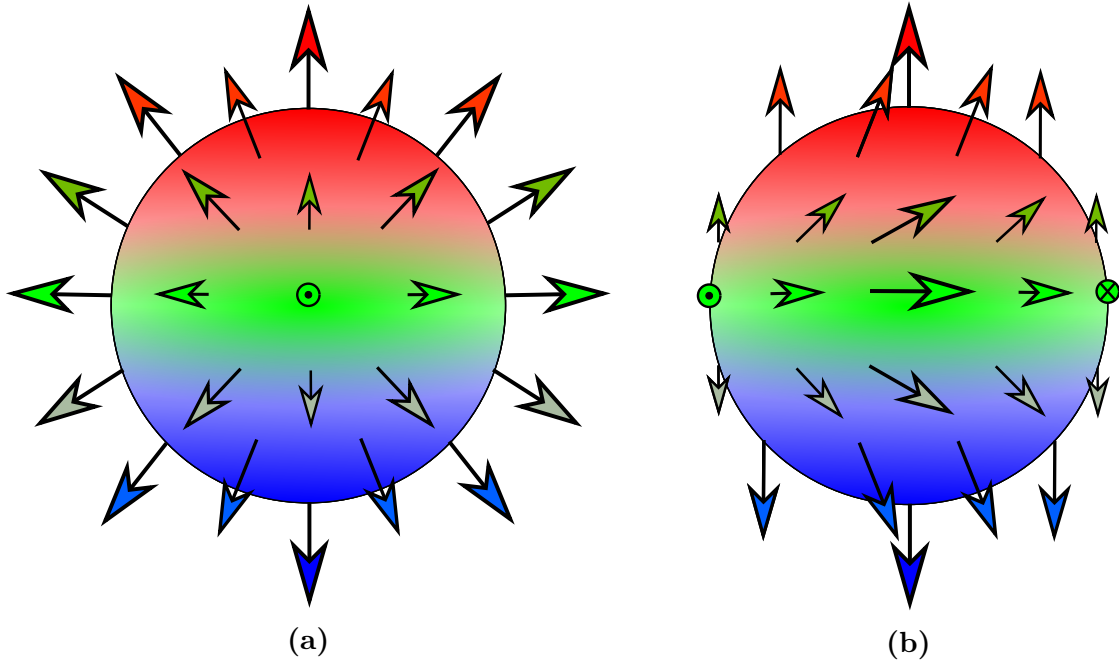
Figure 3.9. Skyrmions magnetization patterns mapped onto a spherical surface. The magnetization at $r = 0$ is at the bottom of the sphere, while the magnetization at $r = \infty$ is at the top. In **(a)** we see a hedgehog skyrmion with $\psi = 0$, while in **(b)** we see a spiral skyrmion with $\psi = \pi/2$.

be an equal force acting in the opposite direction on the skyrmion magnetization. This movement perpendicular to the current direction is known as the topological Hall effect [83], as it depends entirely on the topology of the magnetization.

In magnetization dynamics the Berry phase is most commonly considered through the use of emergent electromagnetic fields. The Berry phase can be found by integrating a quantity known as the Berry vector potential along the closed path in consideration. This vector potential is similar to the vector potential $\boldsymbol{A}$ in electromagnetism, and the curl of this vector potential (known as the Berry curvature) will then behave as a magnetic field [84]. This emergent magnetic field, which is associated with the topology of the

magnetization and not its magnetic flux, is given by [85, 23]

$$\boldsymbol{B}_i^e = \frac{\hbar}{2e}\varepsilon_{ijk}\hat{\boldsymbol{M}} \cdot (\partial_j \hat{\boldsymbol{M}} \times \partial_k \hat{\boldsymbol{M}}). \tag{3.15}$$

This total magnetic flux from this emergent field is quantized by the skyrmion number N_{sk} given by (3.1), which can be seen by integrating the expression above over the skyrmion plane. This emergent magnetic field then causes the conduction electrons to experience a Lorentz force

$$\boldsymbol{F}_{\text{Lorentz}} = q(\boldsymbol{E} + \boldsymbol{v} \times \boldsymbol{B}). \tag{3.16}$$

If one assumes the skyrmion magnetization to be localized in the xy-plane and to be isotropic in the z-direction, then the emergent field $\boldsymbol{B}_i^e$ points along the z-axis. This means that the Lorentz force originating from the emergent magnetic field is localized in the xy-plane, and is perpendicular to the motion of the conduction electrons. This bending of the electrons' motion can induce a motion of the skyrmion perpendicular to the direction of the current. In addition to the emergent magnetic field, there will also be an emergent electric field once the skyrmion magnetization starts moving, for example due to spin-transfer torques where the magnetic moment of the conduction electrons is transferred to the local magnetization. As seen from the Maxwell–Faraday equation,

$$\nabla \times \boldsymbol{E} = -\partial_t \boldsymbol{B}, \tag{3.17}$$

once the magnetization pattern starts moving the emergent magnetic field will become time dependent, and thereby induce an emergent electric field. This emergent field is given by

$$\boldsymbol{E}_i^e = \frac{\hbar}{e}\hat{\boldsymbol{M}} \cdot (\partial_i \hat{\boldsymbol{M}} \times \partial_t \hat{\boldsymbol{M}}). \tag{3.18}$$

This electric field will also cause the electrons to feel a Lorentz force, and as we can see from the expression above this force is perpendicular to the motion of the skyrmion. Through these emergent fields we can then get an intuitive explanation of the topological Hall effect.

We have now discussed qualitatively the dynamics of the skyrmion, and why its dynamics distinguishes itself from topologically trivial magnetization patterns. Building upon this discussion, we will in the next chapter start studying the dynamics of the skyrmion more quantitatively by both analytical and numerical calculations.

4

Electric control of skyrmion motion

Since it was shown theoretically by Berger [9, 10, 11, 12] and Slonczewski [13] that a spin-polarized current could exert a torque on the magnetization in magnetic materials, there has been a lot of focus on electrical control of magnetization dynamics. Through the spin-transfer torque mechanism one was able to switch the magnetization direction in a magnetic layer solely by applying a current through the material [15, 16, 17]. This magnetization switching could for example be achieved by a current induced motion of magnetic domain walls [86, 87, 88, 89].

It has been shown that skyrmions can also be moved by applying a current, and they can be moved by a much weaker current than magnetic domain walls [22, 24], which is the reason for the new interest in them. The velocity at which they can be moved is much smaller than what is achievable by magnetic domain walls, however [28, 32]. Recently it has also been shown that the motion of skyrmions can also be guided through the means of electric fields [27]. It has also been discovered that through the help of constricted geometries and electrical currents, we can create skyrmions in chiral magnets [90, 29, 91]. In addition we are able to detect skyrmions with an unpolarized current [92]. Very recently the ability to generate and control the motion of skyrmions in racetracks has been demonstrated [93]. These new developments will greatly help us in utilizing magnetic skyrmions in memory applications.

The goal of this chapter is to study the equations of motion for the skyrmion, both analytically and numerically, so that we can see how we can steer the motion of the skyrmion in the direction we want. We will consider the motion due to an inhomogeneous electric field and an electric current, which will cause the magnetization to experience Rashba fields due to the broken inversion symmetry. An understanding of how we can control the motion of skyrmions by electrical means will be very useful in regards to how we can utilize skyrmions in memory applications.

4.1   Skyrmion velocity

The extended LLG equation that includes Rashba spin–orbit coupling and spin-transfer torques is given by

$$\partial_t \boldsymbol{M} = -\gamma' \boldsymbol{M} \times \left(\boldsymbol{H}_{\text{eff}} + \boldsymbol{H}_{\text{R}} - \frac{\beta}{M_s} \boldsymbol{M} \times \boldsymbol{H}_{\text{R}} \right)$$
$$+ \frac{\alpha}{M_s} \boldsymbol{M} \times \partial_t \boldsymbol{M} + b_J (\hat{\boldsymbol{j}}_e \cdot \nabla) \boldsymbol{M} - \frac{\beta b_J}{M_s} \boldsymbol{M} \times (\hat{\boldsymbol{j}}_e \cdot \nabla) \boldsymbol{M}, \qquad (4.1)$$

with the Rashba field $\boldsymbol{H}_{\text{R}}$ being given by

$$\boldsymbol{H}_{\text{R}} = \frac{\alpha_{\text{R}} m_e}{\hbar \mu_0 \mu_B} b_J (\hat{\boldsymbol{z}} \times \hat{\boldsymbol{j}}_e) = C_{\text{R}} b_J (\hat{\boldsymbol{z}} \times \hat{\boldsymbol{j}}_e) \qquad (4.2)$$

and b_J being a characteristic velocity

$$b_J = \frac{1}{1 + \beta^2} \frac{\mu_B P j}{e M_s}. \qquad (4.3)$$

The modified gyromagnetic ratio γ' is slightly perturbed with respect to γ, but this perturbation is so small that for all essential purposes we will assume $\gamma' \approx \gamma$. This result was derived by Kim *et al.* in [94] in a manner similar to the approach in Section 2.3.2, where the Rashba Hamiltonian (2.10) was included in the derivation with the *s-d* Hamiltonian. We now want to find this equation in the Thiele formalism, as it then goes from being a partial differential equation to being an algebraic equation in the velocity components. The terms involving the Rashba field $\boldsymbol{H}_{\text{R}}$ act as a magnetic field in the LLG equation, and we can therefore use the definition of the force from a magnetic field that is not aligned with the magnetization in the Thiele equation as given by (3.14a):

$$\boldsymbol{F}_{\text{R}} = -\mu_0 \int \mathrm{d}V \sum_k (\nabla M_k) \left[\boldsymbol{H}_{\text{R}} - \frac{\beta}{M_s} \boldsymbol{M} \times \boldsymbol{H}_{\text{R}} \right]_k. \qquad (4.4)$$

This expression is calculated in Appendix A and is found to be

$$\boldsymbol{F}_{\text{R}} = -\mu_0 \pi \beta C_{\text{R}} b_J M_s d \int_0^\infty \mathrm{d}r \left(\frac{\partial \theta}{\partial r} r + \sin \theta \cos \theta \right) \hat{\boldsymbol{x}} \qquad (4.5)$$

for a hedgehog skyrmion with $\psi = 0$ and $\theta(r = 0) = \pi, \theta(r = \infty) = 0$. We have assumed that the direction of the current is $\hat{\boldsymbol{j}}_e = \hat{\boldsymbol{x}}$. We will only consider these choices for the remainder of this chapter. This is reasonable, as for our particular choice of geometry with thin films (which is necessary to get a significant contribution from the electric field control) hedgehog skyrmions have the lowest energy due to interfacial DMI. We are also free to define the direction along the current to be the x-direction.

We now have the force resulting from Rashba spin–orbit coupling, the next step is then to find the force from an inhomogenous electric field. If we consider an electric field with a constant gradient, the field can then be written in cartesian and skyrmion coordinates as

$$E(\boldsymbol{r}) = E_x x + E_y y \qquad (4.6a)$$
$$= E_x x_0 + E_y y_0 + E_x r \cos \phi + E_y r \sin \phi, \qquad (4.6b)$$

with (x_0, y_0) indicating the location of the skyrmion core. If we integrate this energy density over the entire film, we then find that the total energy contribution from the electric field becomes

$$
\begin{aligned}
U_{\text{EF}} &= \int \mathrm{d}V \, \epsilon_{\text{EF}} \\
&= \eta \int_0^d \mathrm{d}z \int_0^{2\pi} \mathrm{d}\phi \int_0^\infty \mathrm{d}r \, (E_x x_0 + E_y y_0 + E_x r \cos\phi + E_y r \sin\phi) \, r \sin^2\theta \\
&= 2\pi\eta d \, (E_x x_0 + E_y y_0) \int_0^\infty \mathrm{d}r r \sin^2\theta.
\end{aligned}
\tag{4.7}
$$

Remembering that a gradient of the free micromagnetic energy will result in a force in the Thiele equation, as described by (3.14a), we can write the force resulting from the inhomogenous electric field as

$$
\begin{aligned}
\boldsymbol{F}_{\text{E}} &= -\nabla U_{\text{EF}} \\
&= -2\pi\eta d \, (E_x \hat{\boldsymbol{x}} + E_y \hat{\boldsymbol{y}}) \int_0^\infty \mathrm{d}r r \sin^2\theta.
\end{aligned}
\tag{4.8}
$$

We note that the ∇ operator does not act on the integral, as this is independent of the position of the skyrmion core and is therefore just a constant. The final equation in the Thiele formalism for our model can then be written as

$$
\boldsymbol{F}_{\text{R}} + \boldsymbol{F}_{\text{E}} + \boldsymbol{G} \times \left(\boldsymbol{v} + b_J \hat{\boldsymbol{j}}_e\right) - D\left(\alpha\boldsymbol{v} + \beta b_J \hat{\boldsymbol{j}}_e\right) = 0,
\tag{4.9}
$$

where we remember the definitions of the gyrovector $\boldsymbol{G}$ and dissipation factor D to be

$$
\boldsymbol{G} = \frac{2\pi M_s \mu_0 d}{\gamma'} \left[\cos\theta\right]_{\theta(r=0)}^{\theta(r=\infty)} \hat{\boldsymbol{z}}
\tag{4.10a}
$$

$$
D = \frac{\pi M_s \mu_0 d}{\gamma'} \int_0^\infty \mathrm{d}r \left(r \left(\frac{\partial\theta}{\partial r}\right)^2 + \frac{\sin^2\theta}{r}\right).
\tag{4.10b}
$$

If we divide this equation by the length of $\boldsymbol{G}$, the non-trivial equations we end up with are

$$
-Rb_J - C_E E_x - \dot{y}_0 - \alpha_C \dot{x}_0 - \beta_C b_J = 0,
\tag{4.11a}
$$

$$
-C_E E_y + \dot{x}_0 + b_J - \alpha_C \dot{y}_0 = 0,
\tag{4.11b}
$$

where we have made the following definitions:

$$
\alpha_C = \frac{\alpha}{4} \int_0^\infty \mathrm{d}r \left(r \left(\frac{\partial\theta}{\partial r}\right)^2 + \frac{\sin^2\theta}{r}\right),
\tag{4.12a}
$$

$$
\beta_C = \frac{\beta}{4} \int_0^\infty \mathrm{d}r \left(r \left(\frac{\partial\theta}{\partial r}\right)^2 + \frac{\sin^2\theta}{r}\right),
\tag{4.12b}
$$

$$
R = \frac{\gamma' \beta C_{\text{R}}}{4} \int_0^\infty \mathrm{d}r \left(\frac{\partial\theta}{\partial r} r + \sin\theta \cos\theta\right),
\tag{4.12c}
$$

$$
C_E = \frac{\gamma' \eta}{2\mu_0 M_s} \int_0^\infty \mathrm{d}r r \sin^2\theta.
\tag{4.12d}
$$

Solving the equations in (4.11) for $\dot{x}_0$ and $\dot{y}_0$ one finally ends up with the velocity components of the motion of a skyrmion under the influence of spin-transfer torque, Rashba spin–orbit coupling and an inhomogenous electric field:

$$\dot{x}_0 = -\frac{1 + \alpha_C(\beta_C + R)}{\alpha_C^2 + 1}b_J + \frac{C_E}{\alpha_C^2 + 1}E_y - \frac{\alpha_C C_E}{\alpha_C^2 + 1}E_x, \tag{4.13a}$$

$$\dot{y}_0 = \frac{\alpha_C - (\beta_C + R)}{\alpha_C^2 + 1}b_J - \frac{C_E}{\alpha_C^2 + 1}E_x - \frac{\alpha_C C_E}{\alpha_C^2 + 1}E_y. \tag{4.13b}$$

From this result we can see the effects of RSOC and an electric field gradient on the velocity of the skyrmion center of mass. The RSOC has the same impact on the motion as the non-adiabatic STT, and appears as a correction to β_C in the equations of motion. Note that only the term proportional to $\beta \boldsymbol{M} \times \boldsymbol{H}_{\mathrm{R}}$ has an impact on the skyrmion dynamics, as a constant magnetic field like $\boldsymbol{H}$ can not induce a rigid motion of the skyrmion because there is no energy gain for it to move elsewhere. The constant field $\boldsymbol{H}_{\mathrm{R}}$ can, however, induce a deformation of the skyrmion. For example, a constant external magnetic field pointing along the z-direction perpendicular to the skyrmion plane has an effect on the skyrmion size, much like magnetic anisotropy. If this external field is alternating, the field can cause the skyrmion size to shrink and increase periodically [95], and in nanodots it can even be used to switch the magnetization of the core [96]. In our case the magnetic field experienced due to the Rashba effect lies in the skyrmion plane, and one would therefore expect it to have other deformation modes than a field pointing perpendicular to the skyrmion plane. To understand the effect of the non-uniform Rashba field proportional to $\beta \boldsymbol{M} \times \boldsymbol{H}_{\mathrm{R}}$ we can compare it to the adiabatic STT in (2.27). The term in the LLG equation can be written as $\gamma \beta \boldsymbol{M} \times (\boldsymbol{M} \times \boldsymbol{H}_{\mathrm{R}})/M_s = -(\gamma \beta C_{\mathrm{R}} b_J/M_s)\boldsymbol{M} \times (\hat{\boldsymbol{H}}_{\mathrm{R}} \times \boldsymbol{M})$. This is very similar to the adiabatic STT acting on a magnetization $\boldsymbol{M}_j$ from a current that was polarized by passing through a magnetization $\boldsymbol{M}_i$. This torque was proportional to $-\boldsymbol{M}_j \times (\boldsymbol{M}_i \times \boldsymbol{M}_j)$. With the exception of the different torque magnitudes, the only difference is that the polarizing magnetic layer $\boldsymbol{M}_i$ is replaced by the Rashba field $\boldsymbol{H}_{\mathrm{R}}$. This torque then originates from the conduction electrons that are polarized in the direction of the Rashba field. The direction of this field is given by $\hat{\boldsymbol{H}}_{\mathrm{R}} = \hat{\boldsymbol{z}} \times \hat{\boldsymbol{j}}_e$. When the current is passing in the x-direction as we have considered so far, this field points in the y-direction. As this is generates a component of the spin polarization of the current that can be perpendicular to the local magnetization, it would explain why the torque behaves as the non-adiabatic STT. We now compare the driving torque resulting from RSOC more closely to the non-adiabatic STT. The driving torque from RSOC can be written as

$$\gamma \beta \boldsymbol{m} \times (\boldsymbol{M} \times \boldsymbol{H}_{\mathrm{R}}) = \gamma \beta M_s \left((\boldsymbol{m} \cdot \boldsymbol{H}_{\mathrm{R}}) \boldsymbol{m} - \boldsymbol{H}_{\mathrm{R}} \right)$$

$$= \gamma \beta M_s C_{\mathrm{R}} b_J \begin{pmatrix} \sin^2\theta \sin\Phi \cos\Phi \\ \sin^2\theta \sin^2\Phi - 1 \\ \sin\theta \cos\theta \sin\Phi \end{pmatrix}, \tag{4.14}$$

while the non-adiabatic STT can be written as

$$-\beta b_J \boldsymbol{m} \times \left(\hat{\boldsymbol{j}}_e \cdot \nabla \right) \boldsymbol{M} = -\beta b_J M_s \begin{pmatrix} -\sin\Phi \cos\phi\partial_r\theta + \sin\theta \cos\theta \cos\Phi \sin\phi/r \\ \cos\Phi \cos\phi\partial_r\theta + \sin\theta \cos\theta \sin\Phi \sin\phi/r \\ -\sin^2\theta \sin\phi/r \end{pmatrix}, \tag{4.15}$$

where we have used that $\partial_x\theta = -\sin\phi/r\partial_r\theta$ and $\partial_x\Phi = -\sin\phi/r$. If we integrate over the skyrmion plane, the only non-vanishing components in both torques in the $\psi = 0$ case

($\mathit{\Phi} = \phi$) is the y-component. In addition, we see by performing this integration that we get the integral appearing in the RSOC term in (4.12c).

The electric field gradient introduces new terms to the velocity of the skyrmion. We can see that the skyrmion tends to move in a direction perpendicular to the electric field gradient, along $\hat{\boldsymbol{z}} \times (-\nabla E)$. In addition to the motion perpendicular to the gradient, the Gilbert damping also causes a damped motion in the opposite direction of the field gradient, moving the skyrmion to a lower energy state. The damped motion is relatively easy to understand, as it is nothing else than a relaxation of the magnetization to a lower energy. The motion of the skyrmion along the equipotential lines is a bit less intuitive, however. The reason for this motion is the Magnus force, resulting from the topology of the skyrmion. Initially the skyrmion experiences a force against the electric field gradient. At this point this is the only force acting on the skyrmion, as the Magnus force is only existent when the skyrmion moves. The skyrmion therefore drifts down to a lower energy state to begin with. However, as the the skyrmion starts to move the Magnus force kicks in, as the motion of the skyrmion induces an emergent electric field perpendicular to its motion, as described in Section 3.4. This new force changes the direction of the skyrmion motion, until the motion is such that the Magnus force and the force from the inhomogeneous energy landscape cancel out, as illustrated in Figure 4.1. The resulting motion is a Hall-like motion along the equipotential lines. This behaviour that we see from the electric field is analogous to the motion a skyrmion would have in the presence of an electric field in multiferroic insulators [97]. The mechanism behind the motion due to the electric field is different, however. In multiferroic insulators the electric field couples to the dipole moment of the skyrmion, while in this ferromagnetic metal the motion is caused by a shift in the energy landscape due to the modification of the anisotropic energy by the voltage induced magnetic anisotropy.
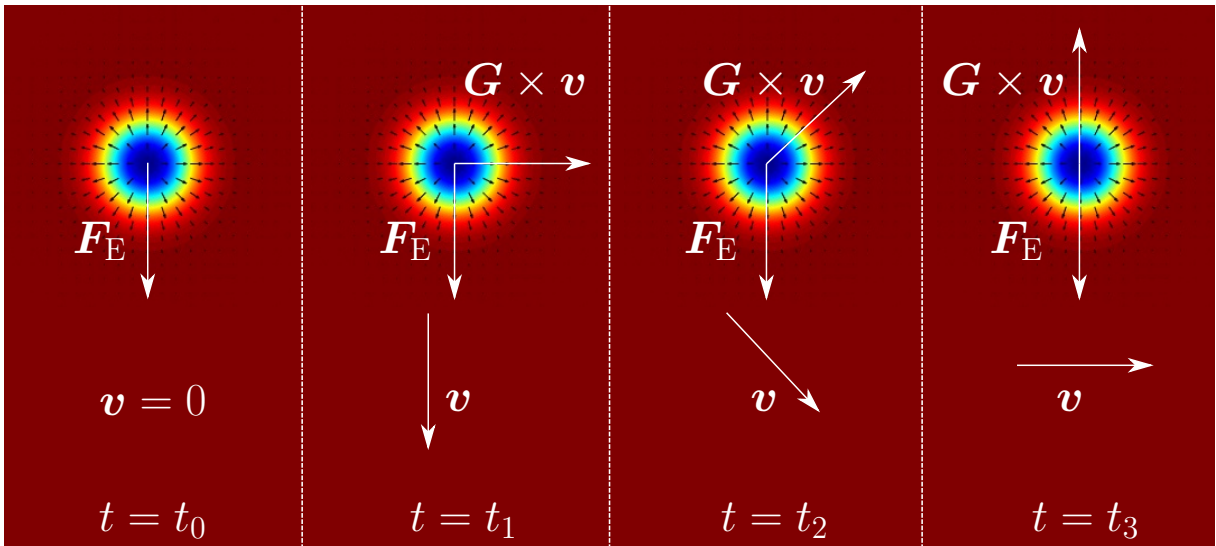
Figure 4.1. The initial motion due to the force from the spatially varying electric field is redirected due to the appearance of the Magnus force when the skyrmion starts to move. In equilibrium we have a Hall-like motion along the equipotential lines in the absence of Gilbert damping.
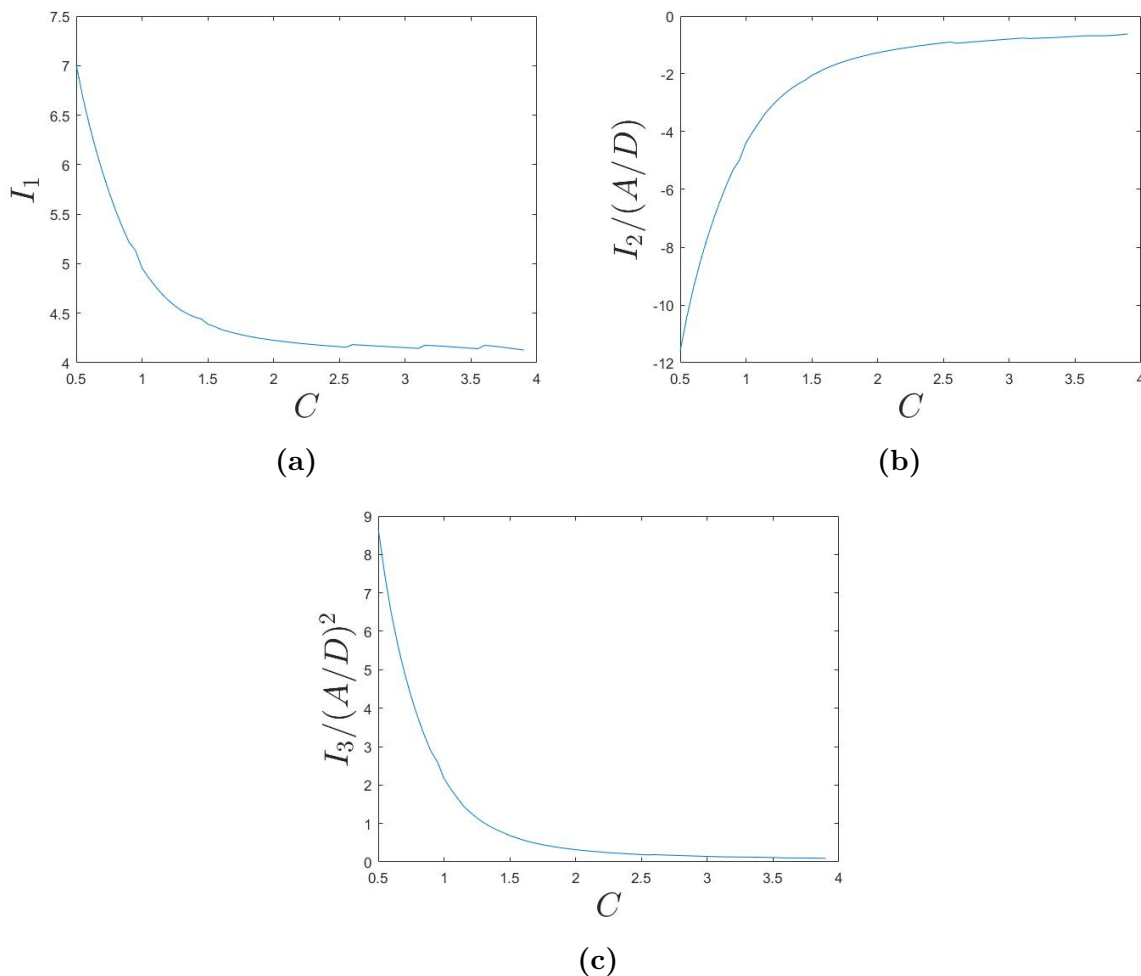
4.2 Numerical integrals

The solution of the skyrmion velocity depends on parameters that are functions of three different integrals. These integrals depend on the solution of $\theta(r)$ that is obtained numerically by solving (3.8). As our solution of θ is a numerical function, the integrals have to be calculated numerically as well. In (3.8) the only variable parameter is the skyrmion parameter $C = AK/D^2$, so the integrals can be expressed as functions of C and for some of the integrals a dimensional scaling factor. The three integrals that we need to evaluate are

$$I_1 = \int_0^\infty \mathrm{d}\tilde{r} \left(\tilde{r} \left(\frac{\partial \theta}{\partial \tilde{r}} \right)^2 + \frac{\sin^2 \theta}{\tilde{r}} \right), \tag{4.16a}$$

$$I_2 = \frac{A}{D} \int_0^\infty \mathrm{d}\tilde{r} \left(\frac{\partial \theta}{\partial \tilde{r}} \tilde{r} + \sin \theta \cos \theta \right), \tag{4.16b}$$

$$I_3 = \frac{A^2}{D^2} \int_0^\infty \mathrm{d}\tilde{r} \tilde{r} \sin^2 \theta. \tag{4.16c}$$

Here the solution of θ inside the integrals is given in the dimensionless length scale $\tilde{r} = r \cdot D/A$. The resulting integrals as functions of C are shown in Figure 4.2.

(a)

(b)

(c)

Figure 4.2. Numerical evaluations of the integrals **(a)** I_1, **(b)** I_2 and **(c)** I_3 as a function of the skyrmion parameter C.

4.3 Pinning, threshold currents and field gradients

As with domain walls, there is also a threshold current or field that is necessary for skyrmions to start moving, even though our previous results do not reflect this. In the case of skyrmions this threshold current is much weaker than the case of domain walls [22]. The reason for this reluctance to move is pinning centers, but for the motion of domain walls there is also an intrinsic pinning in the absence of pinning centers [98]. It is thought that the low threshold current for skyrmion motion can partially be attributed to the Magnus force [90], which is an additional diving force that is not present for domain walls. In addition to having a lower pinning force, skyrmions are also reluctant to be pinned when driven by large enough currents, as the Magnus force and the flexible deformation of the skyrmion enables it to move around the pinning centers [90]. To model the effect of pinning centers on skyrmion motions at low current densities or weak electric fields, one can introduce a pinning force in the Thiele equation (3.13). The equation of interest then becomes

$$\boldsymbol{F}_{\text{pin}} + \boldsymbol{F}_{\text{R}} + \boldsymbol{F}_{\text{E}} + \boldsymbol{G} \times \left(\boldsymbol{v} + b_J \hat{\boldsymbol{j}}_e \right) - D \left(\alpha \boldsymbol{v} + \beta b_J \hat{\boldsymbol{j}}_e \right) = 0. \tag{4.17}$$

The phenemenological pinning force $\boldsymbol{F}_{\text{pin}}$ is conventionally written as [99, 100]

$$\boldsymbol{F}_{\text{pin}} = -4\pi v_{\text{pin}} f(\frac{v}{v_{\text{pin}}}) \frac{\boldsymbol{v}}{v}, \tag{4.18}$$

where the function $f(\frac{v}{v_{\text{pin}}})$ goes towards unity for small skyrmion velocities v. This is to ensure that the force does not vanish as $v \to 0$, but there is a constant force barrier that the skyrmion needs to overcome to have a velocity greater than zero. In the low velocity limit one therefore approximates the pinning force by

$$\boldsymbol{F}_{\text{pin}} = -v_{\text{pin}} \frac{\boldsymbol{v}}{v}, \tag{4.19}$$

where the forces are normalized in a way so that the gyrovector $\boldsymbol{G} = (0, 0, 1)$. The non-trivial equations we then get from (4.17) are

$$-\dot{y}_0 - \beta_C b_J - \alpha_C \dot{x}_0 - v_{\text{pin}} \frac{\dot{x}_0}{v} + F_x = 0, \tag{4.20a}$$

$$b_J + \dot{x}_0 - \alpha_C \dot{y}_0 - v_{\text{pin}} \frac{\dot{y}_0}{v} + F_y = 0, \tag{4.20b}$$

where F_x and F_y are the x- and y-components of the total force $\boldsymbol{F}_{\text{R}} + \boldsymbol{F}_{\text{E}}$ resulting from Rashba spin–orbit coupling and voltage induced magnetic anisotropy respectively. In the case of $F_x = F_y = 0$, one can see that if one makes the substitution

$$\alpha_C \to \alpha_C + \frac{v_{\text{pin}}}{v} \tag{4.21}$$

the equations of motion are exactly the same as for the case of the motion of a skyrmion due to a spin-polarized current in (4.11). The solutions of $\dot{x}_0$ and $\dot{y}_0$ are known in this case, and one can therefore make the substitution of α_C above into these solutions to get the solutions in the presence of pinning:

$$\dot{x}_0 = -\frac{1 + (\alpha_C + \frac{v_{\text{pin}}}{v})\beta_C}{(\alpha_C + \frac{v_{\text{pin}}}{v})^2 + 1} b_J, \tag{4.22a}$$

$$\dot{y}_0 = \frac{(\alpha_C + \frac{v_{\text{pin}}}{v}) - \beta_C}{(\alpha_C + \frac{v_{\text{pin}}}{v})^2 + 1} b_J. \tag{4.22b}$$

As one can see, these solutions depend on the total skyrmion velocity v. To determine this velocity we use the relation $v^2 = \dot{x}_0^2 + \dot{y}_0^2$ and the solutions above, which gives us the equation

$$v^2 = \frac{\beta_C^2 + 1}{(\alpha_C + \frac{v_{\text{pin}}}{v})^2 + 1} b_J^2. \tag{4.23}$$

Rearranging this equation one can get the following second order equation in v:

$$(\alpha_C^2 + 1)v^2 + (2\alpha_C v_{\text{pin}})v + (v_{\text{pin}}^2 - (\beta_C^2 + 1)b_J^2) = 0. \tag{4.24}$$

The solution to this equation is given by

$$v = \frac{\sqrt{(\alpha_C v_{\text{pin}})^2 + (\alpha_C^2 + 1)\left[(\beta_C^2 + 1)b_J^2 - v_{\text{pin}}^2\right]} - \alpha_C v_{\text{pin}}}{\alpha_C^2 + 1}, \tag{4.25}$$

where the positive solution has been chosen as that is the only solution that can give a positive v. This solution in v differs from the solution given by Iwasaki *et al.* [100] by the term outside of the square root, but the solutions of $\dot{x}_0$ and $\dot{y}_0$ are in agreement. As our solution of v is consistent with our solutions of $\dot{x}_0$ and $\dot{y}_0$, and if one plugs our solutions into the equations in (4.20) they are satisfied in the case $F_x = F_y = 0$, it is concluded that our solutions are correct.

So far we have only discussed pinning of the spin-polarized current driven skyrmion motion, but it is also of interest to find the same results in the presence of Rashba spin–orbit coupling and an imhomogenous electric field perpendicular to the film. In other words, we must solve (4.20) when $F_x \neq 0$ and $F_y \neq 0$. We apply the same trick again where we try to incorporate F_x and F_y into similar variables in the equations we already have a solution for. F_x and F_y are both independent of $\dot{x}_0$, $\dot{y}_0$ and v, we must therefore try to include them in other terms also independent of these variables. In (4.20a) the only term independent of these is $-\beta_C b_J$, and in (4.20b) the term is b_J. If we define new variables $\tilde{\beta}_C$ and $\tilde{b}_J$ that satisfy

$$-\tilde{\beta}_C \tilde{b}_J = -\beta_C b_J + F_x, \tag{4.26a}$$

$$\tilde{b}_J = b_J + F_y, \tag{4.26b}$$

meaning they have the following definitions:

$$\tilde{\beta}_C = \frac{\beta_C b_J - F_x}{b_J + F_y}, \tag{4.27a}$$

$$\tilde{b}_J = b_J + F_y, \tag{4.27b}$$

the equations have the same form as before with $\beta_C \to \tilde{\beta}_C$ and $b_J \to \tilde{b}_J$. The total force components resulting from $\boldsymbol{F}_{\text{R}} + \boldsymbol{F}_{\text{E}}$ are

$$F_x = -C_E E_x - R b_J, \tag{4.28a}$$

$$F_y = -C_E E_y. \tag{4.28b}$$

If we plug these into $\tilde{\beta}_C$ and $\tilde{b}_J$ and make the substitutions in our previous solutions of $\dot{x}_0$, $\dot{y}_0$ and v from the current driven case, we end up with the solutions

$$\dot{x}_0 = -\frac{1 + (\alpha_C + \frac{v_{\mathrm{pin}}}{v})(\beta_C + R)}{(\alpha_C + \frac{v_{\mathrm{pin}}}{v})^2 + 1}b_J + \frac{C_E}{(\alpha_C + \frac{v_{\mathrm{pin}}}{v})^2 + 1}E_y - \frac{(\alpha_C + \frac{v_{\mathrm{pin}}}{v})C_E}{(\alpha_C + \frac{v_{\mathrm{pin}}}{v})^2 + 1}E_x, \quad (4.29\mathrm{a})$$

$$\dot{y}_0 = \frac{(\alpha_C + \frac{v_{\mathrm{pin}}}{v}) - \beta_C - R}{(\alpha_C + \frac{v_{\mathrm{pin}}}{v})^2 + 1}b_J - \frac{C_E}{(\alpha_C + \frac{v_{\mathrm{pin}}}{v})^2 + 1}E_x - \frac{(\alpha_C + \frac{v_{\mathrm{pin}}}{v})C_E}{(\alpha_C + \frac{v_{\mathrm{pin}}}{v})^2 + 1}E_y, \quad (4.29\mathrm{b})$$

$$v = \frac{\sqrt{(\alpha_C v_{\mathrm{pin}})^2 + (\alpha_C^2 + 1)\left[(\beta_C b_J + R b_J + C_E E_x)^2 + (b_J - C_E E_y)^2 - v_{\mathrm{pin}}^2\right]} - \alpha_C v_{\mathrm{pin}}}{\alpha_C^2 + 1}.$$

$$(4.29\mathrm{c})$$

It can be seen that in the limit of no pinning ($v_{\mathrm{pin}} \to 0$) the results for $\dot{x}_0$ and $\dot{y}_0$ are in agreement with (4.13). From the expression for v in (4.29c) it is also possible to determine the threshold current or electric field gradient necessary for the solution of v to be greater than zero. If we first consider the case where the skyrmion motion is solely driven by a spin-polarized current, one finds that the skyrmion moves when $b_J > b_J^{(\mathrm{crit})}$ with

$$b_J^{(\mathrm{crit})} = \frac{1}{1 + \beta^2}\frac{\mu_B P}{e M_s}j_e^{(\mathrm{crit})} = \frac{v_{\mathrm{pin}}}{\sqrt{(\beta_C + R)^2 + 1}}. \quad (4.30)$$

To determine the strength of the Rashba parameter α_{R} we use the relation in (2.18), which gives α_{R} in terms of the strength of the DMI and exchange interaction. In the field driven case where the skyrmion motion is solely driven by an inhomogenous electric field applied perpendicular to the film, one finds that the skyrmion moves when the field gradient magnitude $E_g = \sqrt{E_x^2 + E_y^2}$ is greater than some critical value

$$E_g^{(\mathrm{crit})} = \frac{v_{\mathrm{pin}}}{C_E}. \quad (4.31)$$

The numerical values of $b_J^{(\mathrm{crit})}$ and $E_g^{(\mathrm{crit})}$ for different values of the skyrmion parameter C are shown in Figure 4.3. As one can see, the behavior of the critical current and field gradient are quite different. The critical current is a strictly decreasing function of C, but the decrease is only significant for high values of β. The critical field gradient, however, is a strictly increasing function of C, and increases significantly from $C = 0.5$ to $C = 2.5$. If the unit length A/D is kept constant, the size of the skyrmion decreases with increasing C (which can be seen from Figure 3.2). Still assuming that A/D is kept constant, one sees that in the current driven case smaller skyrmions have a lower critical current, while in the electric field driven case larger skyrmions have a lower critical field gradient. This can be understood rather intuitively. The non-adiabatic spin-transfer torque acts as a drag force on the skyrmion in the Thiele equation. This drag force attempts to move the skyrmion in the direction of the conduction electrons. Normally the total non-adiabatic STT is larger for larger skyrmions, but with the presence of RSOC we get an effectively reduced non-adiabatic STT. This reduction is greater for larger skyrmions due to the larger area where the conduction electrons polarized along the Rashba field can transfer their spin to the local magnetization. Because of this effective reduction of the non-adiabatic STT larger skyrmions experience less drag along the motion of the conduction electrons, and smaller skyrmions then require a smaller current to be moved than large ones. If RSOC was not present the situation would be reversed, as there is no reduction of the drag resulting from

non-adiabatic STT, and larger skyrmions would have a lower critical current due to the larger drag force acting on them. For the electric field driven case the spatial variation of the free energy has a larger impact on a large skyrmion than a small skyrmion.
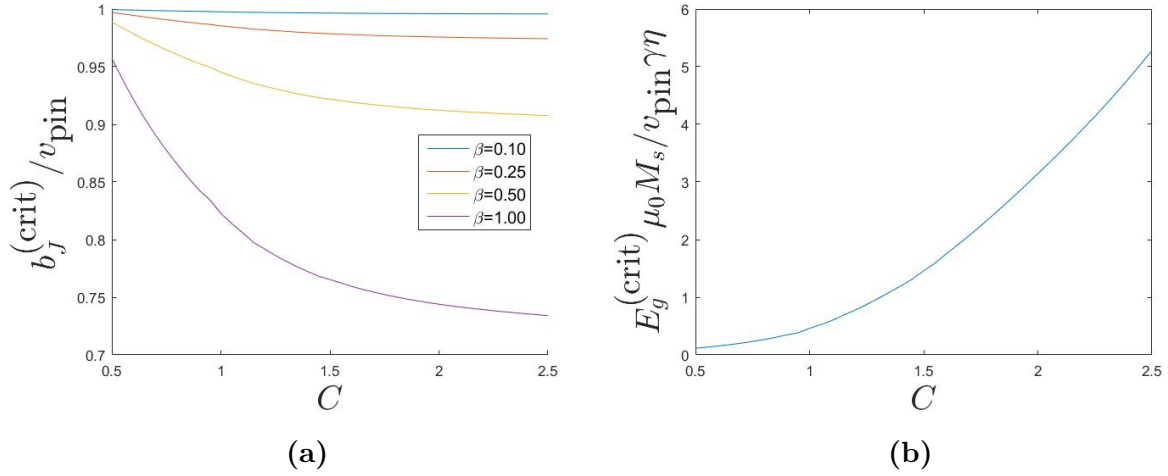
Figure 4.3. **(a)** The critical current density and **(b)** the critical field gradient as a function of the skyrmion parameter C.

4.4   Numerical simulations

In our analytical calculations in the previous sections we have solved the Thiele equation, which is a simplification of the LLG equation. The Thiele equation assumes that we have a rigid motion of the skyrmion, so that the motion of the skyrmion can be described by the motion of a key feature of the magnetization pattern such as the skyrmion core. Because of this, the Thiele equation can not describe whether the skyrmion becomes deformed during its motion or not. In some of the cases we have considered so far it is likely that there will at least be certain deformation of the skyrmion profile. The presence of RSOC and application of an electric field gradient to the system will cause the magnetization to experience magnetic fields that are not aligned with the effective field that stabilizes the skyrmion. To judge if our analytical results have any merit, we therefore solve the LLG equation numerically where we make no assumptions regarding the rigidness of the skyrmion motion. We can then compare our analytical results in the Thiele framework with the numerical results in the LLG framework to see if a rigid motion is a good approximation or not.

4.4.1   The LLG equation as a parabolic equation

The LLG equation is a partial differential equation that is first order in time, and contains first and second order spatial derivatives through the effective field from DMI and the exchange interaction in the skyrmion case. It should then be possible to write the LLG equation on the following form:

$$\bar{d}\dot{\boldsymbol{m}} - \nabla \cdot (\bar{\boldsymbol{c}} \otimes \nabla \boldsymbol{m}) + \bar{a}\boldsymbol{m} = \boldsymbol{f}. \tag{4.32}$$

Here $\boldsymbol{m}$ and $\boldsymbol{f}$ are vectors of length N, $\bar{d}$ and $\bar{a}$ are $N \times N$ matrices, and $\bar{\boldsymbol{c}}$ is a $N_{\text{dim}} \times N_{\text{dim}} \times N \times N$ tensor. For the case of the skyrmion, we have three magnetization components

we need to solve for in a 2D plane, in other words $N = 3$ and $N_{\dim} = 2$. Equations on the form given by (4.32) are solved by the `parabolic` function in MATLAB's `PDE Toolbox`, which utilizes a finite element method. We then need to rewrite (4.1) to the form of (4.32). This was done and provided the following results:

$$\boldsymbol{f} = \begin{pmatrix} b_J\partial_x m_x - \beta b_J(m_y\partial_x m_z - m_z\partial_x m_y) + 2(m_y\partial_x m_x + m_y\partial_y m_y + m_z\partial_y m_z)\gamma D/(\mu_0 M_s) \\ b_J\partial_x m_y - \beta b_J(m_z\partial_x m_x - m_x\partial_x m_z) - 2(m_z\partial_x m_z + m_x\partial_x m_x + m_x\partial_y m_y)\gamma D/(\mu_0 M_s) - \beta H_{\mathrm{R}} \\ b_J\partial_x m_z - \beta b_J(m_x\partial_x m_y - m_y\partial_x m_x) - 2(m_x\partial_y m_z - m_y\partial_x m_z)\gamma D/(\mu_0 M_s) \end{pmatrix},$$

$$(4.33\mathrm{a})$$

$$\bar{d} = \begin{pmatrix} 1 & \alpha m_z & -\alpha m_y \\ -\alpha m_z & 1 & \alpha m_x \\ \alpha m_y & -\alpha m_x & 1 \end{pmatrix}, \tag{4.33b}$$

$$\bar{a} = \begin{pmatrix} -\gamma\beta H_{\mathrm{R}} m_y & 2\gamma(K+\eta E)m_z/(\mu_0 M_s) & -\gamma H_{\mathrm{R}} \\ -2\gamma(K+\eta E)m_z/(\mu_0 M_s) & -\gamma\beta H_{\mathrm{R}} m_y & 0 \\ \gamma H_{\mathrm{R}} & 0 & -\gamma\beta H_{\mathrm{R}} m_y \end{pmatrix}, \tag{4.33c}$$

$$\bar{\boldsymbol{c}} = \begin{pmatrix} \bar{0} & 2\gamma A m_z\bar{I}/(\mu_0 M_s) & -2\gamma A m_y\bar{I}/(\mu_0 M_s) \\ -2\gamma A m_z\bar{I}/(\mu_0 M_s) & \bar{0} & 2\gamma A m_x\bar{I}/(\mu_0 M_s) \\ 2\gamma A m_y\bar{I}/(\mu_0 M_s) & -2\gamma A m_x\bar{I}/(\mu_0 M_s) & \bar{0} \end{pmatrix}, \tag{4.33d}$$

with $\bar{0}$ being a 2×2 matrix of zeros, and $\bar{I}$ the two-dimensional identity matrix. The i-th component of $\nabla \cdot (\bar{\boldsymbol{c}} \otimes \nabla \boldsymbol{m})$ is defined as

$$[\nabla \cdot (\bar{\boldsymbol{c}} \otimes \nabla \boldsymbol{m})]_i = \sum_{j=1}^{N} (\partial_x c_{i,j,1,1}\partial_x + \partial_x c_{i,j,1,2}\partial_y + \partial_y c_{i,j,2,1}\partial_x + \partial_y c_{i,j,2,2}\partial_y)\, m_j. \tag{4.34}$$

4.4.2   Dimensional analysis

When performing the numerical simulations it is necessary to do this using dimensionless quantities. We therefore need to define a unit length- and time-scale for the system based on our parameters. For the unit length-scale we continue to use the one defined in the numerical solution of the skyrmion profile in Section 3.1, which was $\tilde{r} = rD/A$. The unit length scale is therefore $\underline{r} = A/D$. For the time-scale of the system we choose one such that $\underline{t}\gamma K/\mu_0 M_s = 1$, in other words $\underline{t} = \mu_0 M_s/\gamma K$. We now use these definitions to find the scalings of the remaining parameters. The parameter b_J is a velocity factor, and when its dimensionless counterpart is unity it takes on the value $\underline{r}/\underline{t} = \gamma AK/D\mu_0 M_s$. Moving on to the effective field terms from the DMI and exchange interaction, we need to consider spatial derivatives. These derivatives needs to be done in a dimensionless space. We can then see from the chain rule that $\partial_x = \underline{r}^{-1}\partial_{\tilde{x}}$. Each derivative will then carry with it a factor D/A for the derivative to be done in dimensionless coordinates. We then note that the effective field originating from DMI has one spatial derivative, while the effective field originating from the exchange interaction has a double spatial derivative. As $A(D/A)^2 = D(D/A) = K/C$ these fields scale similarly in our dimensionless space. Since we have defined $\underline{t}\gamma K/\mu_0 M_s = 1$, we simply divide these effective fields by the factor $C = AK/D^2$ to get the right scaling. Lastly we consider the scaling of the Rashba field H_{R}. Due to the definition of the time-scale we must require that the dimensionless value of γH_{R} to be unity when $H_{\mathrm{R}} = K/\mu_0 M_s$, which is the measure of field strength chosen in our simulations. A summary of the dimensional scalings is shown in Table 4.1.

Table 4.1. List of dimensionless quantities utilized in the numerical simulation and the scaling factor to get the correct unit and magnitude of the physical quantity.

| Dimensionless quantity	Proper unit	Scaling factor
t	s	$\mu_0 M_s/\gamma K$
r	m	A/D
b_J	m/s	$\gamma K A/\mu_0 M_s D$
H_{R}	A/m	$K/\mu_0 M_s$
$D\partial_{\tilde{x}}$	J/m^3	D^2/A
$A\partial_{\tilde{x}}^2$	J/m^3	D^2/A

In Table 4.2 we list some parameter values for a Ir|Co|Pt multilayer system [101] and 1 nm thick cobalt nanotracks [102]. The value of α_{R} is determined by using the values of A, D and other physical constants in the relation (2.18).

Table 4.2. Table of physical quantities for a Ir|Co|Pt multilayer system and 1 nm thick cobalt nanotracks.

| Quantity	Unit	Ir|Co|Pt	Cobalt
A	pJ/m	10	15
D	mJ/m^2	1.75	4
K	MJ/m^3	0.17	0.8
M_s	MA/m	0.96	0.58
α_{R}	peV·m	3.3	5.1

4.4.3 Static case

As a test case we will first solve the LLG equation without any driving torques or fields as given by (2.22), where we give in the skyrmion profile solved numerically as an initial state. As the magnetization of the skyrmion is parallel with the effective field, which is why the skyrmion is a stable solution, we would expect the solution to be static ($\boldsymbol{M}(\boldsymbol{r}, t) = \boldsymbol{M}(\boldsymbol{r}, t = 0)$). The results are shown in Figure 4.4. At a time $t = \underline{t}$ (which is ~ 4 ps for the cobalt nanotracks and ~ 32 ps for the Ir|Co|Pt multilayer system) there is not much change in the solution, but there is a slight counterclockwise rotation of the m_x and m_y values. After a time $t = 10\underline{t}$, however, the solution has smeared out significantly from the initial state. More importantly, the values of the vector components exceed the allowed interval $[-1, 1]$ by far, thereby breaking the normalization $m_x^2 + m_y^2 + m_z^2 = 1$ of the system. The LLG equation explicitly conserves the magnitude of the magnetization, so this is of particular interest when considering the stability of the code. Although we have three equations that we solve numerically, they are not independent of each other, as we can find the third vector component up to a sign once we have the solution of two. The numerical simulation does not seem to handle this well enough after a certain time, however. It is therefore a clear indication that the implemented solution method is not stable enough. There are several things that could cause this. If the boundary conditions are chosen incorrectly, this could affect the system. For this simulation Dirichlet boundary conditions corresponding to the numerical skyrmion solution at each point were chosen, and should therefore not affect the solution under the assumption that there is no dynamics. Another
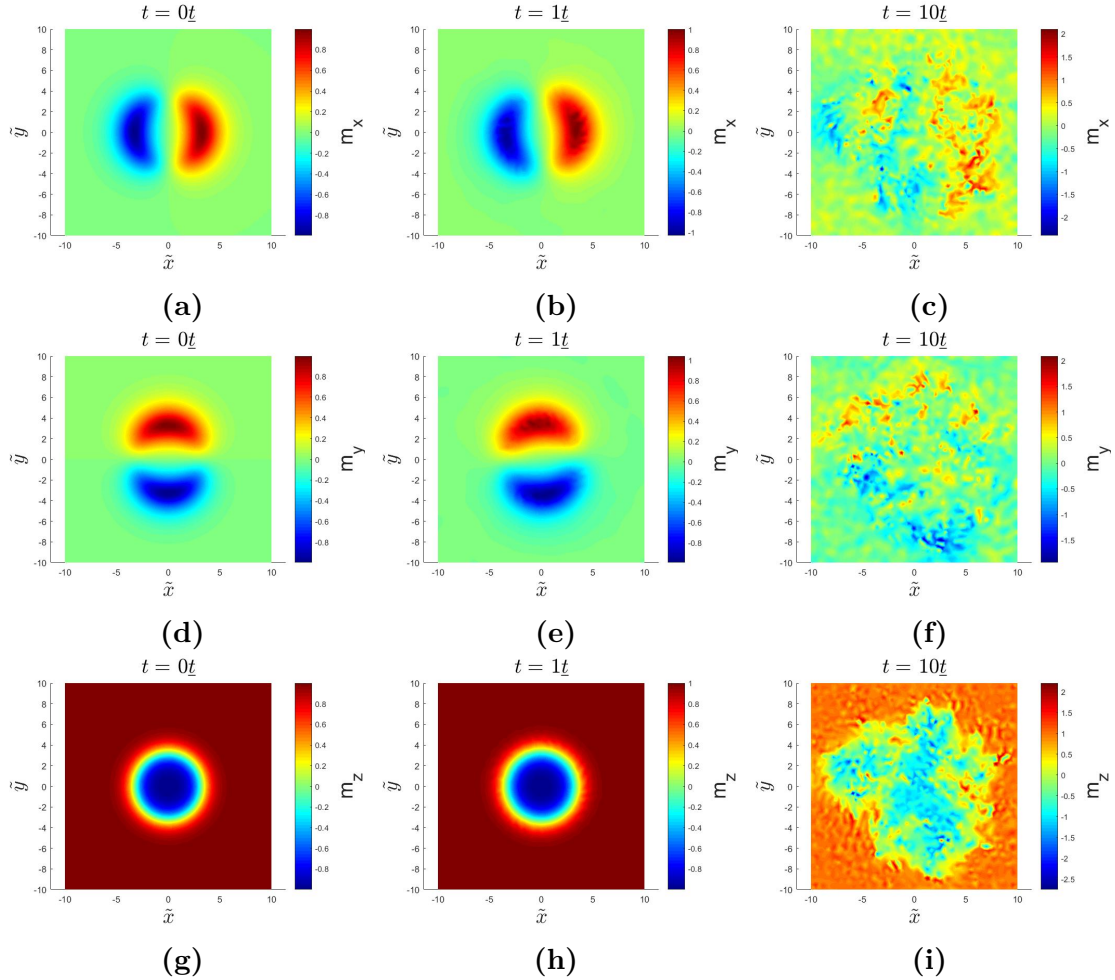
Figure 4.4. Plots of the vector components m_x, m_y and m_z in the skyrmion plane for different times in the numerical simulation. The first row contains the data for m_x, the second for m_y and the third for m_z. The first column shows the initial state, the second at a time $t = \underline{t}$ and the third at a time $t = 10\underline{t}$.

possible source of the instability is how the initial conditions are handled. The out of plane angle θ in the skyrmion profile has to be determined numerically from (3.8). This is a differential equation with a singular point at $\tilde{r} = 0$, and we therefore settle by solving the equation down to a value close to zero. The solution of θ will also be needed arbitrarily close to zero, or at zero itself, when considering the entire skyrmion. A quick fix to this problem is shifting the $\tilde{r}$-values of the numerical solution of θ so that the θ values start at $\tilde{r} = 0$ instead of $\tilde{r} = \epsilon$ (with ϵ here being set to 10^{-4}). This is not a particularly good solution to the problem, as it introduces a small off-set to the solution of θ that will make the skyrmion profile not perfectly aligned with the effective field. However, as this off-set is so small, it is expected that any dynamics this will induce in the LLG equation will primarily go towards stabilizing the skyrmion to its proper stable form. What is more important about this fix is that it makes the function $\theta(\tilde{r})$ well defined at all points, so that $\boldsymbol{m} = (\sin\theta\cos\Phi, \sin\theta\sin\Phi, \cos\theta)$ is defined at all points in the skyrmion plane. To check if this fix is sufficient, we study the first and second derivatives of the magnetization, which appear in the effective field. The results are shown in Figure 4.5. As one can see, we still have an issue with discontinuities in the derivatives. For the $m_x = \sin\theta\cos\Phi$ case this could possibly stem from the $\cos\Phi$ factor, as Φ is not properly defined at $\tilde{r} = 0$. As the

(a)

(b)

(c)

(d)
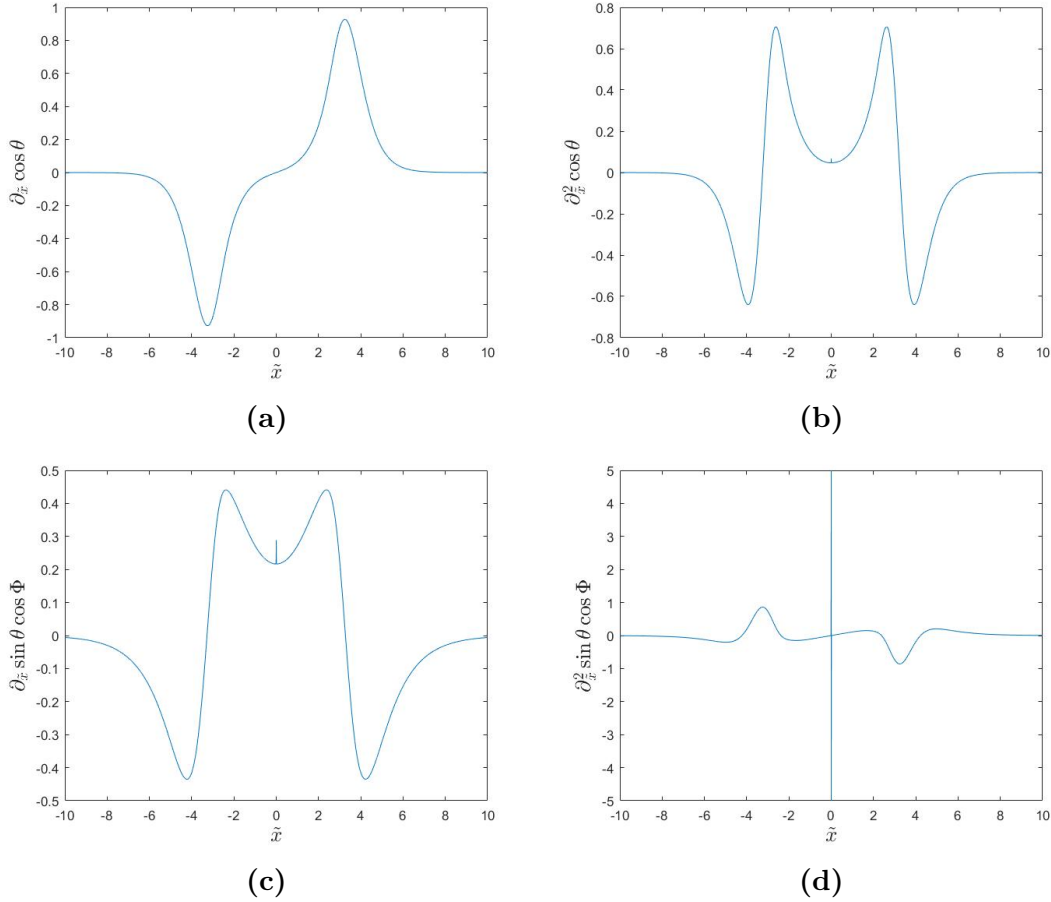
Figure 4.5. First and second derivatives of m_x and m_z in the x-direction. Every derivative has a discontinuity at $\tilde{x} = 0$ except for the first derivative of m_z. The second derivative of m_x has a singularity at $\tilde{x} = 0$.

first derivative of m_x has a discontinuity while the first derivative of m_z does not, and m_z is independent of Φ, it would back up this hypothesis. However, as $\sin\theta(\tilde{r} = 0) = 0$ a value for Φ at this point should not be necessary. But we also see that our fix of the θ solution can not be without problems, as we also have a discontinuity in the second derivative of m_z, and this must stem from how we handle θ. These discontinuities could therefore be an explanation for the instability in our numerical simulations. The most likely sinner in this hypothesis is the second derivative of m_x, which appears to have a singularity at $\tilde{r} = 0$. This singularity most likely originates from the derivatives of Φ, as the discontinuity in the second derivative of m_z is rather small. A last possible explanation for the instability is that while the LLG equation should conserve the magnitude of $\boldsymbol{m}$ by default due to the form of the equation, there is no explicit constriction in the solver that requires that $m_x^2 + m_y^2 + m_z^2 = 1$. As the numerical solutions are based on approximations, if there is a small perturbation that makes $m_x^2 + m_y^2 + m_z^2 \neq 1$ the solver will not necessarily attempt to adjust the magnitude of $\boldsymbol{m}$ back to unity, and this perturbation can then increase until the components of $\boldsymbol{m}$ reach unrealistic values. From this point on the results of the simulation are of absolutely no interest, as the input to the next time step is outright wrong.

4.4.4 Spin-transfer torque driven dynamics

In the previous subsection we saw that the numerical simulation proved to be unstable even in a case that should involve no dynamics. However, up to the time $t = \underline{t}$ it was more or less stable, with some deformations of the initial state that should not be present. Despite the fact that the results yielded by the simulations can not be relied entirely upon, even up to this time, we will attempt to introduce some dynamical terms in the LLG equation and solve this to a time $t = \underline{t}$ and compare this with our analytical results. While the quantitative behavior may be too inaccurate for us to judge if the numerical results agree with our analytical ones, hopefully we can still see if the qualitative behavior is the same. The first test we do is on a skyrmion with $A = 10\,\mathrm{pJ/m}$, $K = 0.17\,\mathrm{MJ/m^3}$,
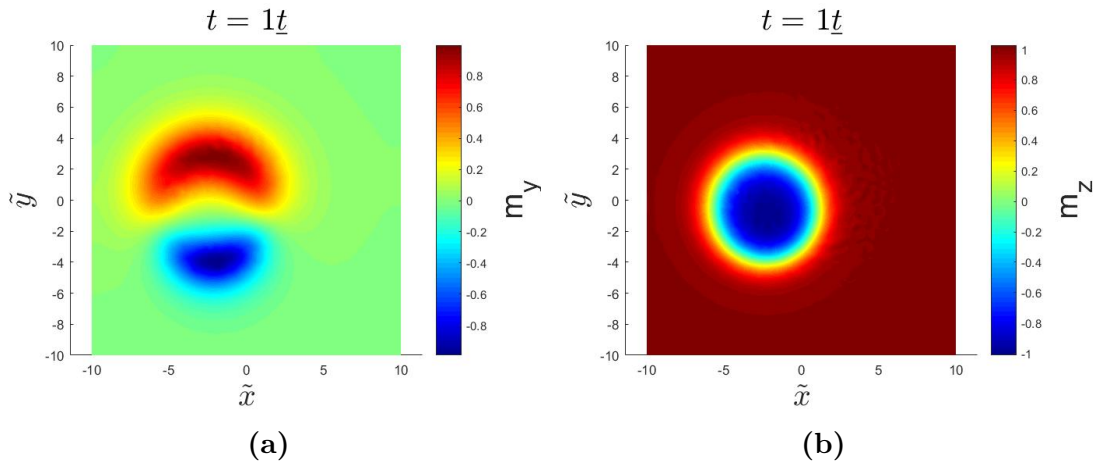
Figure 4.6. Plots of m_y and m_z at a time $t = \underline{t}$ for a skyrmion driven by spin transfer torques. The skyrmion considered has $C = 0.5551$ and the applied current gives a characteristic velocity $b_J \approx 178$ m/s ($b_J = 1$ in dimensionless units). The values of the damping parameters were set to $\alpha = 1.0$ and $\beta = 3.0$. The geometric center of the skyrmion is found to be approximately $(-2.20, -0.85)$ from the plot of m_z.

$D = 1.75$ mJ/m^2, $M_s = 0.96$ MA/m. The characteristic velocity b_J due to the spin transfer torque from the current is set to be unity in dimensionless units. Lastly we choose large damping parameter values ($\alpha = 1.0$ and $\beta = 3.0$) to make the impact of the different types of STT clear. The results are shown in Figure 4.6. While there is a clear deformation of the m_y component, the m_z component has more or less undergone a rigid motion, and all the magnetization components have reasonable values in the range $[-1, 1]$. By looking closely at the plot of m_z one can find that the location of the skyrmion core is approximately $(-2.20, -0.85)$. Using our analytical model in (4.13) we would expect the core to be at $(-2.47, -0.88)$. The numerical result is then rather close to what we would expect from our analytical model. The discrepancy can perhaps be due to the deformation of the m_y component, as our analytical model was made under the assumption of a rigid motion of the skyrmion. Whether the deformation is something that would actually occur in the physical case is not something we can say with accuracy, as we have already determined in the last subsection that the simulations give some deformations in cases where there should be none. In any case, the result we get agrees very well qualitatively with our analytical ones. We have a main velocity component along the direction of the conduction electrons, and also a component perpendicular to the current direction due to the skyrmion Hall effect as $\alpha \neq \beta$. When $\alpha = \beta$, however, we expect this perpendicular component from the skyrmion Hall effect to vanish. To check this we run a simulation with

similar parameters as before, except now we set $\alpha = \beta = 1$. The analytical model would now expect the skyrmion to have a velocity $\boldsymbol{v} = -b_J \hat{\boldsymbol{x}}$. The m_z component resulting from this simulation is presented in Figure 4.7, and its center is at $(-1, 0)$, in complete agreement with our analytical model. In addition, we do not have any deformations of significant magnitude in any of the magnetization components.

$$t = 1\underline{t}$$
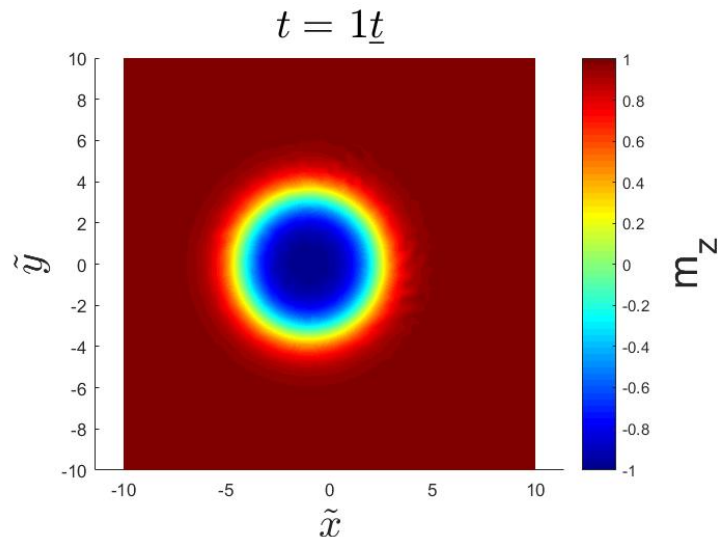
Figure 4.7. Plot m_z at a time $t = \underline{t}$ for a skyrmion driven by spin transfer torques. The skyrmion considered has $C = 0.5551$ and the applied current gives a characteristic velocity $b_J \approx 178$ m/s ($b_J = 1$ in dimensionless units). The values of the damping parameters were set to $\alpha = \beta = 1.0$. The geometric center of the skyrmion is found to be $(-1, 0)$ from the plot of m_z.

4.4.5 The effects of RSOC on the current driven dynamics

We now move on to check the effects of RSOC on the dynamics of the skyrmion. It turns out that there is no time in the simulation that is large enough to see these effects that does not break the normalization of the magnetization to a significant degree. These values outside of the range $[-1, 1]$ are local, however, so we still attempt an analysis. Before we start the analysis it should be noted that the results shown and discussed in this section should be taken with a grain of salt, as the code shows clear signs of instability. As this instability also appears at $t = \underline{t}$, and does not increase significantly at $t = 2\underline{t}$, we run our simulation up to $t = 2\underline{t}$ in this subsection. The dynamical effects of RSOC only appears when we have an applied current in the material. To see its effects it is therefore best to compare the current driven dynamics of a skyrmion in a material with and without RSOC. The strength of DMI is set to be the same in both systems, despite the fact that the presence of RSOC will influence this. This is done so that we consider skyrmions of equal size, and the only difference between their dynamics will then be the effects of RSOC. For this simulation we use the data for the cobalt nanotracks in Table 4.2, and apply a current in the x-direction corresponding to $b_J = 1$ in its dimensionless value. We let the damping constants take on large values $\alpha = \beta = 1$ for it to be easier to recognize the effects of RSOC, as it is expected that the RSOC correction is proportional to β. The simulation results are shown in Figure 4.8. The first thing we notice is that there is significantly more deformation in the system with RSOC than the one without. This could again be due to the instability of the code, having RSOC present in the LLG equation makes the

equations harder to solve. However, RSOC appears as fields in the LLG equation, and for large currents these fields can reach an order of magnitude comparable to the effective field. It is therefore not that unexpected that RSOC causes a deformation of the skyrmion, as the skyrmion magnetization profile is no longer perfectly aligned with the experienced magnetic field. The second thing one notices is that the location of the skyrmion core is not the same in the material with RSOC and the one without. The presence of RSOC shifts the core in the positive x- and y-direction. This is behavior that is similar to what is predicted by (4.13) (remember that R is negative for positive α_{R} and b_J). Analytically the core should be located at $(-1.17, 0.29)$ in the presence of RSOC, while numerically the core is approximately found to be located at $(-0.90, 0.35)$. The results are not that different, and can possibly be due to the deformation of the skyrmion or the instability of the code. What is most important to note is that the qualitative effects of RSOC on the current driven skyrmion dynamics agree rather well with one another.

4.4.6   Electric field driven dynamics

The last effect to check numerically is then the dynamics induced by an inhomogeneous electric field applied perpendicular to the skyrmion plane. The problem with simulating these effects is that for reasonably scaled electric field gradients, such that the overall change in the free energy in the vicinity of the skyrmion is rather small, the time scale needed to see the effects is quite large compared to $\underline{t}$. At these time scales we have seen that the simulations become unstable, and this instability renders any output we may get useless. To get a motion of the skyrmion that we can see at a time scale $\underline{t}$ we can, however, use a very steep electric field gradient. The ones used in these simulations were set so that $\eta E_{x/y}\underline{r} = 0.2K$. This method is not entirely unproblematic either, not even considering that this is a much stronger modification of the anisotropic energy than we can accomplish with an electric field. With a gradient this steep there is a considerable change in the free energy. If we consider the example with $\eta E_x \underline{r} = 0.2K$ the total anisotropic energy at $\tilde{x} = -5$ is zero, while at $\tilde{x} = 5$ is twice that of the original anisotropic energy without an applied electric field. This should cause noticeable deformations in the skyrmion, as the change in the effective field becomes so great that the magnetization of the skyrmion is not even close to being the stable solution. For small time scales these deformations will hopefully not be that dominant, however. There are two effects we would like to check for the electric field driven motion of the skyrmion; in the undamped limit the skyrmion should move perpendicular to the electric field gradient, while in the presence of damping there should also be a velocity component in the opposite direction of the gradient. We therefore run simulations for two different values of α for each gradient direction. We choose a value $\alpha = 0.01$ that should show primarily the motion in the undamped case, and a value $\alpha = 0.7$ to introduce the velocity component due to damping. The value of $\alpha = 0.7$ is chosen to get the maximum velocity component in the opposite direction of the field gradient. This happens when $\alpha_C = 1$, which would correspond to $\alpha = 0.7$ for a skyrmion with $C = 0.75$, as we get when using the values for the cobalt nanotracks in Table 4.2. The simulation results for the m_z component at a time $t = 2\underline{t}$ are shown in Figure 4.9. As we can see there is some deformation of the skyrmion, primarily an elongation along the axis where we apply an electric field gradient. If one studies the plots closer, one can also see that the position of the core has moved slightly, although this is hard to see directly from the plots as presented here.

We will now compare the analytical and numerical core positions using (4.13) and
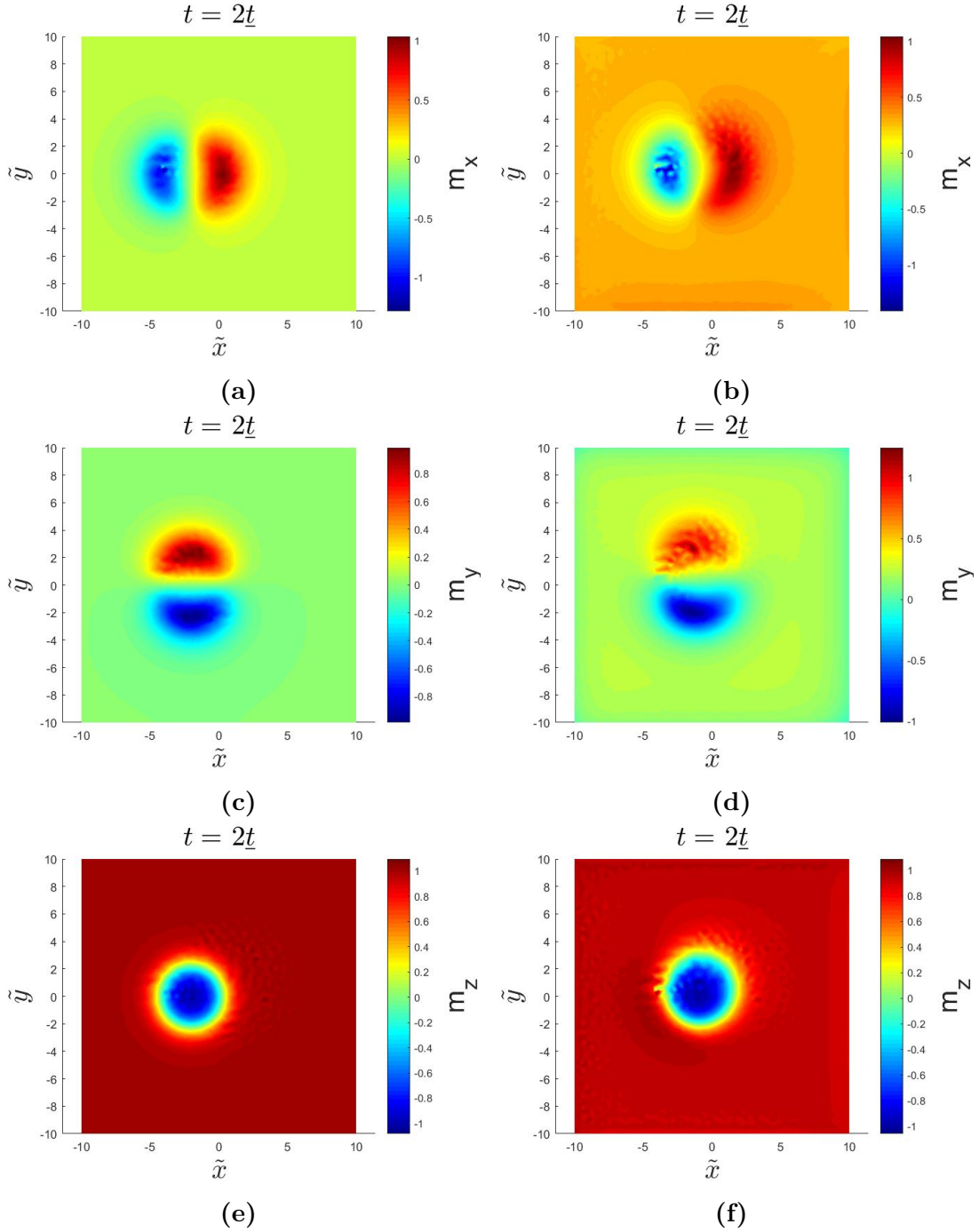
Figure 4.8. $\alpha_{\mathrm{R}} = 5.1$ peV·m, $b_J = 1$, $C = 0.75$, $\alpha = \beta = 1$. The skyrmion core is located at $(-2, 0)$ without RSOC, and at approximately $(-0.90, 0.35)$ with RSOC.

Figure 4.9. The analytical core locations are given by $(-0.01, -0.86)$ and $(-0.43, -0.43)$ for a gradient in the x-direction and a damping parameter $\alpha = 0.01$ and $\alpha = 0.7$ respectively. For a gradient in the y-direction the locations are $(0.86, -0.01)$ and $(0.43, -0.43)$ for $\alpha = 0.01$ and $\alpha = 0.7$ respectively. The analytical results are in good agreement with the velocity component perpendicular to the gradient found numerically, but there is some discrepancy in the velocity component in the opposite direction of the gradient that is proportional to α. Qualitatively the damped velocity component behaves correctly, but quantitatively it is a bit off comparing to the perpendicular velocity component. This

could possibly stem from the elongation of the skyrmion along the gradient axis, as the core is chosen to be where the m_z component is minimal, but this is no longer the geometric center of the skyrmion.
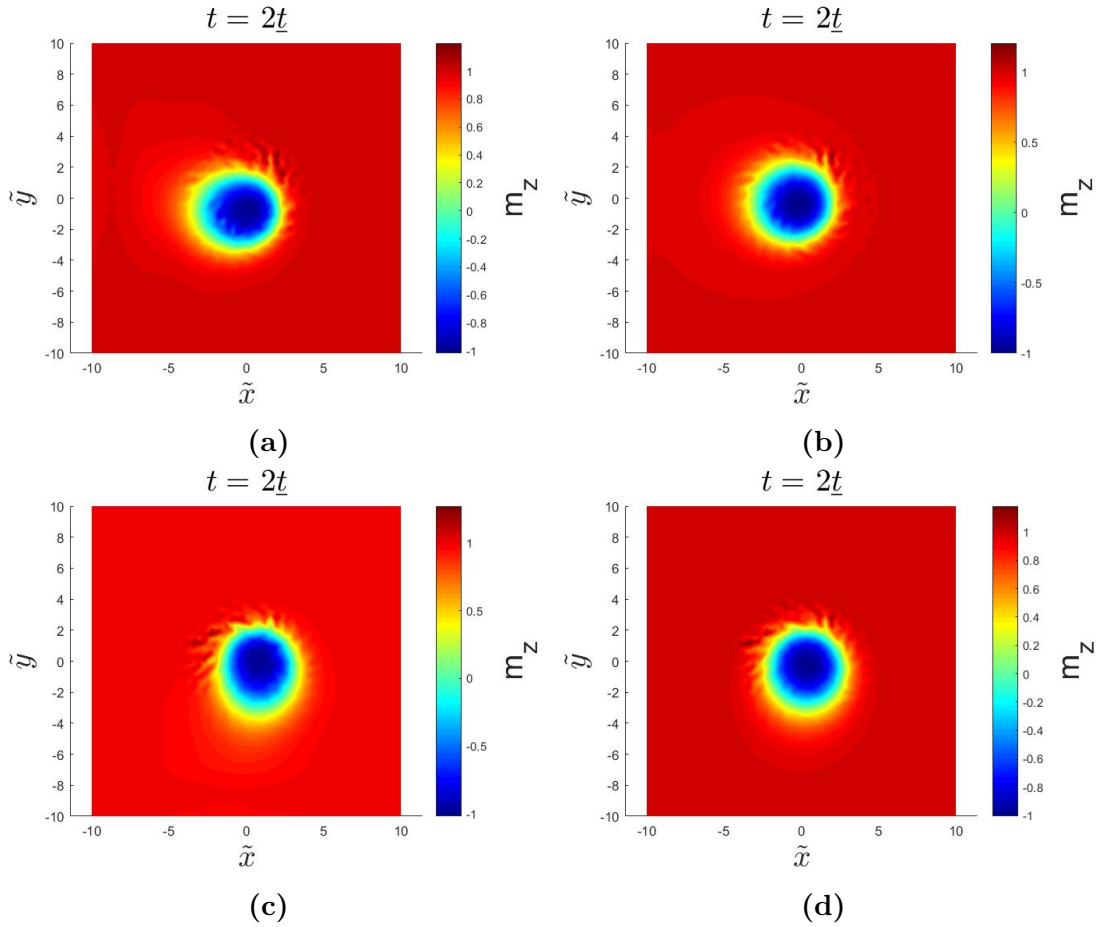
Figure 4.9. The m_z component of a skyrmion with $C = 0.75$ at a time $t = 2\underline{t}$ after applying an electric field gradient to the system at $t = 0$. In **(a)** and **(b)** we have applied a gradient E_x in the x-direction, while in **(c)** and **(d)** we have applied a gradient E_y in the y-direction. The electric field is given by $E = (E_x x + E_y y)\hat{z}$, and the field strength is given by $\eta E_{x/y}\underline{r} = 0.2K$, where we have used the materialistic properties of cobalt nanotracks. In **(a)** and **(c)** the damping parameter is $\alpha = 0.01$, while in **(b)** and **(d)** it is $\alpha = 0.7$. The core locations are found to be approximately **(a)** $(0, -0.75)$, **(b)** $(-0.2, -0.4)$, **(c)** $(0.75, 0)$, **(d)** $(0.4, -0.2)$.

As a final comment on the electric field control of the skyrmion motion we would like to discuss what is a realistic size of the electric field gradient, and how this may be utilized in skyrmion motion. By rewriting (4.13), we can express the electric field gradients as

$$E_x = -\frac{1}{C_E}\left[(\beta_C + R)\,b_J + \alpha_C \dot{x}_0 + \dot{y}_0\right], \tag{4.35a}$$

$$E_y = \frac{1}{C_E}\left[b_J + \dot{x}_0 - \alpha_C \dot{y}_0\right]. \tag{4.35b}$$

One use of the electric field control of the skyrmion motion is to cancel out the perpendicular velocity component when the skyrmion is dynamically driven by a spin-polarized current. We can then estimate the size of the gradient necessary to accomplish this based on the expression above. For simplicity we assume a case with $\alpha = 0$, so that the $\dot{y}_0$

component can be cancelled out by an electric field gradient in the x-direction alone. The value of β needs to be nonzero for us to have a nonzero $\dot{y}_0$ to cancel out. In this example we let $\beta = 0.01$ for reference, and we note that the field gradient scales linearly with β. The magnitude of the electric field gradient in the x-direction necessary to make $\dot{y}_0$ vanish then becomes

$$\eta E_x \underline{r} = -\frac{2\mu_0 M_s \underline{r}}{\gamma' I_3} \left(\beta_C + R\right) b_J. \tag{4.36}$$

For a current density $j_e = 10^{10}$ A/m^2 the size of b_J is approximately 1 m/s. In the cobalt nanotrack case, we would then require an electric field gradient of the magnitude $\eta E_x \underline{r}/K = -2.8 \cdot 10^{-6}$ to cancel out the perpendicular velocity component, while for the Ir|Co|Pt multilayer system we would require $\eta E_x \underline{r}/K = -1.2 \cdot 10^{-5}$. This is a much more feasible field gradient than the one used in the numerics to illustrate the dynamics (which was $\eta E_x \underline{r}/K = 0.2$), as it does not require a very considerable change in the perpendicular magnetic anisotropy. In addition, as the free energy is slowly varying in the vicinity of the skyrmion, it is unlikely to cause any deformations of significance.

5
Spin torque oscillators

In this chapter we will cover the second topic of this thesis, which is spin torque oscillators. These oscillators are realized by a magnetic multilayer system, where the free magnetic moments in the system can undergo self-sustained oscillations. Due to the giant magnetoresistance effect this causes a temporally varying resistance of a current passing through the multilayer system, allowing us to generate an alternating current by applying a direct current to the system. Like the magnetization dynamics of the skyrmion, these self-sustained oscillations can be described by a variation of the LLG equation, known as the Landau–Lifshitz–Gilbert–Slonczewski (LLGS) equation. Because of the geometry of the multilayer system, it is possible to induce a Rashba spin–orbit coupling due to the broken inversion symmetry. The effect of this spin–orbit coupling on the spin torque oscillator in such a multilayer system has to date not yet been explored, and is the purpose of this chapter. We will in this chapter perform analytical and numerical calculations on the system when RSOC is present, and find an analogous description of this effect comparing it to well known effects.

5.1   Giant magnetoresistance

An important effect that is fundamental for the spin torque oscillators is the giant magnetoresistance (GMR) effect. This effect was discovered by Albert Fert [6] and Peter Grünberg [7] in 1988, for which they won the Nobel prize in 2007. They discovered that when an electrical current passed through a layered magnetic system with different magnetic orientations, the resistance changed considerably depending on whether the magnetic layers were parallel or anti-parallel, as illustrated in Figure 5.1. The reason for this difference in resistance is that electrons with magnetic moments aligned with the local magnetization are scattered far more than electrons that have a magnetic moment anti-parallel with the local magnetization [103]. This can be argued through the fact that for the parallel magnetic moments there are many states they can scatter into, while for the anti-parallel magnetic moments there are far less, leading to a lower scattering of the anti-parallel magnetic moments.

   GMR has most noticeably been utilized in non-volatile memory technologies such as

(a)

(b)
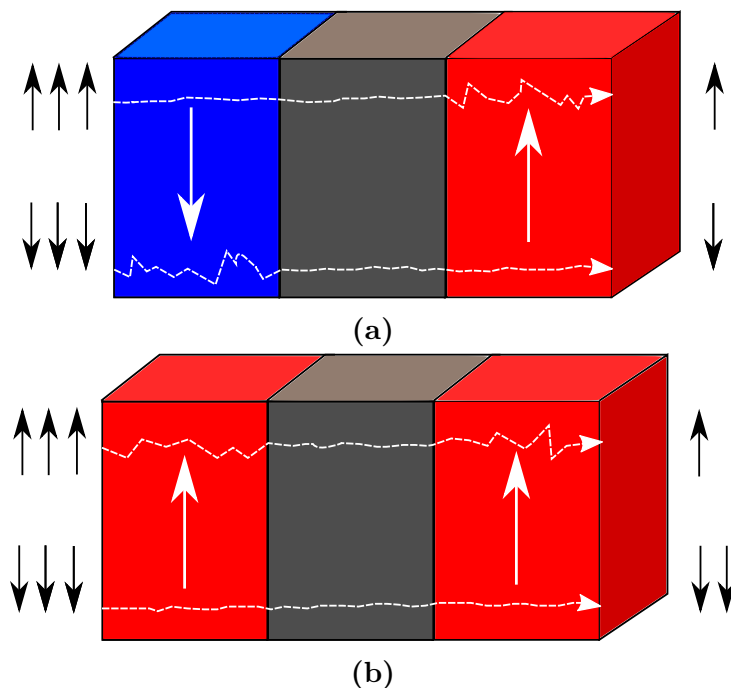
Figure 5.1. The resistance of a current passing through a multilayered magnetic system depends on the magnetic moment of the electron (proportional to their spin) and the alignment of the magnetic layers. Here we consider an anti-parallel configuration in **(a)** and a parallel configuration in **(b)** separated by a non-magnetic material. In **(a)** the resistance is high because of the anti-parallel configuration of the magnetic layers the current has to pass through, leading to considerable scattering of the parallel magnetic moments of the electrons due to the larger density of states. In **(b)** the resistance of the electrons with a magnetic moment anti-parallel to the magnetic layers is lower than the electrons with a parallel magnetic moment.

magnetoresistive random-access memory (MRAM) [2] and racetrack memories [4]. The GMR is pivotal in spin torque oscillators, as the resistance is a function of the angle between two magnetizations. If we were able to make these magnetizations oscillate, such that the angle between them varies in time, the oscillation in the resistance due to GMR will cause an oscillation in the current. We would then have an oscillator that converts the direct current applied to the system into an alternating current. This type of system that utilizes the precession of magnetic moments to generate an oscillating current is known as a spin torque oscillator (STO).

5.2   Spin torque oscillators under influence of spin–orbit coupling

The spin torque oscillators that we will consider in this thesis primarily consist of a fixed polarizing magnetic layer, and two free magnetic layers that interact with each other through the RKKY interaction. We will study the effects the Rashba spin–orbit coupling may have in two different geometries, a bulk geometry and a thin film geometry, as illustrated in Figure 5.2. Whether the system is in an oscillating state depends on the system parameters, such as the strength of the magnetic anisotropy (which we assume to be uniaxial), the current density inducing spin-transfer torques, and the strength of the RKKY interaction between the free magnetic layers. Spin torque oscillators have been

found to occur in both ferromagnetic [39] and antiferromagnetic [40] coupling between the free magnetic layers. By varying some of these parameters we can study when the system is in an STO phase, or when a collinear state where the free magnetic layers are aligned or anti-aligned with the easy axis of the material is stable. This would result in a phase diagram that would give information regarding what state we will find the system in for a given set of parameters. The goal of this chapter is to study the effects of Rashba spin–orbit coupling on the STO phase in this phase diagram, and the effects it has on the oscillation frequency of the current going out of the system.

(a)

(b)
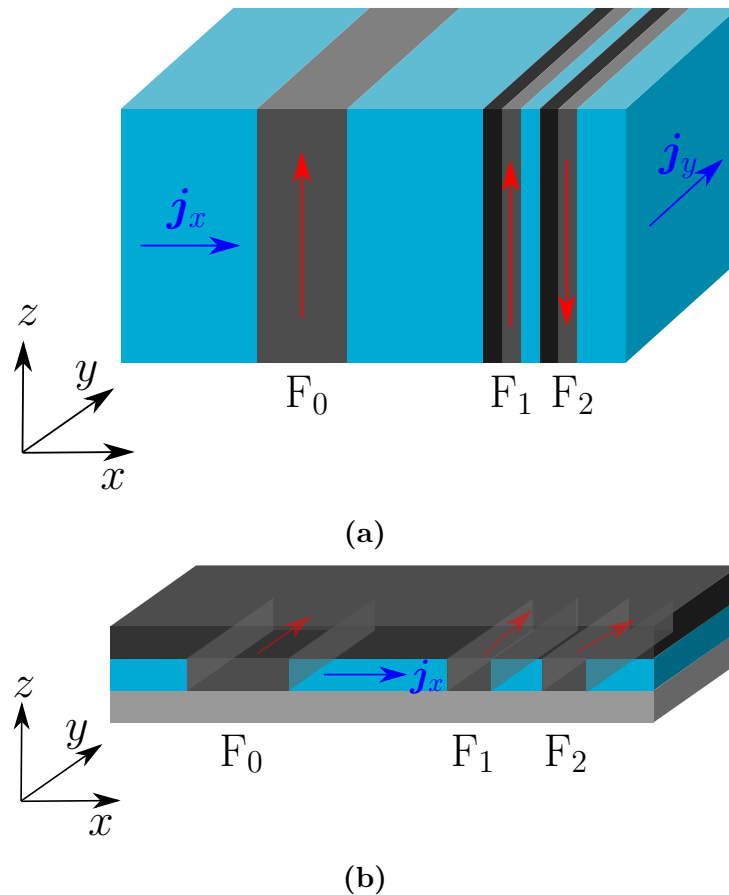
Figure 5.2. Illustrations of **(a)** the bulk geometry and **(b)** the thin film geometry. In the geometries a fixed magnetic layer F_0 is separated from two free magnetic layers F_1 and F_2 by a non-magnetic metallic material shown here in blue. A material illustrated in black, which is neighboring to F_1 and F_2 in **(a)** and the top film in **(b)**, is present to get a strong Rashba spin–orbit coupling at the interface of the free ferromagnetic layers. In **(b)** the bottom film is a material that will cause little to no RSOC at the interface to the ferromagnetic materials. To induce dynamics a current is applied in the x-direction which causes $\boldsymbol{m}_1$ and $\boldsymbol{m}_2$ to experience spin-transfer torques. In **(a)** a current is also applied in the y-direction to create significant RSOC effects on $\boldsymbol{m}_1$ and $\boldsymbol{m}_2$ due to the symmetry breaking in the x-direction. In the film geometry this is caused by the current in the x-direction as the symmetry breaking is in the z-direction. The free magnetic layers also interact through the RKKY interaction, while the distance to the fixed magnetic layer is chosen such that an RKKY interaction with this layer can be neglected. In **(a)** the material has an easy axis in the z-direction, while in **(b)** the material has an easy axis in the y-direction.

The model that we will use to analyze this system is a variation of the Landau–Lifshitz–Gilbert–Slonczewski (LLGS) equation that includes the Rashba field derived by Kim *et al.* [94]. The LLGS equation is an expansion of the LLG equation (2.22) that

includes spin-transfer torques on uniform magnetic moments. Usually the non-adiabatic spin-transfer torque is rather small compared to the adiabatic spin-transfer torque, to an order of magnitude on the size of the Gilbert damping α (which is typically 10^{-2} for the systems we will consider). This torque still has a significant contribution to the dynamics of the magnetization even at this order of magnitude, as we have previously seen in the skyrmion dynamics. In metallic multilayers such as N/F/N/F/N (N being a non-magnetic metal, and F being a ferromagnetic metal), however, the non-adiabatic STT is even smaller than usual due to symmetry considerations. The lowest contribution to the non-adiabatic STT in such a system becomes quadratic in the applied voltage bias V that generates the current responsible for STT. Since the voltage bias necessary to generate large current densities for systems at this scale is quite small, a torque that is proportional to V^2 can be neglected. This symmetry consideration is discussed in more detail by Ralph and Stiles [104]. We are then content by only including the adiabatic spin-transfer torque in our model, and the LLGS equation that we consider then becomes

$$\partial_t \boldsymbol{m}_i = -\gamma \boldsymbol{m}_i \times \left(\boldsymbol{H}_i^{\mathrm{eff}} + \boldsymbol{H}_i^{\mathrm{R}} - \beta \boldsymbol{m}_i \times \boldsymbol{H}_i^{\mathrm{R}} \right) + \alpha \boldsymbol{m}_i \times \partial_t \boldsymbol{m}_i + \boldsymbol{T}_i^{\mathrm{STT}}, \qquad (5.1)$$

with $\boldsymbol{m}_i$ being the magnetization in F_i. We remember that the Rashba field is given by

$$\boldsymbol{H}_i^{\mathrm{R}} = \frac{1}{1+\beta^2} \frac{\alpha_{\mathrm{R}} m_e P(i) j}{e M_s \hbar \mu_0} \hat{\boldsymbol{n}} \times \hat{\boldsymbol{j}}. \qquad (5.2)$$

The polarization $P(i)$ is the polarization of the current responsible for the spin–orbit coupling at the interface between F_i and the material that induces a strong RSOC at the interface. Note that the non-adiabatic contribution of the Rashba field proportional to β is still included, as the same symmetry argument that allowed us to neglect the non-adiabatic STT is not applicable to this torque. The adiabatic STT acting on $\boldsymbol{m}_1$ and $\boldsymbol{m}_2$ are given by

$$\boldsymbol{T}_1^{\mathrm{STT}} = -\frac{\gamma \hbar j_x}{2 e M_s \mu_0 d} \boldsymbol{m}_1 \times (P_0 \boldsymbol{m}_0 - P_1 \boldsymbol{m}_2) \times \boldsymbol{m}_1, \qquad (5.3\mathrm{a})$$

$$\boldsymbol{T}_2^{\mathrm{STT}} = -\frac{\gamma \hbar j_x}{2 e M_s \mu_0 d} P_1 \boldsymbol{m}_2 \times \boldsymbol{m}_1 \times \boldsymbol{m}_2, \qquad (5.3\mathrm{b})$$

following the derivation in Section 2.3.1. Here P_i is the polarization of the current in $\mathrm{F}_i/\mathrm{N}/\mathrm{F}_{i+1}$. The effective field $\boldsymbol{H}_i^{\mathrm{eff}}$ in the free magnetic layer F_i is given by the field resulting from magnetic anisotropy and the RKKY interaction, which becomes

$$\boldsymbol{H}_i^{\mathrm{eff}} = \frac{2K}{\mu_0 M_s} \left(\boldsymbol{m}_i \cdot \hat{\boldsymbol{n}}_k \right) \hat{\boldsymbol{n}}_k + \frac{J_{\mathrm{RKKY}}}{\mu_0 M_s d} \boldsymbol{m}_{\bar{i}}. \qquad (5.4)$$

Here $\hat{\boldsymbol{n}}_k$ is a unit vector along the easy axis, d is the thickness of the free magnetic layers F_1 and F_2 (which are assumed to have an equal thickness), and $\bar{i}$ indicates the index of the free magnetic layer that is not i ($\bar{i} = 3 - i$). To study the different stable phases of this system, which we assume to be collinear states along $\hat{\boldsymbol{n}}_k$, we follow the derivation by Zhou *et al.* [39]. We first make the ansatz that we have a small perturbation $\boldsymbol{u}_i$ from a collinear state, so that $\boldsymbol{m}_i \approx \lambda_i \hat{\boldsymbol{n}}_k + \boldsymbol{u}_i$, where $\lambda_i = \pm 1$. The possible collinear states in question are $\downarrow\downarrow, \downarrow\uparrow, \uparrow\downarrow, \uparrow\uparrow$, with the arrows indicating the direction of $\boldsymbol{m}_1$ and $\boldsymbol{m}_2$ respectively, and $\uparrow$ being the unit vector $\hat{\boldsymbol{n}}_k$ along the easy axis. To decide whether the collinear state is stable, we must study the time evolution of the perturbation $\boldsymbol{u}_i$. This

is done by performing a Fourier transform of the LLGS equation using our ansatz of $\boldsymbol{m}_i$, which is shown in Appendix B. The end result can be written compactly as

$$\left(\hat{A}\omega + \hat{V}\right) \begin{pmatrix} \tilde{\boldsymbol{u}}_1 \\ \tilde{\boldsymbol{u}}_2 \end{pmatrix} = 0. \tag{5.5}$$

The matrices for the different geometries are given by

$$\hat{A}_{\text{bulk}} = \begin{pmatrix} 1 - i\alpha\lambda_1 & 0 \\ 0 & 1 - i\alpha\lambda_2 \end{pmatrix}, \tag{5.6a}$$

$$\hat{A}_{\text{film}} = \begin{pmatrix} 1 + i\alpha\lambda_1 & 0 \\ 0 & 1 + i\alpha\lambda_2 \end{pmatrix}, \tag{5.6b}$$

$$\hat{V}_{\text{bulk}} = \omega_0 \begin{pmatrix} \lambda_1 & 0 \\ 0 & \lambda_2 \end{pmatrix} + \omega_J \begin{pmatrix} \lambda_2 & -\lambda_1 \\ -\lambda_2 & \lambda_1 \end{pmatrix} + i\omega_j^{(x)} \left[P_0 \begin{pmatrix} -\lambda_1 & 0 \\ 0 & 0 \end{pmatrix} + P_1 \begin{pmatrix} \lambda_1\lambda_2 & -1 \\ 1 & -\lambda_1\lambda_2 \end{pmatrix} \right]$$
$$\frac{\omega_{\text{R}}^{(y)}}{1+\beta^2} \left[\begin{pmatrix} P_1^{(y)} & 0 \\ 0 & P_2^{(y)} \end{pmatrix} - i\beta \begin{pmatrix} P_1^{(y)}\lambda_1 & 0 \\ 0 & P_2^{(y)}\lambda_2 \end{pmatrix} \right], \tag{5.6c}$$

$$\hat{V}_{\text{film}} = -\omega_0 \begin{pmatrix} \lambda_1 & 0 \\ 0 & \lambda_2 \end{pmatrix} - \omega_J \begin{pmatrix} \lambda_2 & -\lambda_1 \\ -\lambda_2 & \lambda_1 \end{pmatrix} + i\omega_j^{(x)} \left[P_0 \begin{pmatrix} -\lambda_1 & 0 \\ 0 & 0 \end{pmatrix} + P_1 \begin{pmatrix} \lambda_1\lambda_2 & -1 \\ 1 & -\lambda_1\lambda_2 \end{pmatrix} \right]$$
$$- \frac{\omega_{\text{R}}^{(x)}}{1+\beta^2} \left[\begin{pmatrix} P_0 & 0 \\ 0 & P_1 \end{pmatrix} + i\beta \begin{pmatrix} P_0\lambda_1 & 0 \\ 0 & P_1\lambda_2 \end{pmatrix} \right]. \tag{5.6d}$$

Here we have defined the frequencies $\omega_0 = 2\gamma K/\mu_0 M_s$, $\omega_J = \gamma J_{\text{RKKY}}/\mu_0 M_s d$, $\omega_j^{(x)} = \gamma\hbar j_x/2\mu_0 M_s d$ and $\omega_{\text{R}}^{(x/y)} = \gamma\alpha_{\text{R}} m_e j_{x/y}/\hbar\mu_0 e M_s$. $\tilde{\boldsymbol{u}}_1$ and $\tilde{\boldsymbol{u}}_2$ are the Fourier transforms of $\boldsymbol{u}_1$ and $\boldsymbol{u}_2$, and are defined as $\boldsymbol{u}_i(t) = \int \tilde{\boldsymbol{u}}_i(\omega) \exp\left(-i\omega t\right) d\omega/2\pi$. From this definition we can see that the perturbation is stable when the imaginary part of ω is less than zero, but when the imaginary part of ω is greater than zero the perturbation is exponentially increasing. To determine the sign of the imaginary component of ω we use (5.5). By rearranging the terms and multiplying with the inverse of $\hat{A}$, we see that ω is restricted to be one of the two possible eigenvalues of the 2×2 matrix $\hat{W} = -\hat{A}^{-1}\hat{V}$. The collinear state $\boldsymbol{m}_1 = \lambda_1\hat{\boldsymbol{n}}_k$, $\boldsymbol{m}_2 = \lambda_2\hat{\boldsymbol{n}}_k$ is then stable if both of the eigenvalues of $\hat{W}$ have negative imaginary components. This is of course dependent on the system parameters. We can then use this matrix to find the phase diagrams for when the collinear states are stable or not. There will be a region where none of the collinear states are stable for some choice of parameters, and it is in this region that an STO phase will have to be localized. However, a lack of a stable collinear state does not indicate that we have an STO phase. Our analytical model can only describe if a perturbation from a collinear state will increase or relax back to its original state, and if the perturbation is increasing it is not able to say whether the perturbation at some point becomes a self-sustained precession in the magnetization.

Something else that we need to consider is what defines an STO phase. The goal of the spin torque oscillator is to transform the applied direct current into an alternating current, utilizing the giant magnetoresistance effect. The resistance of our multilayer system is dependent on the respective alignment of the magnetic layers, so when we excite oscillations in the magnetizations we get an oscillating resistance of the system. The resistance is approximated by

$$R(t) = R_0 + \Delta R_1 \boldsymbol{m}_0 \cdot \boldsymbol{m}_1 + \Delta R_2 \boldsymbol{m}_1 \cdot \boldsymbol{m}_2. \tag{5.7}$$

To have a spin torque oscillator we must therefore require oscillations in at least $\boldsymbol{m}_0 \cdot \boldsymbol{m}_1$ or $\boldsymbol{m}_1 \cdot \boldsymbol{m}_2$. Oscillations in $\boldsymbol{m}_1$ in the form of a precession around the axis of $\boldsymbol{m}_0$ will therefore not cause any change in the resistance of the system, and such oscillations are hence not considered as an STO phase. We will therefore later establish numerically based on the time evolution of $\boldsymbol{m}_1$ and $\boldsymbol{m}_2$ when we have an STO phase in our system.

Before moving on to numerics, we want to see if it is possible to find an analogy for the new terms in the LLGS equation that the Rashba field introduces. We see that the matrix proportional to ω_R in (5.6c) and (5.6d) is very similar to the $\hat{A}$ matrix in (5.6a) and (5.6b) in the case when $P_0 = P_1$ and $P_1^{(y)} = P_2^{(y)}$. For simplicity we consider the case where all polarizations are equal to P, but is still valid in the case where $P_0 = P_1 = P$ and $P_1^{(y)} = P_2^{(y)} = P'$, as we can adjust the Rashba parameter so that $\alpha_R' P' = \alpha_R P$. If we consider this case, we can incorporate the effects of RSOC into (5.5) so that there is no explicit dependence on ω_R by introducing a new modified eigenfrequency ω^* and Gilbert damping α^*. These modified parameters would have to satisfy

$$\omega^* = \omega + \omega_R^{(x/y)} \frac{P}{1+\beta^2}, \tag{5.8a}$$

$$\omega^* \alpha^* = \omega \alpha + \omega_R^{(x/y)} \beta \frac{P}{1+\beta^2}. \tag{5.8b}$$

As we remember, we used the sign of the imaginary component of ω to determine whether a collinear state is stable or not. As $\omega_R^{(x/y)}$ is real, ω and ω^* have the same imaginary component, and the modified ω^* will therefore not have any impact on when a collinear state is stable or not. We therefore move on to consider the modified α^*. The modified Gilbert parameter is a complex function, while the original α is entirely real. However, as α^* only appears in the product $\omega^* \alpha^*$ in the Fourier transform of the LLGS equation, and ω^* and $\omega^* \alpha^*$ only have a modification in their real components, the imaginary component of α^* is there to weigh up for the change in the real component. The physical effects of RSOC on our system can then be seen from the real component of α^*, which is found to be

$$\Re(\alpha^*) = \frac{\left(\alpha \Re(\omega) + \beta \omega_R^{(x/y)} \frac{P}{1+\beta^2}\right)\left(\Re(\omega) + \omega_R^{(x/y)} \frac{P}{1+\beta^2}\right) + \alpha \Im(\omega)^2}{\left(\Re(\omega) + \omega_R^{(x/y)} \frac{P}{1+\beta^2}\right)^2 + \Im(\omega)^2}. \tag{5.9}$$

We note that there is no restriction on the sign on either ω or $\omega_R^{(x/y)}$, making it possible for α^* to take on a wide range of values. In the special case $\Im(\omega) = 0$ there is a singularity in $\Re(\alpha^*)$ at $\omega_R^{(x/y)} = (1+\beta^2)\Re(\omega)/P$, so that $\Re(\alpha^*)$ can in fact take on any value. It is then possible for us to get negative values of $\Re(\alpha^*)$, which differs from α which can only be positive. This enables us to get an anti-damping term in the LLGS equation, which will help destabilize the collinear states along the effective field. If we consider the case when $\Im(\omega) \neq 0$, $\Re(\alpha^*)$ is a finite and smooth function with a single minimum and maximum. These can be found by differentiating $\Re(\alpha^*)$ with respect to ω_R,

$$\frac{\partial}{\partial \omega_R} \Re(\alpha^*) = -(\alpha - \beta) \frac{\Im(\omega)^2\left(\Re(\omega) + 2\omega_R \frac{P}{1+\beta^2}\right) + \Re(\omega)\left(\Re(\omega) + \omega_R \frac{P}{1+\beta^2}\right)^2}{\left(\Im(\omega)^2 + \left(\Re(\omega) + \omega_R \frac{P}{1+\beta^2}\right)^2\right)^2} \tag{5.10}$$

and are found to be

$$\omega_R = -\left(\frac{1+\beta^2}{P}\right) \frac{\Im(\omega)^2 \pm \Im(\omega)\sqrt{\Im(\omega)^2 + \Re(\omega)^2} + \Re(\omega)^2}{\Re(\omega)}. \tag{5.11}$$

We see that the sign of the derivative is dependent on whether $\alpha > \beta$ or $\alpha < \beta$, in addition to the sign of $\Re\mathrm{e}(\omega)$ and ω_{R}. If we are in a maximal region of $\Re\mathrm{e}(\alpha^*)$ (a region where $\Re\mathrm{e}(\alpha^*) > \alpha$), we can therefore move to a minimal region ($\Re\mathrm{e}(\alpha^*) < \alpha$) by switching the sign of ω_{R}, which we can control by the direction of the current responsible for RSOC. This is easily done in the bulk geometry, as we can switch the direction of the current in the y-direction which only affects the spin–orbit coupling. In the thin-film geometry switching the sign of j_x may not have the desired effects, as this current is also responsible for the spin-transfer torques, and a change in j_x will therefore also lead to a change in ω.

The minimum value of $\Re\mathrm{e}(\alpha^*)$ can still be negative even when $\Im\mathrm{m}(\omega) \neq 0$, despite the lack of a singularity. Whether we can get a negative value depends heavily on ω, however, which is a complex function not only of the system parameters, but also of the collinear state. So even if RSOC helps to destabilize one collinear state by turning the Gilbert damping into an anti-damping term, it is not given that this will occur for all collinear states.

5.3   Numerical simulations

5.3.1   Method

For our numerical solution we need to solve the LLGS equation (5.1) directly. This is a three dimensional vector equation, but due to the interaction between $\boldsymbol{m}_1$ and $\boldsymbol{m}_2$ through the RKKY-interaction and the spin-transfer torques, we need to solve for both vectors simultaneously. This makes the LLGS equation for this case six coupled differential equations that are highly non-linear, due to the cubic terms appearing in the STT. The advantage with this equation over the LLG equation that we got for the skyrmion case, however, is that the solution is only temporally varying, making this an ordinary differential equation (ODE) instead of the partial differential equation (PDE) we got for the skyrmion. ODEs are in general much easier to solve than PDEs, and software such as `MATLAB` has well-implemented solvers for such problems. We will here utilize `MATLAB`'s `ode45` solver. One problem that was encountered when solving the LLGS equation numerically was one that is familiar to us from the skyrmion case; the modulus of the magnetization unit vector was not always conserved to unity. For some parameters the modulus even oscillated between being one and zero, which clearly is a type of behavior we want to eliminate. For the skyrmion case we narrowed the problem down to either being a singularity in the spatial derivatives or the fact that conservation of the unit modulus was not explicitly enforced in the solution (only through the form of the LLG equation, which should conserve the modulus). In the LLGS equation we have no spatial derivatives, but like the skyrmion case we also have not explicitly enforced the unity modulus in the solution. One way to implement this is to replace quadratic factors in a single magnetization component m_i^2 by $1 - m_j^2 - m_k^2$ to enforce the unity relation

$$m_x^2 + m_y^2 + m_z^2 = 1. \tag{5.12}$$

For the solution of the skyrmion motion this method was not feasible, as we had no quadratic factors in any single magnetization component, and the method does not work well for linear factors as we get an ambiguity in the sign when taking the square root of the relation above. For the LLGS equation in the STO case this method is feasible due to the different type of STT terms. This method is not perfect, we still get a magnetization modulus that decreases with time, but the magnitude of this decrease is negligible.
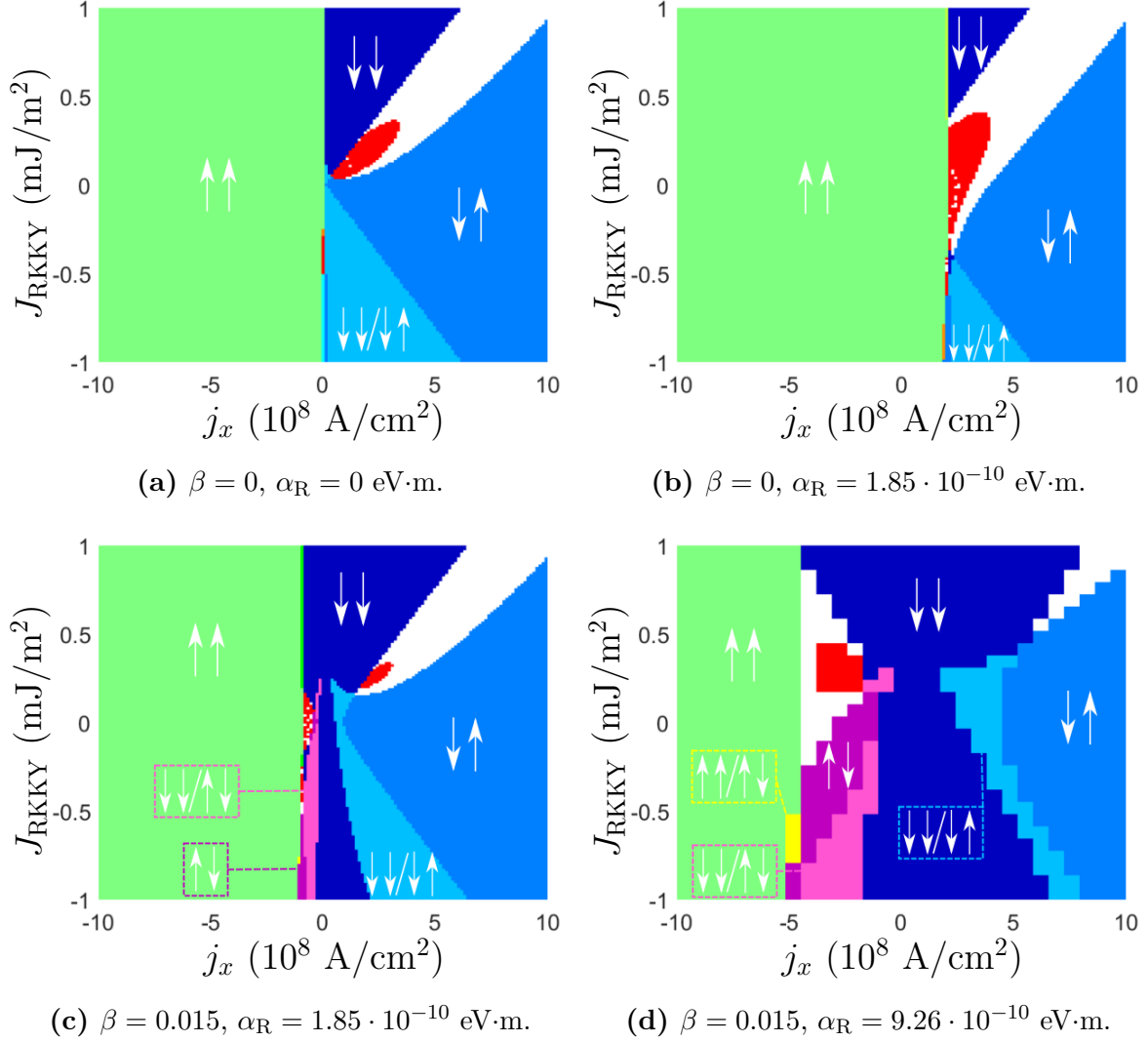
Once the LLGS equation is solved for all six vector components, we need to analyze the results. This analysis will primarily decide if the solution is in a collinear state, an STO phase, or none of the former. We will also perform a Fourier transform of $\boldsymbol{m}_0 \cdot \boldsymbol{m}_1$ for some sets of parameters to see the frequency spectrum of a potential STO phase. To establish if the solution is a collinear state or an STO phase we consider the last 20% of the time-interval of the calculated solution, and then compare the latter half of that to the former half. In each half of the interval we first calculate the average value of $\boldsymbol{m}_0 \cdot \boldsymbol{m}_1$ and $\boldsymbol{m}_1 \cdot \boldsymbol{m}_2$, and how much the solution varies from that average during the interval. If the variation in the latter interval is above some cutoff factor between zero and one times the variation in the former interval, and the average variation is above some minimal value, we classify the solution as an STO phase. This way an oscillation that decays significantly and very small oscillations will not be classified as an STO phase. In our calculations we set the cutoff-factor to 0.9, and the minimum variance necessary to have an STO phase to be 10^{-6} per time unit in the latter 10% of the solution interval. If the conclusion is that the solution is not an STO phase, we classify the state based on the final value of the solution of the vector components. If the final value of the two vector components along the easy axis is ± 1 to some degree of accuracy and the remaining four are zero, we classify the solution to be in the corresponding collinear state. If that is also not the case, we classify the system as being in a canted state. A canted state is where the magnetization has either relaxed to a state that is not parallel to the easy axis, or the system is oscillating in a manner that keeps $\boldsymbol{m}_0 \cdot \boldsymbol{m}_1$ and $\boldsymbol{m}_1 \cdot \boldsymbol{m}_2$ constant (and thereby not generating oscillations in the resistance).

Regarding the dimensional treatment of the numerical implementation, the LLGS equation can be written in terms of the frequency constants ω_0, ω_J, $\omega_j^{(x)}$, $\omega_R^{(x/y)}$, some dimensionless constants and the magnetization unit vectors. We set the value of ω_0 to be unity in our simulations, which defines our unit time step, and scale our remaining frequencies accordingly.

5.3.2 Phase diagrams

By combining the analytical framework and numerical method described previously, we can create phase diagrams that show for what parameters the different collinear states are stable, when we have an STO phase, and when we are in a canted state. We perform these calculations with the same parameters as Zhou *et al.* [39] for an easy comparison between the results with and without RSOC. These parameters are $\alpha = 0.01$, $P = 0.5$, $K = 8 \cdot 10^4$ J/m^3, $d = 3$ nm, $J \sim 1$ mJ/m^2, $j_x \sim 10^8$ A/cm^2, $M_s = 127$ kA/m. In the bulk geometry we also set $j_y = 10^9$ A/cm^2. Regarding the strength of the Rashba parameter α_R we consider the values $\alpha_R = 0$, $1.85 \cdot 10^{-10}$ eV·m, $9.26 \cdot 10^{-10}$ eV·m. These rather high values are chosen to get a clear indication of the effects RSOC may have. The values are also chosen not to be unrealistic, as α_R has been found to be $\sim 3.7 \cdot 10^{-10}$ eV·m at the surface of Bi/Ag alloy [43]. In the bulk geometry the strength of the Rashba parameter is not too important, as we can adjust for a lower α_R by increasing j_y accordingly. This is not possible in the thin film geometry, however, as both spin-transfer torques and RSOC are controlled by the current j_x, and so the strength of α_R becomes more important in the thin film geometry.

Performing the calculations, the resulting phase diagrams for the bulk geometry are shown in Figure 5.3, and the phase diagrams for the thin film geometry are shown in Figure 5.4. The phase diagram without the effects of RSOC, as found by Zhou et al.,

(a) $\beta = 0$, $\alpha_\mathrm{R} = 0$ eV·m.

(b) $\beta = 0$, $\alpha_\mathrm{R} = 1.85 \cdot 10^{-10}$ eV·m.

(c) $\beta = 0.015$, $\alpha_\mathrm{R} = 1.85 \cdot 10^{-10}$ eV·m.

(d) $\beta = 0.015$, $\alpha_\mathrm{R} = 9.26 \cdot 10^{-10}$ eV·m.

Figure 5.3. Phase diagrams for the bulk geometry. For all phase diagrams the values $\alpha = 0.01$, $P = 0.5$, $j_y = 10^9$ A/cm^2, $K = 8 \cdot 10^4$ J/m^3, $d = 3$ nm are assumed. The red regions indicate an STO phase, while the white regions are canted states.

is presented in Figure 5.3a. We see by comparing it to a system with RSOC present, as shown in Figure 5.3b, that RSOC can increase the size of the STO phase and even extend it down to the antiferromagnetic regime for compensated magnetic moments $\boldsymbol{m}_i$. Now to compare our results to our analogy of RSOC effectively modifying the Gilbert damping α. According to Zhou *et al.* the border between the unstable region (STO phase and the canted state, illustrated in red and white) and the ↑↓ state is approximately given by

$$\omega_J = \sqrt{4\omega_0^2 + \left(\omega_j^{(x)}\right)^2} - 2\omega_0 + \alpha \frac{\omega_0^2}{\omega_j^{(x)}}. \tag{5.13}$$

For $\alpha > 0$ we would therefore expect the border to increase as $j_x \to 0^+$, as in Figure 5.3a. In Figure 5.3b, however, this border decreases as $j_x \to 0^+$ as if $\alpha < 0$. As we remember from our analogy, we found that the effective Gilbert damping $\Re\mathrm{e}(\alpha^*)$ could become negative in the presence of RSOC for some set of parameters. This seems to be the case here. We also remember that we could switch from being in a minimal region in $\Re\mathrm{e}(\alpha^*)$ to a maximal region by letting $\beta > \alpha$ if we were in a minimal region when

$\beta < \alpha$. The phase diagram in this case is shown in Figure 5.3c. As predicted, the border between the unstable region and the ↑↓ state is lifted. In addition, the size of the STO phase localized in that region decreases, which would correspond well with an increase in the Gilbert damping. This does not mean systems with $\beta > \alpha$ are of no interest to get an increase in the size of the STO phase, however. We also noted in our analogy that we could also go from being in a minimal to a maximal region in $\Re(\alpha^*)$ by switching the direction of the current in the y-direction.

(a) $\beta = 0$, $\alpha_{\mathrm{R}} = 9.26 \cdot 10^{-10}$ eV·m.   **(b)** $\beta = 0.005$, $\alpha_{\mathrm{R}} = 9.26 \cdot 10^{-10}$ eV·m.
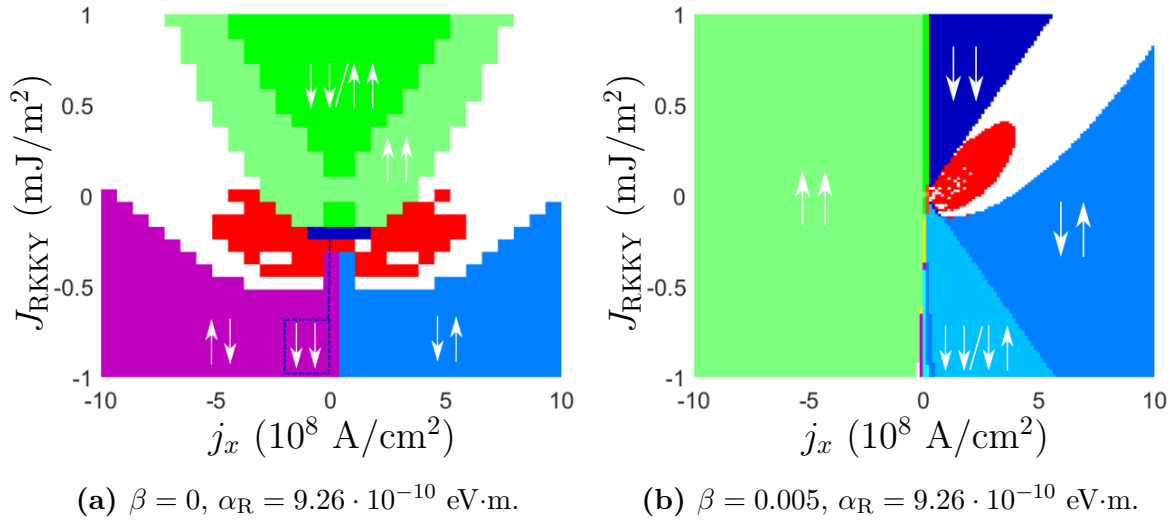
Figure 5.4. Phase diagrams for the thin film geometry. For all phase diagrams the values $\alpha = 0.01$, $P = 0.5$, $K = 8 \cdot 10^4$ J/m^3, $d = 3$ nm are assumed. The red regions indicate an STO phase, while the white regions are canted states.

(a)   **(b)**
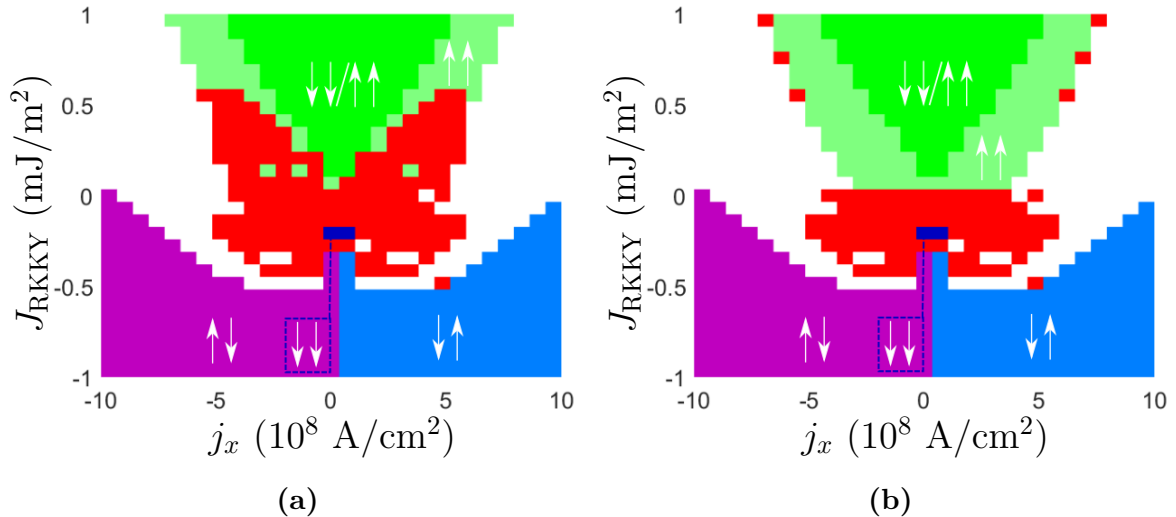
Figure 5.5. The stability of the ↑↑ state in the thin film geometry for $\beta = 0$, $\alpha_{\mathrm{R}} = 9.26 \cdot 10^{-10}$ eV·m is found to be very dependent on the initial conditions. In **(a)** the initial state is chosen to be close to ↓↓ for $J_{\mathrm{RKKY}} > 0$, while in **(b)** the initial state is chosen to be close to ↑↑ in the same region. In both cases the initial state is chosen to be close to ↓↑ for $J_{\mathrm{RKKY}} < 0$.
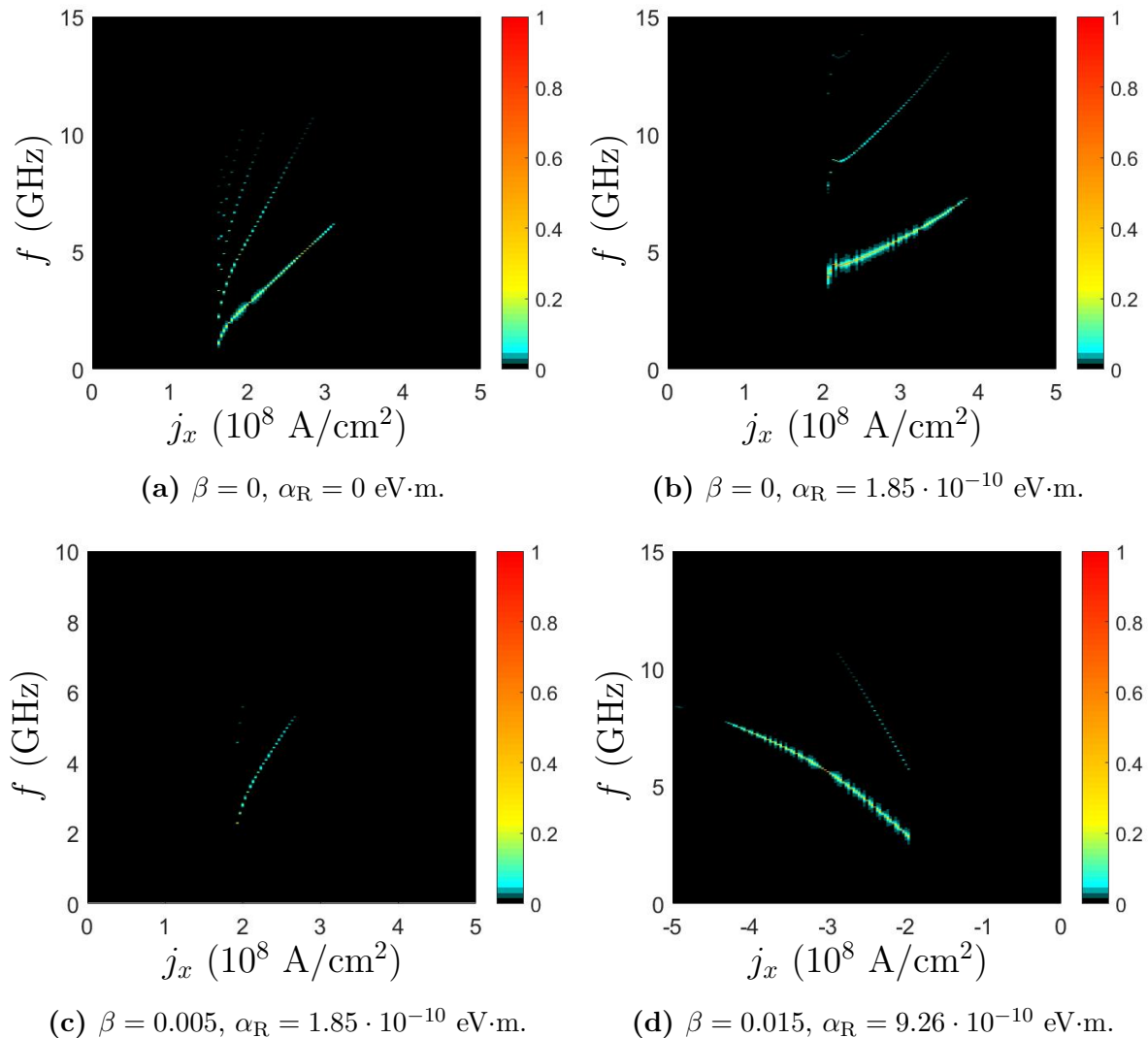
Moving on to the thin film geometry, we get a different behavior in the phase diagrams. We do not get the same behavior in the border between the unstable region

and the ↑↓ state due to the fact that the effects of RSOC are proportional to j_x, and as $j_x \to 0$ these effects vanish. We can, however, still see a lowering of the border with RSOC present, as shown in both Figure 5.4a and 5.4b, but we do not have the same effect when $j_x \to 0^+$. In the phase diagrams shown here we also have an increase in the STO phase for the thin film geometry when RSOC is present, though this increase requires a rather large Rashba parameter α_R to become evident. We are also able to find an STO phase in the antiferromagnetic regime ($J_{RKKY} < 0$), most noticeably in the case with $\beta = 0$, $\alpha_R = 9.26 \cdot 10^{-10}$ eV·m as illustrated in Figure 5.4a. This STO phase is also more or less symmetric in j_x. Something that should be noted with this set of parameters is that while we have a region where the ↑↑ state is stable, numerical calculations show that whether the system relaxes to this state is highly dependent on the initial condition of $\boldsymbol{m}_1$ and $\boldsymbol{m}_2$. In Figure 5.5 we show all the points in the phase diagram that are found to be in an oscillating state for different initial conditions. This is in contrast with Figure 5.3 and 5.4 where we only classify a point to be an oscillating state if the numerical calculations indicate this and the analytical calculations say there are no stable collinear states the system can relax to. In all figures the stability of the collinear states is determined analytically, while the STO phase is found numerically. As we can see in Figure 5.5a an initial condition that is close to ↓↓ or ↓↑ does not relax to the ↑↑ state even if this is stable, and we can also get an STO phase in the ferromagnetic regime. This can be understood by looking at the imaginary component of ω belonging to the ↑↑ state for these parameters. It is found that the imaginary component, while less than zero, only has a magnitude of 10^{-2}. In comparison the other stable regions typically have an order of magnitude up to 10^1. It is therefore not surprising that if the initial state is far away from being in ↑↑ it is possible that the system will not relax to that state, and we can get an oscillating or canted state even though there exists a stable collinear state.

The sensitivity issue concerning the initial state of $\boldsymbol{m}_1$ and $\boldsymbol{m}_2$ was only of considerable significance for the ↑↑ state in the thin-film geometry with $\beta = 0$, $\alpha_R = 9.26 \cdot 10^{-10}$ eV·m. There was also some sensitivity for other phase diagrams in the limit $j_x \to 0$. Regarding the cutoff factors utilized for classifying the numerical solution, there was very little sensitivity in the choice of parameters. The transitional region between an STO state and a canted or collinear state is found to happen on a typical scale of 10^6 A/cm^2 or 10^{-3} mJ/m^2, both of which being very small compared to the magnitude of the parameters considered. As the cutoff factors would primarily have an effect in this transitional region, a change in these parameters would not lead to a significant change in the size of the STO phase. It can also be seen in some of the phase diagrams that there are found to be some canted states in the middle of the STO region, or a single STO state separated from the main STO region. This is discovered to be due to the time interval the system is solved over, as for some parameters it takes longer time for the system to obtain stable oscillations than for others. The time scale that the system was solved over was constrained to some degree, due to the run-time of the solver. It is also observed that the initial state of $\boldsymbol{m}_1$ and $\boldsymbol{m}_2$ has some impact on how fast these oscillations become stable. When solving the system over a longer time scale the STO regions should become more or less continuous.

5.3.3 Frequency spectra

We have now shown that with the presence of RSOC we are able to increase the size of the STO phase. It is also of interest to study what impact RSOC has on the frequency

(a) $\beta = 0$, $\alpha_\mathrm{R} = 0$ eV·m.

(b) $\beta = 0$, $\alpha_\mathrm{R} = 1.85 \cdot 10^{-10}$ eV·m.

(c) $\beta = 0.005$, $\alpha_\mathrm{R} = 1.85 \cdot 10^{-10}$ eV·m.

(d) $\beta = 0.015$, $\alpha_\mathrm{R} = 9.26 \cdot 10^{-10}$ eV·m.

Figure 5.6. The one sided spectra of the Fourier transform of $\boldsymbol{m}_0 \cdot \boldsymbol{m}_1$ in the bulk geometry. The Fourier transform was taken along the $J_\mathrm{RKKY} = 0.25$ mJ/m^2 line in the phase diagrams.

spectrum. To study this we take fast Fourier transforms of $\boldsymbol{m}_0 \cdot \boldsymbol{m}_1$ for selected values of J_RKKY. The Fourier transforms of $\boldsymbol{m}_1 \cdot \boldsymbol{m}_2$ are not presented as they show the same frequency spectra, but with slightly different amplitudes. The results for the bulk geometry are shown in Figure 5.6, and the results for the thin film geometry are shown in Figure 5.7. First considering the results from the bulk geometry, we see that in the presence of RSOC we have fewer frequencies for a given j_x in comparison to the case without RSOC. Moreover, we see that the amplitude of the oscillations can also be larger when we have RSOC in the system, as seen in Figure 5.6b and 5.6d. For some parameters they can also be smaller, however, as seen in Figure 5.6c. The main frequency in the presence of RSOC tends to be more slowly varying as a function of j_x than the system without RSOC, but we can obtain slightly higher frequencies with RSOC than without. In addition, the oscillations in the presence of RSOC can also have higher amplitudes than the system without RSOC, as shown in Figure 5.6b and 5.6d. As the strength of RSOC is controllable by j_y, this allows for a more tunable frequency spectrum in the spin torque oscillator when the effects of RSOC are included. We now have two parameters we can vary to control the frequency output without changing the materialistic properties instead of just one.

Considering the frequency spectra in the thin film geometry we see that for the ferromagnetically coupled magnetic moments in Figure 5.7b the behavior is rather similar to the bulk geometry case in Figure 5.6b. We have higher amplitudes of the oscillations, and a reduction in the amount of frequencies. The frequency as a function of current is slightly steeper than in the bulk geometry, however. The result that makes the thin film geometry stand out from the bulk geometry is the frequency spectrum of the antiferromagnetically coupled magnetic moments in Figure 5.7a. As we can see, the frequency spectrum reflects the same symmetry in j_x as the STO phase in the phase diagram. In addition, we have several more frequencies available in this antiferromagnetic STO than in the ferromagnetic STO.

(a) $\beta = 0$, $\alpha_R = 9.26 \cdot 10^{-10}$ eV·m.   **(b)** $\beta = 0.005$, $\alpha_R = 9.26 \cdot 10^{-10}$ eV·m.
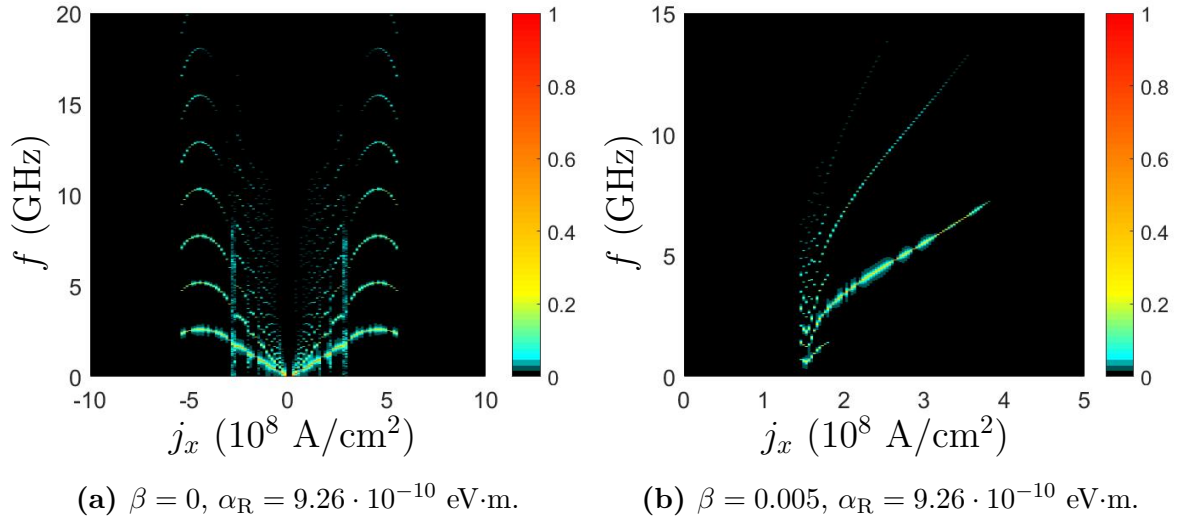
Figure 5.7. The one sided spectra of the Fourier transform of $\boldsymbol{m}_0 \cdot \boldsymbol{m}_1$ in the thin film geometry. The Fourier transform was taken along the $J_{\mathrm{RKKY}} = -0.2$ mJ/m^2 line in **(a)** and along $J_{\mathrm{RKKY}} = 0.25$ mJ/m^2 in **(b)**.

6

Conclusion

6.1 Summary and conclusion

We have derived analytically the velocity of a skyrmion under the effects of a spin-transfer torque from a spin polarized current, Rashba spin–orbit coupling, a constant electric field gradient and a phenomenological pinning force. It was found that the effects of the spin–orbit coupling could be viewed as a modification of the non-adiabatic spin-transfer torque. The motion of the skyrmion due to a constant electric field gradient could be described as a motion along the equipotential lines perpendicular to the gradient, and a damped motion proportional to the Gilbert damping in the opposite direction of the gradient. The electric field gradient is not able to generate high skyrmion velocities, but can be used to cancel out the perpendicular velocity component due to the topological Hall effect in the motion driven by a spin-polarized current. In the presence of pinning forces it was found that the critical current was smaller for smaller skyrmions when Rashba spin–orbit coupling was present, but the reduction was only significant for large values of the non-adiabatic spin-transfer torque. Without the presence of Rashba spin–orbit coupling the situation is reversed, and larger skyrmions have a smaller critical current. For the motion driven by electric field gradients larger skyrmions had a lower critical field gradient.

The analytical derivation was based on the micromagnetic model and the Thiele equation. The Thiele equation is a simplification of the Landau–Lifshitz–Gilbert equation, and assumes a rigid motion of the skyrmion. To check if the ansatz of a rigid motion holds true the LLG equation was also solved numerically for comparison to the results from the Thiele equation, as the LLG equation makes no assumptions regarding the shape of the skyrmion during its motion. Due to the complexity of the LLG equation, however, stability problems were encountered when utilizing a standard finite element method solver. After a certain time step the numerical simulations did not longer conserve the magnitude of the magnetization, which is explicitly conserved by the form of the LLG equation. To attempt to get any useful results before this instability rendered any result useless, very strong currents and electric field gradients were considered to be able to observe the dynamics of the skyrmion at that time-scale. The results observed agreed qualitatively with the analytical results derived, but some deformation of the skyrmion was also observed. This

could potentially be due to the extreme values used in the numerical simulations. To be able to draw any real conclusions from the numerical data it is therefore recommended to run new simulations with a solver more specialized for the LLG equation, so that it is possible to observe the skyrmion dynamics over longer time steps with more realistic parameters for the current and electric field gradient.

In addition to the electric control of the skyrmion dynamics, we also studied the electrical control of spin torque oscillators in systems with Rashba spin–orbit coupling in the free magnetic layers. The strength of this spin–orbit coupling was tunable by a spin polarized electric current, allowing us to control the magnitude of the resulting effects in our system. The phase diagrams for two different geometries were calculated analytically and numerically for varying strengths of the spin–orbit coupling. It was discovered that by having Rashba spin–orbit coupling in our system we could increase the size of the resulting spin torque oscillator phase in our phase diagrams, and that it was possible to get an oscillating phase in both ferromagnetically and antiferromagnetically coupled compensated magnetic layers, the latter of which being a new discovery. Moreover, the oscillations in the spin torque oscillator phase were often found to have higher amplitudes in their oscillations when spin–orbit coupling was present, and the frequencies obtained often differed slightly from the system without spin–orbit coupling. This is of particular interest as it allows for a wider tunability of the frequency output by varying the strength of the current applied to the system.

6.2 Prospects for further studies

In this thesis the focus has been on electrical control of magnetization dynamics. We have shown how the direction of the skyrmion motion can be adjusted by a constant electric field gradient, and previously it has also been shown how skyrmions can be guided by generating unstable regions with electric fields [27]. What can also be of interest to study is how the motion of skyrmions are affected by more complex spatial variations in the electric field. If it was possible to create an energy landscape that allowed us to generate a trajectory for individual skyrmions this would be highly attractive in skyrmion-based memory applications.

The motion of skyrmions can also be manipulated by other means than electric currents and fields. In recent years it has been shown that skyrmion motion can be driven by magnons, both in a translational [105] and rotational [106] manner. The motion is induced by the scattering of the magnons in the skyrmion. The translational motion can be generated by a spin-wave source, whereas the rotational motion has been found to occur due to thermal magnons. How the skyrmion magnon-driven motion can be controlled in a manner viable for use in memory application is still a topic of interest.

The magnon-driven magnetization dynamics has also been shown to be able to drive spin torque oscillators in ferromagnetic multilayers [107], but has yet to be studied for an antiferromagnetic coupling.

7
Bibliography

[1] N. Okamoto, H. Kurebayashi, T. Trypiniotis, I. Farrer, D. A. Ritchie, E. Saitoh, J. Sinova, J. Mašek, T. Jungwirth, and C. H. W. Barnes. Electric control of the spin hall effect by intervalley transitions. *Nat Mater*, 13(10):932–937, Oct 2014. Article.

[2] J. Åkerman. Toward a universal memory. *Science*, 308(5721):508–510, 2005.

[3] J.A. Katine and Eric E. Fullerton. Device implications of spin-transfer torques. *Journal of Magnetism and Magnetic Materials*, 320(7):1217 – 1226, 2008.

[4] S. S. P. Parkin, M. Hayashi, and L. Thomas. Magnetic domain-wall racetrack memory. *Science*, 320(5873):190–194, 2008.

[5] A. D. Kent and D. C. Worledge. A new spin on magnetic memories. *Nat Nano*, 10(3):187–191, Mar 2015. Commentary.

[6] M. N. Baibich, J. M. Broto, A. Fert, F. Nguyen Van Dau, F. Petroff, P. Etienne, G. Creuzet, A. Friederich, and J. Chazelas. Giant magnetoresistance of (001)Fe/(001)Cr magnetic superlattices. *Phys. Rev. Lett.*, 61:2472–2475, Nov 1988.

[7] G. Binasch, P. Grünberg, F. Saurenbach, and W. Zinn. Enhanced magnetoresistance in layered magnetic structures with antiferromagnetic interlayer exchange. *Phys. Rev. B*, 39:4828–4830, Mar 1989.

[8] M. Johnson and R. H. Silsbee. Interfacial charge-spin coupling: Injection and detection of spin magnetization in metals. *Phys. Rev. Lett.*, 55:1790–1793, Oct 1985.

[9] L. Berger. Lowfield magnetoresistance and domain drag in ferromagnets. *Journal of Applied Physics*, 49(3):2156–2161, 1978.

[10] L. Berger. Exchange interaction between ferromagnetic domain wall and electric current in very thin metallic films. *Journal of Applied Physics*, 55(6):1954–1956, 1984.

[11] L. Berger. Motion of a magnetic domain wall traversed by fastrising current pulses. *Journal of Applied Physics*, 71(6):2721–2726, 1992.

[12] L. Berger. Emission of spin waves by a magnetic multilayer traversed by a current. *Phys. Rev. B*, 54:9353–9358, Oct 1996.

[13] J.C. Slonczewski. Current-driven excitation of magnetic multilayers. *Journal of Magnetism and Magnetic Materials*, 159(1–2):L1 – L7, 1996.

[14] M. Tsoi, A. G. M. Jansen, J. Bass, W.-C. Chiang, M. Seck, V. Tsoi, and P. Wyder. Excitation of a magnetic multilayer by an electric current. *Phys. Rev. Lett.*, 80:4281–4284, May 1998.

[15] E. B. Myers, D. C. Ralph, J. A. Katine, R. N. Louie, and R. A. Buhrman. Current-induced switching of domains in magnetic multilayer devices. *Science*, 285(5429):867–870, 1999.

[16] J.Z Sun. Current-driven magnetic switching in manganite trilayer junctions. *Journal of Magnetism and Magnetic Materials*, 202(1):157 – 162, 1999.

[17] J. A. Katine, F. J. Albert, R. A. Buhrman, E. B. Myers, and D. C. Ralph. Current-driven magnetization reversal and spin-wave excitations in Co /Cu /Co pillars. *Phys. Rev. Lett.*, 84:3149–3152, Apr 2000.

[18] L. Gan, S. H. Chung, K. H. Aschenbach, M. Dreyer, and R. D. Gomez. Pulsed-current-induced domain wall propagation in permalloy patterns observed using magnetic force microscope. *IEEE Transactions on Magnetics*, 36(5):3047–3049, Sep 2000.

[19] N. Vernier, D. A. Allwood, D. Atkinson, M. D. Cooke, and R. P. Cowburn. Domain wall propagation in magnetic nanowires by spin-polarized current injection. *EPL (Europhysics Letters)*, 65(4):526, 2004.

[20] N.L. Schryer and L. R. Walker. The motion of 180° domain walls in uniform dc magnetic fields . *Journal of Applied Physics*, 45(5406), 1974.

[21] A. Yamaguchi, S. Nasu, H. Tanigawa, T. Ono, K. Miyake, K. Mibu, and T. Shinjo. Effect of joule heating in current-driven domain wall motion. *Applied Physics Letters*, 86(1), 2005.

[22] F. Jonietz, S. Mühlbauer, C. Pfleiderer, A. Neubauer, W. Münzer, A. Bauer, T. Adams, R. Georgii, P. Böni, R. A. Duine, K. Everschor, M. Garst, and A. Rosch. Spin transfer torques in mnsi at ultralow current densities. *Science*, 330(6011):1648–1651, 2010.

[23] T. Schulz, R. Ritz, A. Bauer, M. Halder, M. Wagner, C. Franz, C. Pfleiderer, K. Everschor, M. Garst, and A. Rosch. Emergent electrodynamics of skyrmions in a chiral magnet. *Nat Phys*, 8(4):301–304, Apr 2012.

[24] X. Z. Yu, N. Kanazawa, W. Z. Zhang, T. Nagai, T. Hara, K. Kimoto, Y. Matsui, Y. Onose, and Y. Tokura. Skyrmion flow near room temperature in an ultralow current density. *Nat Commun*, 3:988, Aug 2012.

[25] J. Grollier, P. Boulenc, V. Cros, A. Hamzić, A. Vaurès, A. Fert, and G. Faini. Switching a spin valve back and forth by current-induced domain wall motion. *Applied Physics Letters*, 83(3), 2003.

[26] M. Mochizuki and Y. Watanabe. Writing a skyrmion on multiferroic materials. *Applied Physics Letters*, 107(8), 2015.

[27] P. Upadhyaya, G. Yu, P. K. Amiri, and K. L. Wang. Electric-field guiding of magnetic skyrmions. *Phys. Rev. B*, 92:134411, Oct 2015.

[28] A. Fert, V. Cros, and J. Sampaio. Skyrmions on the track. *Nat Nano*, 8(3):152–156, Mar 2013.

[29] J. Sampaio, V. Cros, S. Rohart, A. Thiaville, and A. Fert. Nucleation, stability and current-induced motion of isolated magnetic skyrmions in nanostructures. *Nat Nano*, 8(11):839–844, Nov 2013. Article.

[30] Y. Liu, G. Yin, J. Zang, J. Shi, and R. K. Lake. Skyrmion creation and annihilation by spin waves. *Applied Physics Letters*, 107(15), 2015.

[31] Y. Nii, T. Nakajima, A. Kikkawa, Y. Yamasaki, K. Ohishi, J. Suzuki, Y. Taguchi, T. Arima, Y. Tokura, and Y. Iwasa. Uniaxial stress control of skyrmion phase. *Nat Commun*, 6, Oct 2015. Article.

[32] S-H. Yang, K-S. Ryu, and S. Parkin. Domain-wall velocities of up to $750 \, \mathrm{ms}^{-1}$ driven by exchange-coupling torque in synthetic antiferromagnets. *Nature Nanotechnology*, 10(3):221–226, Mar 2015. Letter.

[33] M. Tsoi, A. G. M. Jansen, J. Bass, W.-C. Chiang, V. Tsoi, and P. Wyder. Generation and detection of phase-coherent current-driven magnons in magnetic multilayers. *Nature*, 406(6791):46–48, Jul 2000.

[34] S. I. Kiselev, J. C. Sankey, I. N. Krivorotov, N. C. Emley, R. J. Schoelkopf, R. A. Buhrman, and D. C. Ralph. Microwave oscillations of a nanomagnet driven by a spin-polarized current. *Nature*, 425(6956):380–383, Sep 2003.

[35] W. H. Rippard, M. R. Pufall, S. Kaka, S. E. Russek, and T. J. Silva. Direct-current induced dynamics in $Co_{90}Fe_{10}/Ni_{80}Fe_{20}$ point contacts. *Phys. Rev. Lett.*, 92:027201, Jan 2004.

[36] T.J. Silva and W.H. Rippard. Developments in nano-oscillators based upon spin-transfer point-contact devices. *Journal of Magnetism and Magnetic Materials*, 320(7):1260 – 1271, 2008.

[37] J-V. Kim. Chapter four - Spin-torque oscillators. volume 63 of *Solid State Physics*, pages 217 – 294. Academic Press, 2012.

[38] J.Z. Sun and D.C. Ralph. Magnetoresistance and spin-transfer torque in magnetic tunnel junctions. *Journal of Magnetism and Magnetic Materials*, 320(7):1227 – 1237, 2008.

[39] Y. Zhou, J. Xiao, G. E. W. Bauer, and F. C. Zhang. Field-free synthetic-ferromagnet spin torque oscillator. *Phys. Rev. B*, 87:020409, Jan 2013.

[40] C. Klein, C. Petitjean, and X. Waintal. Interplay between nonequilibrium and equilibrium spin torque using synthetic ferrimagnets. *Phys. Rev. Lett.*, 108:086601, Feb 2012.

[41] Y. A. Bychkov and E. I. Rashba. Oscillatory effects and the magnetic susceptibility of carriers in inversion layers. *Journal of Physics C: Solid State Physics*, 17(33):6039, 1984.

[42] M. Heide, G. Bihlmayer, Ph. Mavropoulos, A. Bringer, and S. Blügel. Spin–orbit driven physics at surfaces. *Newsletter of the Psi-K Network*, 78, 2006.

[43] A. Manchon, H. C. Koo, J. Nitta, S. M. Frolov, and R. A. Duine. New perspectives for rashba spin-orbit coupling. *Nat Mater*, 14(9):871–882, Sep 2015. Review.

[44] J. Sinova, D. Culcer, Q. Niu, N. A. Sinitsyn, T. Jungwirth, and A. H. MacDonald. Universal intrinsic spin hall effect. *Phys. Rev. Lett.*, 92:126603, Mar 2004.

[45] S. Datta and B. Das. Electronic analog of the electrooptic modulator. *Applied Physics Letters*, 56(7), 1990.

[46] M Schultz, F Heinrichs, U Merkt, T Colin, T Skauli, and S Løvold. Rashba spin splitting in a gated HgTe quantum well. *Semiconductor Science and Technology*, 11(8):1168, 1996.

[47] J. Nitta, T. Akazaki, H. Takayanagi, and T. Enoki. Gate control of spin-orbit interaction in an inverted $In_{0.53}Ga_{0.47}As/In_{0.52}Al_{0.48}As$ heterostructure. *Phys. Rev. Lett.*, 78:1335–1338, Feb 1997.

[48] I. M. Miron, K. Garello, G. Gaudin, P.-J. Zermatten, M. V. Costache, S. Auffret, S. Bandiera, B. Rodmacq, A. Schuhl, and P. Gambardella. Perpendicular switching of a single ferromagnetic layer induced by in-plane current injection. *Nature*, 476(7359):189–193, Aug 2011.

[49] Z. Duan, A. Smith, L. Yang, B. Youngblood, J. Lindner, V. E. Demidov, S. O. Demokritov, and I. N. Krivorotov. Nanowire spin torque oscillator driven by spin orbit torques. *Nat Commun*, 5, Dec 2014. Article.

[50] Ø. Johansen. Magnetization dynamics of domain walls and skyrmions in micromagnetics. `https://github.com/oyvindjohansen/Ferromagnetism-DW/blob/master/main.pdf`.

[51] P. F. Carcia, A. D. Meinhaldt, and A. Suna. Perpendicular magnetic anisotropy in Pd/Co thin film layered structures. *Applied Physics Letters*, 47(2), 1985.

[52] F. Matsukura, Y. Tokura, and H. Ohno. Control of magnetism by electric fields. *Nat Nano*, 10(3):209–220, Mar 2015. Review.

[53] T. Maruyama, Y. Shiota, T. Nozaki, K. Ohta, N. Toda, M. Mizuguchi, A. Tulapurkar, T. Shinjo, M. Shiraishi, S. Mizukami, Y. Ando, and Y. Suzuki. Large voltage-induced magnetic anisotropy change in a few atomic layers of iron. *Nat Nano*, 4(3):158–161, Mar 2009.

[54] M. A. Ruderman and C. Kittel. Indirect exchange coupling of nuclear magnetic moments by conduction electrons. *Phys. Rev.*, 96:99–102, Oct 1954.

[55] T. Kasuya. A theory of metallic ferro- and antiferromagnetism on Zener's model. *Progress of Theoretical Physics*, 16(1):45–57, 1956.

[56] Kei Yosida. Magnetic properties of Cu-Mn alloys. *Phys. Rev.*, 106:893–898, Jun 1957.

[57] J. H. Van Vleck. Note on the interactions between the spins of magnetic ions or nuclei in metals. *Rev. Mod. Phys.*, 34:681–686, Oct 1962.

[58] S. S. P. Parkin and D. Mauri. Spin engineering: Direct determination of the Ruderman-Kittel-Kasuya-Yosida far-field range function in ruthenium. *Phys. Rev. B*, 44:7131–7134, Oct 1991.

[59] T. Moriya. Anisotropic superexchange interaction and weak ferromagnetism. *Phys. Rev.*, 120:91–98, Oct 1960.

[60] I. E. Dzyaloshinskii. A Thermodynamic Theory of "Weak" Ferromagnetism of Antiferromagnets. *J. Phys. Chem. Solids*, 4:241–255, 1958.

[61] K-W. Kim, H-W. Lee, K-J. Lee, and M. D. Stiles. Chirality from interfacial spin-orbit coupling effects in magnetic bilayers. *Phys. Rev. Lett.*, 111:216601, Nov 2013.

[62] Y-H. Liu and Y-Q. Li. A mechanism to pin skyrmions in chiral magnets. *Journal of Physics: Condensed Matter*, 25(7):076005, 2013.

[63] J. Müller and A. Rosch. Capturing of a magnetic skyrmion with a hole. *Phys. Rev. B*, 91:054410, Feb 2015.

[64] L. D. Landau and E. M. Lifshitz. On the theory of the dispersion of magnetic permeability in ferromagnetic bodies. *Phys. Zeitsch. der Sow.*, 6:153–169, 1935.

[65] T. L. Gilbert. Classics in Magnetics A Phenomenological Theory of Damping in Ferromagnetic Materials. *IEEE Transactions on Magnetics*, 40(6):3443–3449, November 2004.

[66] T. L. Gilbert and J. M. Kelly. Anomalous rotational damping in ferromagnetic sheets. In *Conference on magnetism and magnetic materials: papers presented, Pittsburgh, Pa., June 14-16, 1955*, pages 253–263. American Institute of Electrical Engineers, 1955.

[67] S. Zhang and Z. Li. Roles of Nonequilibrium Conduction Electrons on the Magnetization Dynamics of Ferromagnets. *Phys. Rev. Lett.*, 93(12):127204, 2004.

[68] T.H.R. Skyrme. A unified field theory of mesons and baryons. *Nuclear Physics*, 31:556 – 569, 1962.

[69] S. Heinze, K. von Bergmann, M. Menzel, J. Brede, A. Kubetzka, R. Wiesendanger, G. Bihlmayer, and S. Blugel. Spontaneous atomic-scale magnetic skyrmion lattice in two dimensions. *Nat Phys*, 7(9):713–718, September 2011.

[70] O. A. Tretiakov and O. Tchernyshyov. Vortices in thin ferromagnetic films and the skyrmion number. *Phys. Rev. B*, 75:012408, Jan 2007.

[71] S. Mühlbauer, B. Binz, F. Jonietz, C. Pfleiderer, A. Rosch, A. Neubauer, R. Georgii, and P. Böni. Skyrmion lattice in a chiral magnet. *Science*, 323(5916):915–919, 2009.

[72] N. Nagaosa and Y. Tokura. Topological properties and dynamics of magnetic skyrmions. *Nat Nano*, 8(12):899–911, Dec 2013. Review.

[73] Y. S. Lin, P. J. Grundy, and E. A. Giess. Bubble domains in magnetostatically coupled garnet films. *Applied Physics Letters*, 23(8), 1973.

[74] T. Okubo, S. Chung, and H. Kawamura. Multiple-*q* states and the skyrmion lattice of the triangular-lattice heisenberg antiferromagnet under magnetic fields. *Phys. Rev. Lett.*, 108:017206, Jan 2012.

[75] K. Everschor. *Current-Induced Dynamics of Chiral Magnetic Structures: Skyrmions, Emergent Electrodynamics and Spin-Transfer Torques*. PhD thesis, Mathematisch-Naturwissenschaftlichen Fakultät der Universität zu Köln, 2012.

[76] J. D. Jackson. *Classical Electrodynamics Third Edition*. Wiley, third edition, August 1998.

[77] A. A. Thiele. Steady-state motion of magnetic domains. *Phys. Rev. Lett.*, 30:230–233, Feb 1973.

[78] B. Krüger. *Current-Driven Magnetization Dynamics: Analytical Modeling and Numerical Simulation*. PhD thesis, Institut für Theoretische Physik Universität Hamburg, 2011.

[79] K. Everschor-Sitte and M. Sitte. Real-space berry phases: Skyrmion soccer (invited). *Journal of Applied Physics*, 115(17), 2014.

[80] M. V. Berry. Quantal phase factors accompanying adiabatic changes. *Proceedings of the Royal Society of London. Series A, Mathematical and Physical Sciences*, 392(1802):45–57, 1984.

[81] G. Tatara, H. Kohno, J. Shibata, Y. Lemaho, and K-J. Lee. Spin torque and force due to current for general spin textures. *Journal of the Physical Society of Japan*, 76(5):054707, 2007.

[82] B. Binz and A. Vishwanath. Chirality induced anomalous-hall effect in helical spin crystals. *Physica B: Condensed Matter*, 403(5–9):1336 – 1340, 2008. Proceedings of the International Conference on Strongly Correlated Electron Systems.

[83] J. Ye, Y. B. Kim, A. J. Millis, B. I. Shraiman, P. Majumdar, and Z. Tešanović. Berry phase theory of the anomalous hall effect: Application to colossal magnetoresistance manganites. *Phys. Rev. Lett.*, 83:3737–3740, Nov 1999.

[84] N. Kanazawa. *Charge and Heat Transport Phenomena in Electronic and Spin Structures in B20-type Compounds*. Springer Theses. Springer Japan, 2015.

[85] N. Nagaosa, X. Z. Yu, and Y. Tokura. Gauge fields in real and momentum spaces in magnets: monopoles and skyrmions. *Philosophical Transactions of the Royal Society of London A: Mathematical, Physical and Engineering Sciences*, 370(1981):5806–5819, 2012.

[86] M. Yamanouchi, D. Chiba, F. Matsukura, and H. Ohno. Current-induced domain-wall switching in a ferromagnetic semiconductor structure. *Nature*, 428(6982):539–542, Apr 2004.

[87] A. Yamaguchi, T. Ono, S. Nasu, K. Miyake, K. Mibu, and T. Shinjo. Real-space observation of current-driven domain wall motion in submicron magnetic wires. *Phys. Rev. Lett.*, 92:077205, Feb 2004.

[88] E. Saitoh, H. Miyajima, T. Yamaoka, and G. Tatara. Current-induced resonance and mass determination of a single magnetic domain wall. *Nature*, 432(7014):203–206, Nov 2004.

[89] M. Yamanouchi, D. Chiba, F. Matsukura, T. Dietl, and H. Ohno. Velocity of domain-wall motion induced by electrical current in the ferromagnetic semiconductor (ga,mn)as. *Phys. Rev. Lett.*, 96:096601, Mar 2006.

[90] J. Iwasaki, M. Mochizuki, and N. Nagaosa. Current-induced skyrmion dynamics in constricted geometries. *Nat Nano*, 8(10):742–747, Oct 2013. Article.

[91] W. Jiang, P. Upadhyaya, W. Zhang, G. Yu, M. B. Jungfleisch, F. Y. Fradin, J. E. Pearson, Y. Tserkovnyak, K. L. Wang, O. Heinonen, S. G. E. te Velthuis, and A. Hoffmann. Blowing magnetic skyrmion bubbles. *Science*, 349(6245):283–286, 2015.

[92] T. L. Monchesky. Skyrmions: Detection with unpolarized currents. *Nat Nano*, 10(12):1008–1009, Dec 2015. News and Views.

[93] S. Woo, K. Litzius, B. Kruger, M-Y. Im, L. Caretta, K. Richter, M. Mann, A. Krone, R. M. Reeve, M. Weigand, P. Agrawal, I. Lemesh, M-A. Mawass, P. Fischer, M. Klaui, and G. S. D. Beach. Observation of room-temperature magnetic skyrmions and their current-driven dynamics in ultrathin metallic ferromagnets. *Nat Mater*, 15(5):501–506, May 2016. Letter.

[94] K-W. Kim, S-M. Seo, J. Ryu, K-J. Lee, and H-W. Lee. Magnetization dynamics induced by in-plane currents in ultrathin magnetic nanostructures with Rashba spin-orbit coupling. *Phys. Rev. B*, 85:180404, May 2012.

[95] M. Mochizuki. Spin-wave modes and their intense excitation effects in skyrmion crystals. *Phys. Rev. Lett.*, 108:017601, Jan 2012.

[96] B. Zhang, W. Wang, M. Beg, H. Fangohr, and W. Kuch. Microwave-induced dynamic switching of magnetic skyrmion cores in nanodots. *Applied Physics Letters*, 106(10), 2015.

[97] Y-H. Liu, Y-Q. Li, and J. H. Han. Skyrmion dynamics in multiferroic insulators. *Phys. Rev. B*, 87:100402, Mar 2013.

[98] T. Koyama, D. Chiba, K. Ueda, K. Kondou, H. Tanigawa, S. Fukami, T. Suzuki, N. Ohshima, N. Ishiwata, Y. Nakatani, K. Kobayashi, and T. Ono. Observation of the intrinsic pinning of a magnetic domain wall in a ferromagnetic nanowire. *Nat Mater*, 10(3):194–197, Mar 2011.

[99] K. Everschor, M. Garst, B. Binz, F. Jonietz, S. Mühlbauer, C. Pfleiderer, and A. Rosch. Rotating skyrmion lattices by spin torques and field or temperature gradients. *Phys. Rev. B*, 86:054432, Aug 2012.

[100] J. Iwasaki, M. Mochizuki, and N. Nagaosa. Universal current-velocity relation of skyrmion motion in chiral magnets. *Nat Commun*, 4:1463, Feb 2013.

[101] C. Moreau-Luchaire, C. Moutas, N. Reyren, J. Sampaio, C. A. F. Vaz, N. Van Horne, K. Bouzehouane, K. Garcia, C. Deranlot, P. Warnicke, P. Wohlhüter, J.-M. George, M. Weigand, J. Raabe, V. Cros, and A. Fert. Additive interfacial chiral interaction in multilayers for stabilization of small individual skyrmions at room temperature. *Nat Nano*, advance online publication, Jan 2016.

[102] X. Zhang, M. Ezawa, D. Xiao, G. P. Zhao, Y. Liu, and Y. Zhou. All-magnetic control of skyrmions in nanowires by a spin wave. *Nanotechnology*, 26(22):225701, 2015.

[103] C. Chappert, A. Fert, and Frederic Nguyen Van Dau. The emergence of spin electronics in data storage. *Nat Mater*, 6(11):813–823, Nov 2007.

[104] D.C. Ralph and M.D. Stiles. Spin transfer torques. *Journal of Magnetism and Magnetic Materials*, 320(7):1190 – 1216, 2008.

[105] J. Iwasaki, A. J. Beekman, and N. Nagaosa. Theory of magnon-skyrmion scattering in chiral magnets. *Phys. Rev. B*, 89:064412, Feb 2014.

[106] M. Mochizuki, X. Z. Yu, S. Seki, N. Kanazawa, W. Koshibae, J. Zang, M. Mostovoy, Y. Tokura, and N. Nagaosa. Thermally driven ratchet motion of a skyrmion microcrystal and topological magnon hall effect. *Nat Mater*, 13(3):241–246, Mar 2014. Letter.

[107] S. A. Bender and Y. Tserkovnyak. Thermally driven spin torques in layered magnetic insulators. *Phys. Rev. B*, 93:064418, Feb 2016.

Appendices

A

Rashba force in the Thiele equation

The Rashba force in the Thiele equation is given by

$$\boldsymbol{F}_{\mathrm{R}} = -\mu_0 \int \mathrm{d}V \sum_k (\nabla M_k) \left(\boldsymbol{H}_{\mathrm{R}} - \frac{\beta}{M_s} \boldsymbol{M} \times \boldsymbol{H}_{\mathrm{R}} \right)_k \tag{A.1}$$

with $\boldsymbol{H}_{\mathrm{R}} = C_{\mathrm{R}} b_J \hat{\boldsymbol{y}}$ for a broken inversion symmetry in the z-direction and an applied current in the x-direction. We will first consider the force

$$\boldsymbol{F}_{\mathrm{R}}^{(1)} = -\mu_0 \int \mathrm{d}V \sum_k (\nabla M_k) \left(\boldsymbol{H}_{\mathrm{R}} \right)_k . \tag{A.2}$$

To do this we must know $\partial_x m_y$ and $\partial_y m_y$. We note for the remainder of this chapter that $\partial_z \boldsymbol{M} = 0$. To find these derivatives we use the chain rule and the following relations obtained from the ansatz $\theta = \theta(r)$ and identity $\tan \phi = x/y$:

$$\partial_x \theta = \cos \phi \partial_r \theta, \tag{A.3a}$$

$$\partial_y \theta = \sin \phi \partial_r \theta, \tag{A.3b}$$

$$\partial_x \Phi = -\frac{\sin \phi}{r}, \tag{A.3c}$$

$$\partial_y \Phi = \frac{\cos \phi}{r}. \tag{A.3d}$$

We then find that

$$\partial_x m_y = \partial_x (\sin \theta \sin \Phi) = \cos \theta \sin \Phi \cos \phi \partial_r \theta - \frac{\sin \theta}{r} \cos \Phi \sin \phi, \tag{A.4a}$$

$$\partial_y m_y = \partial_y (\sin \theta \sin \Phi) = \cos \theta \sin \Phi \sin \phi \partial_r \theta + \frac{\sin \theta}{r} \cos \Phi \cos \phi. \tag{A.4b}$$

Using these results we end up with the force

$$\boldsymbol{F}_{\mathrm{R}}^{(1)} = -\mu_0 C_{\mathrm{R}} b_J M_s \int \mathrm{d}V \begin{pmatrix} (\sin \psi + \cos \Phi \sin \phi) \partial_r \theta - \frac{\sin \theta}{r} \cos \Phi \sin \phi \\ (\cos \psi - \cos \Phi \cos \phi) \partial_r \theta + \frac{\sin \theta}{r} \cos \Phi \cos \phi \\ 0 \end{pmatrix}, \tag{A.5}$$

where we have used the relations

$$\sin\Phi\cos\phi - \cos\Phi\sin\phi = \sin\psi, \tag{A.6a}$$

$$\sin\Phi\sin\phi + \cos\Phi\cos\phi = \cos\psi. \tag{A.6b}$$

In the case of $\psi = 0$ or $\psi = \pi$, we can easily see that two of the components of $\boldsymbol{F}_R^{(1)}$ are zero, as $\sin\psi = 0$ and $\int \mathrm{d}\phi \cos\phi\sin\phi = 0$. The y-component can also be seen to be zero. As $\cos\Phi\cos\phi = \cos^2\phi$ and $(\cos\psi - \cos\Phi\cos\phi) = \sin^2\phi$ for $\psi = 0$, $\cos\Phi\cos\phi = -\cos^2\phi$ and $(\cos\psi - \cos\Phi\cos\phi) = -\sin^2\phi$ for $\psi = \pi$, after performing the integral over ϕ we remain with a constant times the integral

$$\int_0^\infty \mathrm{d}r \left(r\cos\theta\partial_r\theta + \sin\theta\right). \tag{A.7}$$

This integral is zero as well, as one can see by performing a partial integration of $\sin\theta(r)$:

$$\int_0^\infty \mathrm{d}r \sin\theta = r\sin\theta|_{r=0}^{r=\infty} - \int_0^\infty \mathrm{d}r\, r\cos\theta\partial_r\theta. \tag{A.8}$$

Rearranging the terms gives us

$$\int_0^\infty \mathrm{d}r \left(r\cos\theta\partial_r\theta + \sin\theta\right) = r\sin\theta|_{r=0}^{r=\infty} = 0. \tag{A.9}$$

This integral is zero because $\sin\theta(r)$ decays faster than $1/r$ and is finite at $r = 0$, which can be verified numerically. We have then shown that $\boldsymbol{F}_R^{(1)} = 0$ for $\psi = 0, \pi$. It can be shown in a similar manner that $\boldsymbol{F}_R^{(1)} = 0$ for $\psi = \pm\pi/2$ as well. We then proceed to consider the second part of the force,

$$\boldsymbol{F}_R^{(2)} = -\mu_0 \int \mathrm{d}V \sum_k (\nabla M_k) \left(-\frac{\beta}{M_s}\boldsymbol{M} \times \boldsymbol{H}_R\right)_k. \tag{A.10}$$

The cross-product in the magnetic field can be written out as $-\beta\boldsymbol{m}\times\boldsymbol{H}_R = \beta C_R b_J(\cos\theta\hat{\boldsymbol{x}} - \sin\theta\cos\Phi\hat{\boldsymbol{z}})$. The partial derivatives of m_x and m_z are found to be

$$\partial_x m_x = \partial_x(\sin\theta\cos\Phi) = \cos\theta\cos\Phi\cos\phi\partial_r\theta + \frac{\sin\theta}{r}\sin\Phi\sin\phi, \tag{A.11a}$$

$$\partial_y m_x = \partial_y(\sin\theta\cos\Phi) = \cos\theta\cos\Phi\sin\phi\partial_r\theta - \frac{\sin\theta}{r}\sin\Phi\cos\phi, \tag{A.11b}$$

$$\partial_x m_z = \partial_x \cos\theta = -\sin\theta\cos\phi\partial_r\theta, \tag{A.11c}$$

$$\partial_y m_z = \partial_x \cos\theta = -\sin\theta\sin\phi\partial_r\theta. \tag{A.11d}$$

Inserting this into the expression for $\boldsymbol{F}_R^{(2)}$ in (A.10) we find that it can be expressed as

$$\boldsymbol{F}_R^{(2)} = -\mu_0\beta C_R b_J M_s \int \mathrm{d}V \begin{pmatrix} (\cos\psi - \sin\Phi\sin\phi)\partial_r\theta + \frac{\sin\theta\cos\theta}{r}\sin\Phi\sin\phi \\ (\sin\Phi\cos\phi - \sin\psi)\partial_r\theta - \frac{\sin\theta\cos\theta}{r}\sin\Phi\cos\phi \\ 0 \end{pmatrix}. \tag{A.12}$$

In the case of $\psi = 0$ or $\psi = \pi$ it can be seen that the only non-vanishing component is the x-component, due to the integration over ϕ. It can be verified that the resulting force vector becomes

$$\boldsymbol{F}_R = \boldsymbol{F}_R^{(2)} = -\mu_0\beta C_R b_J M_s\pi d \int_0^\infty \mathrm{d}r \left(r\partial_r\theta + \sin\theta\cos\theta\right) \begin{pmatrix} \cos\psi \\ -\sin\psi \\ 0 \end{pmatrix}, \tag{A.13}$$

with d being the thickness in the z-direction. This result is only valid when $\psi = 0, \pm\pi/2, \pi$, but it should be noted that for the uni-axial inversion asymmetry along $\hat{\boldsymbol{n}}$ defining the Rashba field used here the hedgehog skyrmion with $\psi = 0$ or $\psi = \pi$ is the energetically favored skyrmion profile.

B

Fourier transform of LLGS into an eigenvalue equation

The LLGS equation that we will consider in this appendix is given by

$$\partial_t \boldsymbol{m}_i = -\gamma \boldsymbol{m}_i \times \left(\boldsymbol{H}_i^{\text{eff}} + \boldsymbol{H}_i^{\text{R}} - \beta \boldsymbol{m}_i \times \boldsymbol{H}_i^{\text{R}} \right) + \alpha \boldsymbol{m}_i \times \partial_t \boldsymbol{m}_i + \boldsymbol{T}_i^{\text{STT}}, \tag{B.1}$$

with the fields and torques being given by

$$\boldsymbol{H}_i^{\text{eff}} = \frac{\omega_0}{\gamma} \left(\boldsymbol{m}_i \cdot \hat{\boldsymbol{n}}_k \right) \hat{\boldsymbol{n}}_k + \frac{\omega_J}{\gamma} \boldsymbol{m}_{\bar{i}}, \tag{B.2a}$$

$$\boldsymbol{H}_i^{\text{R}} = \frac{\omega_{\text{R}}}{\gamma(1 + \beta^2)} P_i^{(\hat{\boldsymbol{j}} \cdot \hat{\boldsymbol{r}})} \hat{\boldsymbol{n}} \times \hat{\boldsymbol{j}}, \tag{B.2b}$$

$$\boldsymbol{T}_1^{\text{STT}} = -\frac{\omega_j^{(x)}}{\gamma} \boldsymbol{m}_1 \times \left(P_0^{(x)} \boldsymbol{m}_0 - P_1^{(x)} \boldsymbol{m}_2 \right) \times \boldsymbol{m}_1, \tag{B.2c}$$

$$\boldsymbol{T}_2^{\text{STT}} = -\frac{\omega_j^{(x)}}{\gamma} P_1^{(x)} \boldsymbol{m}_2 \times \boldsymbol{m}_1 \times \boldsymbol{m}_2. \tag{B.2d}$$

B.1 Bulk geometry

We start off by considering the bulk geometry, which has an easy axis in the z-direction, making $\hat{\boldsymbol{n}}_k = \hat{\boldsymbol{z}}$. The main inversion asymmetry is in the x-direction, and the current giving rise to the Rashba field is applied in the y-direction. The direction of the Rashba field $\boldsymbol{H}_i^{\text{R}}$ then becomes $\hat{\boldsymbol{x}} \times \hat{\boldsymbol{y}} = \hat{\boldsymbol{z}}$. We then make the ansatz that $\boldsymbol{m}_i = u_i^x(t)\hat{\boldsymbol{x}} + u_i^y(t)\hat{\boldsymbol{y}} + \lambda_i \hat{\boldsymbol{z}}$. In addition, we perform a Fourier transform such that

$$\boldsymbol{u}_i(t) = \int \tilde{\boldsymbol{u}}_i(\omega) \exp\left(-i\omega t\right) \mathrm{d}\omega/2\pi. \tag{B.3}$$

81

Starting from the left of (B.1), the terms to first order in u then become

$$\partial_t \boldsymbol{m}_i = -i\omega \left(\tilde{u}_i^x \hat{\boldsymbol{x}} + \tilde{u}_i^y \hat{\boldsymbol{y}} \right), \tag{B.4a}$$

$$-\gamma \boldsymbol{m}_i \times \boldsymbol{H}_i^{\text{eff}} = -\omega_0 \lambda_i \left(\tilde{u}_i^y \hat{\boldsymbol{x}} - \tilde{u}_i^x \hat{\boldsymbol{y}} \right)$$
$$- \omega_J \left[\left(\lambda_{\bar{i}} \tilde{u}_i^y - \lambda_i \tilde{u}_{\bar{i}}^y \right) \hat{\boldsymbol{x}} - \left(\lambda_{\bar{i}} \tilde{u}_i^x - \lambda_i \tilde{u}_{\bar{i}}^x \right) \hat{\boldsymbol{y}} \right], \tag{B.4b}$$

$$-\gamma \boldsymbol{m}_i \times \boldsymbol{H}_i^{\text{R}} = -\frac{\omega_{\text{R}}}{1+\beta^2} P_i^{(y)} \left(\tilde{u}_i^y \hat{\boldsymbol{x}} - \tilde{u}_i^x \hat{\boldsymbol{y}} \right), \tag{B.4c}$$

$$\gamma \beta \boldsymbol{m}_i \times \boldsymbol{m}_i \times \boldsymbol{H}_i^{\text{R}} = \frac{\beta \omega_{\text{R}}}{1+\beta^2} P_i^{(y)} \lambda_i \ \left(\tilde{u}_i^x \hat{\boldsymbol{x}} + \tilde{u}_i^y \hat{\boldsymbol{y}} \right), \tag{B.4d}$$

$$\alpha \boldsymbol{m}_i \times \partial_t \boldsymbol{m}_i = i\alpha\omega\lambda_i \left(\tilde{u}_i^y \hat{\boldsymbol{x}} - \tilde{u}_i^x \hat{\boldsymbol{y}} \right), \tag{B.4e}$$

$$\boldsymbol{T}_1^{\text{STT}} = \omega_j^{(x)} \lambda_1 P_0^{(x)} \left(\tilde{u}_1^x \hat{\boldsymbol{x}} + \tilde{u}_1^y \hat{\boldsymbol{y}} \right)$$
$$+ \omega_j^{(x)} P_1^{(x)} \left[\left(-\lambda_1 \lambda_2 \tilde{u}_1^x + \tilde{u}_2^x \right) \hat{\boldsymbol{x}} + \left(-\lambda_1 \lambda_2 \tilde{u}_1^y + \tilde{u}_2^y \right) \hat{\boldsymbol{y}} \right], \tag{B.4f}$$

$$\boldsymbol{T}_2^{\text{STT}} = -\omega_j^{(x)} P_1^{(x)} \left[\left(-\lambda_1 \lambda_2 \tilde{u}_1^x + \tilde{u}_2^x \right) \hat{\boldsymbol{x}} + \left(-\lambda_1 \lambda_2 \tilde{u}_1^y + \tilde{u}_2^y \right) \hat{\boldsymbol{y}} \right]. \tag{B.4g}$$

We want to express the equations above as a linear combination of $\tilde{\boldsymbol{u}}_i$, as then it will be possible to get the LLGS equation on the form of an eigenvalue equation. For some terms, such as (B.4a) this will be trivial, whereas for other terms, such as (B.4c) it becomes a little harder. To deal with these terms that result from the cross-products, we utilize the periodic nature of the Fourier transform. In Figure B.1 we see that the terms in (B.4) that can not be written directly as a linear combination in $\tilde{\boldsymbol{u}}_i$ are terms that are a phase $\pi/2$ ahead or behind $\tilde{\boldsymbol{u}}_i$. A rotation of something complex by an angle $\pi/2$ is equivalent to multiplying it with the imaginary number i. Therefore, $\left(-\tilde{u}_i^y \hat{\boldsymbol{x}} + \tilde{u}_i^x \hat{\boldsymbol{y}} \right) = i \left(\tilde{u}_i^x \hat{\boldsymbol{x}} + \tilde{u}_i^y \hat{\boldsymbol{y}} \right)$ and $\left(\tilde{u}_i^y \hat{\boldsymbol{x}} - \tilde{u}_i^x \hat{\boldsymbol{y}} \right) = -i \left(\tilde{u}_i^x \hat{\boldsymbol{x}} + \tilde{u}_i^y \hat{\boldsymbol{y}} \right)$. Using this, we find that the LLGS equations can be written as

$$\left[-(i+\alpha\lambda_1)\omega - i\omega_0\lambda_1 - i\omega_J\lambda_2 - \frac{\omega_{\text{R}}}{1+\beta^2} P_1^{(y)}(i+\beta\lambda_1) + \omega_j^{(x)}\lambda_1(\lambda_2 P_1^{(x)} - P_0^{(x)}) \right] \tilde{\boldsymbol{u}}_1$$
$$+ \left[i\omega_J\lambda_1 - \omega_j^{(x)} P_1^{(x)} \right] \tilde{\boldsymbol{u}}_2 = 0, \tag{B.5a}$$

$$\left[i\omega_J\lambda_2 + \omega_j^{(x)} P_1^{(x)} \right] \tilde{\boldsymbol{u}}_1$$
$$+ \left[-(i+\alpha\lambda_2)\omega - i\omega_0\lambda_2 - i\omega_J\lambda_1 - \frac{\omega_{\text{R}}}{1+\beta^2} P_1^{(y)}(i+\beta\lambda_2) - \omega_j^{(x)}\lambda_1\lambda_2 P_1^{(x)} \right] \tilde{\boldsymbol{u}}_2 = 0. \tag{B.5b}$$
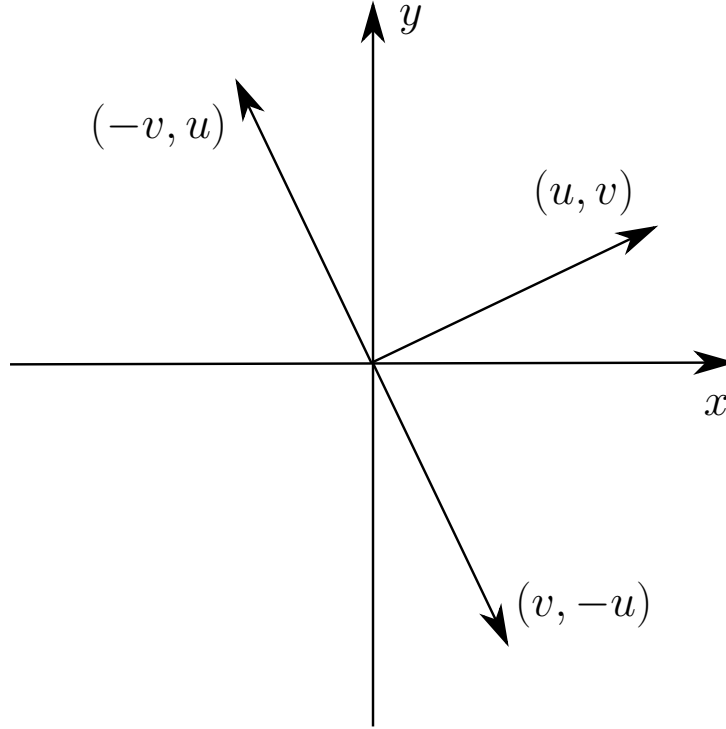
Multiplying the equations above with i, we can write the equations compactly as

$$\left(\bar{A}\omega + \bar{V} \right) \begin{pmatrix} \tilde{\boldsymbol{u}}_1 \\ \tilde{\boldsymbol{u}}_2 \end{pmatrix} = 0, \tag{B.6}$$

with

$$\bar{A} = \begin{pmatrix} 1 - i\alpha\lambda_1 & 0 \\ 0 & 1 - i\alpha\lambda_2 \end{pmatrix}, \tag{B.7a}$$

$$\bar{V} = \omega_0 \begin{pmatrix} \lambda_1 & 0 \\ 0 & \lambda_2 \end{pmatrix} + \omega_J \begin{pmatrix} \lambda_2 & -\lambda_1 \\ -\lambda_2 & \lambda_1 \end{pmatrix} + i\omega_j^{(x)} \left[P_0 \begin{pmatrix} -\lambda_1 & 0 \\ 0 & 0 \end{pmatrix} + P_1 \begin{pmatrix} \lambda_1\lambda_2 & -1 \\ 1 & -\lambda_1\lambda_2 \end{pmatrix} \right]$$
$$\frac{\omega_{\text{R}}^{(y)}}{1+\beta^2} \left[\begin{pmatrix} P_1^{(y)} & 0 \\ 0 & P_2^{(y)} \end{pmatrix} - i\beta \begin{pmatrix} P_1^{(y)}\lambda_1 & 0 \\ 0 & P_2^{(y)}\lambda_2 \end{pmatrix} \right]. \tag{B.7b}$$

Figure B.1. The vector $(-v, u)$ is a phase $\pi/2$ ahead of the vector (u, v), while the vector $(v, -u)$ is a phase $\pi/2$ behind the vector (u, v).

B.2 Thin film geometry

When considering the thin film geometry, there are four differences from the bulk geometry. Firstly, the easy axis is along $\hat{\boldsymbol{n}}_k = \hat{\boldsymbol{y}}$ instead of $\hat{\boldsymbol{n}}_k = \hat{\boldsymbol{z}}$. Secondly, the main inversion asymmetry is in the z-direction and there is only an applied current in the x-direction, so that the direction of the Rashba field becomes $\hat{\boldsymbol{z}} \times \hat{\boldsymbol{x}} = \hat{\boldsymbol{y}}$. For the bulk case this was also directed along $\hat{\boldsymbol{z}}$. Thirdly, as the easy axis is along $\hat{\boldsymbol{y}}$, we use the ansatz $\boldsymbol{m}_i = u_i^x \hat{\boldsymbol{x}} + \lambda_i \hat{\boldsymbol{y}} + u_i^z \hat{\boldsymbol{z}}$. Lastly, the polarizations in the Rashba field are given by the polarizations of the current in the x-direction, so that $\boldsymbol{H}_i^{\text{R}} \propto P_{i-1}^{(x)}$. With the exception of the last change, the difference between the thin film geometry and the bulk geometry is mainly a switch between the y- and z-directions. This makes it easier for us to find the matrices $\bar{A}$ and $\bar{V}$ for the thin film geometry. When switching two column vectors in a determinant you pick up a negative sign. When we switch the y- and z-directions, we therefore pick up a negative sign for the terms that stem from an odd number of cross products. Using this in addition to the fact that it is the current in the x-direction that generates the Rashba field, the equations for the thin film geometry can also be written in the form of (B.6) with

$$\bar{A} = \begin{pmatrix} 1 + i\alpha\lambda_1 & 0 \\ 0 & 1 + i\alpha\lambda_2 \end{pmatrix}, \tag{B.8a}$$

$$\bar{V} = -\omega_0 \begin{pmatrix} \lambda_1 & 0 \\ 0 & \lambda_2 \end{pmatrix} - \omega_J \begin{pmatrix} \lambda_2 & -\lambda_1 \\ -\lambda_2 & \lambda_1 \end{pmatrix} + i\omega_j^{(x)} \left[P_0 \begin{pmatrix} -\lambda_1 & 0 \\ 0 & 0 \end{pmatrix} + P_1 \begin{pmatrix} \lambda_1\lambda_2 & -1 \\ 1 & -\lambda_1\lambda_2 \end{pmatrix} \right]$$

$$\frac{\omega_{\text{R}}^{(y)}}{1 + \beta^2} \left[\begin{pmatrix} -P_0^{(x)} & 0 \\ 0 & P_1^{(x)} \end{pmatrix} - i\beta \begin{pmatrix} P_0^{(x)}\lambda_1 & 0 \\ 0 & P_1^{(x)}\lambda_2 \end{pmatrix} \right]. \tag{B.8b}$$

C

Spin torque oscillator research article

Here we enclose the article based on our results regarding spin torque oscillators, currently undergoing review in Nature Scientific Reports.

Current driven spin–orbit torque oscillator: ferromagnetic and antiferromagnetic coupling

Øyvind Johansen[1] **and Jacob Linder**[1,*]

[1]Department of Physics, Norwegian University of Science and Technology, N-7491 Trondheim, Norway
[*]Corresponding author: jacob.linder@ntnu.no

ABSTRACT

We consider theoretically the impact of Rashba spin–orbit coupling on spin torque oscillators (STOs) in synthetic ferromagnets and antiferromagnets that have either a bulk multilayer or a thin film structure. The synthetic magnets consist of a fixed polarizing layer and two free magnetic layers that interact through the Ruderman-Kittel-Kasuya-Yosida interaction. We determine analytically which collinear states along the easy axis that are stable, and establish numerically the phase diagram for when the system is in the STO mode and when collinear configurations are stable, respectively. It is found that the Rashba spin–orbit coupling can induce anti-damping in the vicinity of the collinear states, which assists the spin transfer torque in generating self-sustained oscillations, and that it can substantially increase the STO part of the phase diagram. Moreover, we find that the STO phase can extend deep into the antiferromagnetic regime in the presence of spin–orbit torques.

Introduction

Twenty years ago, it was theoretically proposed by Slonczewski[1] and Berger[2] that there could be exerted a torque on the magnetization in multilayer systems by passing a spin polarized current through the magnetic layers. This was coined the spin-transfer torque (STT) as the spin of the spin polarized current was transferred to the magnetic layer. This effect was observed experimentally[3,4] a few years after the publications by Slonczewski and Berger, and spiked a lot of interest in the field as the magnetization could now be manipulated by electrical means, which is often advantageous practically compared to manipulation by magnetic fields. This torque could be used to switch the magnetization direction in one of the magnetic layers above some critical current,[4–6] which is of interest for writing techniques in memory technologies such as MRAM[7,8] and racetrack memories.[9] The spin-transfer torque was also shown to induce a precession in the free magnetic layers,[10–12] which is now known as a spin torque oscillator (STO). The spin torque oscillator takes in a dc spin polarized current, and due to the precession in the free magnetic layers that causes an oscillation in the resistance through the giant magnetoresistance effect,[13,14] and the result is an ac current passing out of the multilayers. These alternating currents can have a wide range of frequencies, spanning the range of 100s of MHz to 100s of GHz,[8,15,16] and these frequencies are tunable by the magnitude of the applied current. Spin torque oscillators can exist in both antiferromagnetically[17] and feromagnetically[18] coupled magnetic layers, although it was noted in Ref.[18] that they were unable to reproduce the antiferromagnetic STO phase predicted in Ref.[17] Antiferromagnetic nano-oscillators were also recently considered in Ref.[19]

Another type of torque that has gained interest in magnetization dynamics in more recent years is the torque resulting from Rashba spin–orbit coupling (RSOC).[20] This type of spin–orbit coupling occurs in materials with broken inversion symmetry, such as at the interface between two materials.[21] This inversion asymmetry causes an in-plane current flowing parallel to the interface to experience a magnetic field perpendicular to both the direction of the current and inversion asymmetry.[22] Rashba spin–orbit coupling has been shown to introduce interesting effects in many different areas of physics,[23] and is of particular interest due to the fact that the strength of the interaction can be tuned by gate voltages.[24,25] RSOC can, like STT, be utilized in magnetization switching, although RSOC is not the mechanism solely responsible for it.[26] Several works have considered the influence of spin–orbit torques on magnetic domain wall motion.[27–37] It has also been observed experimentally that the spin–orbit torque from RSOC can contribute to self-oscillations in STOs.[38]

In this article, we show that RSOC can be used in metallic multilayer systems to substantially increase the size of the STO phase. Moreover, we discover an STO phase for two compensated antiferromagnetically coupled magnetic layers, which is a new result compared to *e.g.* Zhou *et al.* who could only find an STO phase for a ferromagnetic coupling in Ref.,[18] and Klein *et al.* could only find an STO phase for uncompensated antiferromagnetically coupled magnetic layers in Ref.[17] We begin by setting up our model by utilizing the Landau-Liftshitz-Gilbert-Slonczewski (LLGS) equation, and then proceed by performing a Fourier transform of this equation to find when collinear states along the easy axis are stable. By comparing the new terms introduced by having RSOC present, we find that the spin–orbit torques effectively can be described by a modification of the

Gilbert damping α, to the extent where we can get an anti-damping term in the LLGS equation. To establish when we have an STO phase we solve the full LLGS equation numerically for different sets of experimentally relevant parameters, considering two possible geometries, and use the solutions to classify the phases. Lastly, we analyze the frequency spectrum of the STO phases by performing a Fourier transform of the solutions along different lines in the phase diagrams.

Theory

We will consider two different geometries where spin–orbit torques strongly influence the STO phase, and which display different behaviors. These geometries will henceforth be called the bulk and thin film geometries, and are illustrated in Figure 1. Both geometries consist of a polarizing layer F_0 and two free magnetic layers F_1 an F_2, all separated by a non-magnetic metal in order to reduce the exchange coupling and prevent magnetic locking. The main differences between the geometries is the direction of which the inversion symmetry is broken, and the current that is required to induce the spin–orbit coupling. In the bulk geometry the current in the y-direction induces spin–orbit torques from RSOC, while the current in the x-direction induces the STT. In the thin film geometry, however, both STT and RSOC are caused by the same current in the x-direction, making it impossible so separate the effects from one another. In contrast, this is possible in the bulk geometry.
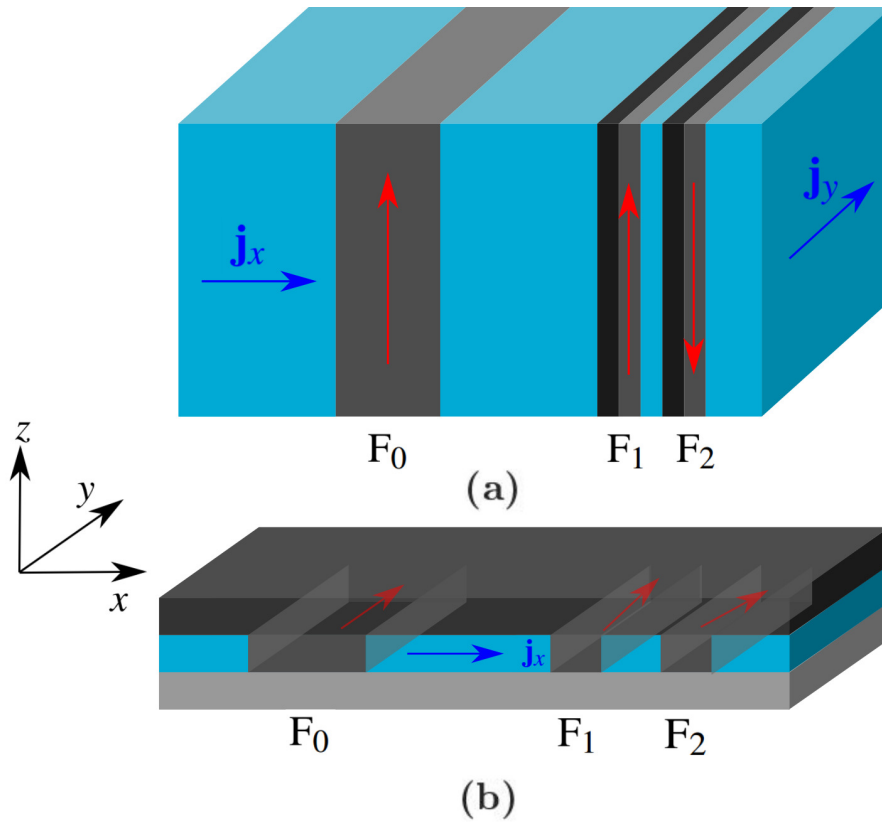
Figure 1. Illustrations of **(a)** the bulk geometry and **(b)** the thin film geometry. In both geometries, a fixed magnetic layer F_0 is separated from two free magnetic layers F_1 and F_2 by a non-magnetic metallic material shown here in blue. A material illustrated in black, which is neighboring to F_1 and F_2 in **(a)** and the top film in **(b)**, is present to get a strong Rashba spin–orbit coupling at the interface of the free ferromagnetic layers. A suitable choice for this material could be a heavy normal metal such as Au or Pt. In **(b)** the bottom film is a substrate which we assume does not induce any measurable interfacial spin–orbit coupling effects. To induce dynamics a current is applied in the x-direction which causes $\mathbf{m}_1$ and $\mathbf{m}_2$ to experience spin-transfer torques. In **(a)** a current is also applied in the y-direction to create significant RSOC effects on $\mathbf{m}_1$ and $\mathbf{m}_2$ due to the symmetry breaking in the x-direction. In the film geometry this is caused by the current in the x-direction as the symmetry breaking is in the z-direction. The free magnetic layers also interact through the RKKY interaction, while the distance to the fixed magnetic layer is chosen such that an RKKY interaction with this layer can be neglected. In **(a)** the material has an easy axis in the z-direction, while in **(b)** the material has an easy axis in the y-direction.

The model for the dynamics of the magnetizations in the two free magnetic layers that we will study in this article is a

variation of two coupled Landau–Lifshitz–Gilbert–Slonczewski (LLGS) equations. This equation is given by

$$\partial_t \mathbf{m}_i = -\gamma \mathbf{m}_i \times \left(\mathbf{H}_i^{\text{eff}} + \mathbf{H}_i^R - \beta \mathbf{m}_i \times \mathbf{H}_i^R \right) + \alpha \mathbf{m}_i \times \partial_t \mathbf{m}_i + \mathbf{T}_i^{\text{STT}}. \tag{1}$$

Here the Rashba field $\mathbf{H}_i^R$ is given by[27]

$$\mathbf{H}_i^R = \frac{1}{1+\beta^2} \frac{\alpha_R m_e P(i) j}{e M_s \hbar \mu_0} \hat{\mathbf{n}} \times \hat{\mathbf{j}}, \tag{2}$$

with α_R being the Rashba parameter, $P(i)$ the polarization of the current j passing through F_i, and $\hat{\mathbf{n}}$ the direction of inversion asymmetry. The parameter β is the non-adiabatic damping parameter of the itinerant electrons that describes the ratio of the inverse exchange interaction parameter $1/J_{\text{ex}}$ and the spin-flip relaxation time. Lastly, the spin-transfer torques $\mathbf{T}_i^{\text{STT}}$ are acting on $\mathbf{m}_i$ are

$$\mathbf{T}_1^{\text{STT}} = -\frac{\gamma \hbar j_x}{2 e M_s \mu_0 d} \mathbf{m}_1 \times (P_0 \mathbf{m}_0 - P_1 \mathbf{m}_2) \times \mathbf{m}_1, \tag{3a}$$

$$\mathbf{T}_2^{\text{STT}} = -\frac{\gamma \hbar j_x}{2 e M_s \mu_0 d} P_1 \mathbf{m}_2 \times \mathbf{m}_1 \times \mathbf{m}_2, \tag{3b}$$

with d being the thickness of the regions F_1 and F_2 in the x-direction, and P_0 and P_1 being the polarization of the current in the non-magnetic material in $F_0/N/F_1$ and $F_1/N/F_2$ respectively. Due to the symmetry of the geometry we can neglect the non-adiabatic spin transfer torque.[39] For the effective field $\mathbf{H}_{\text{eff}}$, we consider contributions from the RKKY interaction and magnetic anisotropy. The effective field then becomes

$$\mathbf{H}_i^{\text{eff}} = \frac{2K}{\mu_0 M_s} (\mathbf{m}_i \cdot \hat{\mathbf{n}}_k) \hat{\mathbf{n}}_k + \frac{J}{\mu_0 M_s d} \mathbf{m}_{\bar{i}}. \tag{4}$$

K is the anisotropy strength, $\hat{\mathbf{n}}_k$ a direction along the easy axis ($\hat{\mathbf{n}}_k = \hat{\mathbf{z}}$ for the bulk geometry, and $\hat{\mathbf{n}}_k = \hat{\mathbf{y}}$ for the thin film geometry), J is the strength of the RKKY interaction, and the index $\bar{i}$ denotes the index of the free magnetization that is not $\mathbf{m}_i$ ($\bar{i} = 3 - i$).

We now follow the procedure by Zhou et al.[18] and consider when the collinear states of $\mathbf{m}_1$ and $\mathbf{m}_2$ along the easy axis are stable or not. We start off with the ansatz that there is a slight perturbation $\mathbf{u}_i$ from the collinear state, such that $\mathbf{m}_i = \lambda_i \hat{\mathbf{n}}_k + \mathbf{u}_i$ ($\lambda_i = \pm 1$). Plugging this ansatz into (1) and performing a Fourier transform $\mathbf{u}_i(t) = \int \tilde{\mathbf{u}}_i(\omega) \exp(-i\omega t) \, d\omega / 2\pi$, we get a result that is on the form

$$\left(\hat{A}\omega + \hat{V} \right) \begin{pmatrix} \tilde{\mathbf{u}}_1 \\ \tilde{\mathbf{u}}_2 \end{pmatrix} = 0. \tag{5}$$

The matrices for the different geometries are given by

$$\hat{A}_{\text{bulk}} = \begin{pmatrix} 1 - i\alpha\lambda_1 & 0 \\ 0 & 1 - i\alpha\lambda_2 \end{pmatrix}, \tag{6a}$$

$$\hat{A}_{\text{film}} = \begin{pmatrix} 1 + i\alpha\lambda_1 & 0 \\ 0 & 1 + i\alpha\lambda_2 \end{pmatrix}, \tag{6b}$$

$$\hat{V}_{\text{bulk}} = \omega_0 \begin{pmatrix} \lambda_1 & 0 \\ 0 & \lambda_2 \end{pmatrix} + \omega_J \begin{pmatrix} \lambda_2 & -\lambda_1 \\ -\lambda_2 & \lambda_1 \end{pmatrix} + i\omega_j^{(x)} \left[P_0 \begin{pmatrix} -\lambda_1 & 0 \\ 0 & 0 \end{pmatrix} + P_1 \begin{pmatrix} \lambda_1\lambda_2 & -1 \\ 1 & -\lambda_1\lambda_2 \end{pmatrix} \right]$$
$$\frac{\omega_R^{(y)}}{1+\beta^2} \left[\begin{pmatrix} P_1^{(y)} & 0 \\ 0 & P_2^{(y)} \end{pmatrix} - i\beta \begin{pmatrix} P_1^{(y)}\lambda_1 & 0 \\ 0 & P_2^{(y)}\lambda_2 \end{pmatrix} \right], \tag{6c}$$

$$\hat{V}_{\text{film}} = -\omega_0 \begin{pmatrix} \lambda_1 & 0 \\ 0 & \lambda_2 \end{pmatrix} - \omega_J \begin{pmatrix} \lambda_2 & -\lambda_1 \\ -\lambda_2 & \lambda_1 \end{pmatrix} + i\omega_j^{(x)} \left[P_0 \begin{pmatrix} -\lambda_1 & 0 \\ 0 & 0 \end{pmatrix} + P_1 \begin{pmatrix} \lambda_1\lambda_2 & -1 \\ 1 & -\lambda_1\lambda_2 \end{pmatrix} \right]$$
$$- \frac{\omega_R^{(x)}}{1+\beta^2} \left[\begin{pmatrix} P_0 & 0 \\ 0 & P_1 \end{pmatrix} + i\beta \begin{pmatrix} P_0\lambda_1 & 0 \\ 0 & P_1\lambda_2 \end{pmatrix} \right]. \tag{6d}$$

Here, we have defined the frequencies $\omega_0 = 2\gamma K/\mu_0 M_s$, $\omega_J = \gamma J/\mu_0 M_s d$, $\omega_j^{(x)} = \gamma \hbar j_x/2\mu_0 M_s d$ and $\omega_R^{(x/y)} = \gamma \alpha_R m_e j_{x/y}/\hbar \mu_0 e M_s$. We now want to determine if any of the collinear states are stable when the frequencies and other constants are specified.

This can be seen from the sign of the imaginary component of ω; when the imaginary component is negative, $\exp(-i\omega t)$ is a decreasing function in time, while if the imaginary component is positive the function is exponentially increasing. Any small perturbation away from the collinear state is then unstable if $\Im m(\omega) > 0$. The value of ω can be determined from (5), as it can be written as an eigenvalue equation where ω is an eigenvalue of the matrix $\hat{W} = -\hat{A}^{-1}\hat{V}$. From this one can then find for what choice of parameters none of the collinear states are stable. An STO phase will be localized within this region, but the entire region is not necessarily an STO phase. We here distinguish between the STO phase and a canted phase by considering the temporal evolution of the magnetoresistance, which is approximated by

$$R(t) = R_0 + \Delta R_1 \mathbf{m}_0 \cdot \mathbf{m}_1 + \Delta R_2 \mathbf{m}_1 \cdot \mathbf{m}_2. \tag{7}$$

If the magnetoresistance is oscillating in time, meaning at least $\mathbf{m}_0 \cdot \mathbf{m}_1$ or $\mathbf{m}_1 \cdot \mathbf{m}_2$ is oscillating, we have an STO phase. If $\mathbf{m}_0 \cdot \mathbf{m}_1$ and $\mathbf{m}_1 \cdot \mathbf{m}_2$ are both constant, we have a canted phase. Note that if $\mathbf{m}_1$ and $\mathbf{m}_2$ oscillate in-phase in a plane perpendicular to $\mathbf{m}_0$, such that $\mathbf{m}_0 \cdot \mathbf{m}_1$ and $\mathbf{m}_1 \cdot \mathbf{m}_2$ are constant, we still have a canted phase and not an STO phase even though there are oscillations in the individual magnetization components. To confirm our analytical results, we will also later establish fully numerically when the STO phase occurs.

We now want to determine the physical effect that the Rashba spin–orbit coupling introduces by comparing it with other known terms. If we make the simplification of an equal polarization in the current causing the spin–orbit coupling in the free layers ($P_0 = P_1 = P$, $P_1^{(y)} = P_2^{(y)} = P$), this can be done without much effort. Note that for the bulk case it is not necessary to have the same polarization for both j_x and j_y, we could still achieve the same results with $P_1^{(y)} = P_2^{(y)} = P'$ by modifying α_R so that $\alpha_R P = \alpha_R' P'$. When performing this simplification in the polarization the matrix proportional to $\omega_R^{(x/y)}$ becomes very similar to the $\bar{A}$ matrix. The influence of RSOC is then to renormalize α and ω in the following manner:

$$\omega^* = \omega + \omega_R^{(x/y)} \frac{P}{1+\beta^2}, \tag{8a}$$

$$\alpha^* = \frac{\alpha\omega + \beta\omega_R^{(x/y)} \frac{P}{1+\beta^2}}{\omega + \omega_R^{(x/y)} \frac{P}{1+\beta^2}}. \tag{8b}$$

We note that the imaginary components of ω^* and ω are the same, as $\omega_R^{(x/y)}$ is entirely real. The stability of a phase was determined by the imaginary component of its eigenvalue, therefore any effect that RSOC may have on shifting the borders between a stable and an unstable region must be seen from α^*. As ω is in general complex, so is α^* (α, however, is real). It is also noted that the product $\alpha^*\omega^* = \alpha\omega + \omega_R^{(x/y)}P(1+\beta^2)^{-1}$ only has a shift in its real value. As ω and ω^* are complex and have the same imaginary component, the imaginary component of α^* must be non-zero if $\mathrm{Re}(\alpha^*) \neq \alpha$. This imaginary component of α^* ensures that the imaginary component of $\alpha\omega$ is invariant under the transformation to $\alpha^*\omega^*$, but is otherwise of little interest as α only appears in the product $\alpha\omega$. The effect of RSOC can then be found from the real part of α^*, which is found to be

$$\mathrm{Re}(\alpha^*) = \frac{\left(\alpha\mathrm{Re}(\omega) + \beta\omega_R^{(x/y)} \frac{P}{1+\beta^2}\right)\left(\mathrm{Re}(\omega) + \omega_R^{(x/y)} \frac{P}{1+\beta^2}\right) + \alpha\Im m(\omega)^2}{\left(\mathrm{Re}(\omega) + \omega_R^{(x/y)} \frac{P}{1+\beta^2}\right)^2 + \Im m(\omega)^2}. \tag{9}$$

There is no restriction on the sign of ω or $\omega_R^{(x/y)}$ ($\omega_R^{(y)}$ can for example be negative by switching the direction of the current j_y), and $\mathrm{Re}(\alpha^*)$ can as a consequence also take on negative values. The effect of RSOC can then be seen as a modification of the Gilbert damping parameter α, even to the extent where it takes on negative values and becomes an *anti-damping term* in the LLGS equation. We note that the modification α^* depends on the eigenvalues ω, which are complex functions of the system parameters. As the ansatz is a small perturbation from a collinear state, the modified value α^* is only valid in this state, and will change again in a manner that cannot be described by this framework if the perturbation is unstable and we move away from the collinear state. One special case that should be noted is when $\alpha = \beta$, for which $\mathrm{Re}(\alpha^*) = \alpha$. This predicts that when $\alpha = \beta$, RSOC has no impact on whether a collinear state is stable or not. When $\alpha \neq \beta$, $\mathrm{Re}(\alpha^*)$ has a maximum and a minimum when $\Im m(\omega) \neq 0$ and a singularity when $\Im m(\omega) = 0$. These extremal points are found from

$$\frac{\partial}{\partial\omega_R}\mathrm{Re}(\alpha^*) = -(\alpha-\beta)\frac{\Im m(\omega)^2\left(\mathrm{Re}(\omega) + 2\omega_R\frac{P}{1+\beta^2}\right) + \mathrm{Re}(\omega)\left(\mathrm{Re}(\omega) + \omega_R\frac{P}{1+\beta^2}\right)^2}{\left(\Im m(\omega)^2 + \left(\mathrm{Re}(\omega) + \omega_R\frac{P}{1+\beta^2}\right)^2\right)^2} = 0 \tag{10}$$

and are

$$\omega_R = -\left(\frac{1+\beta^2}{P}\right)\frac{\mathfrak{Im}(\omega)^2 \pm \mathfrak{Im}(\omega)\sqrt{\mathfrak{Im}(\omega)^2 + \mathfrak{Re}(\omega)^2} + \mathfrak{Re}(\omega)^2}{\mathfrak{Re}(\omega)}. \tag{11}$$

Which value is the maximum and minimum is determined by the sign of $\mathfrak{Re}(\omega)$, and whether $\beta > \alpha$ or $\beta < \alpha$. This means that if for our set of parameters we have $\mathfrak{Re}(\alpha^*) < \alpha$ for $\alpha > \beta$, we will have $\mathfrak{Re}(\alpha^*) > \alpha$ for the same set of parameters but with $\alpha < \beta$. Optimally we would like to have $\mathfrak{Re}(\alpha^*) < \alpha$ to increase the size of the STO phase, and we would also like to be able to have this for both $\alpha < \beta$ and $\alpha > \beta$. This can be controlled by the direction of the current responsible for the SOC, as we would then switch the minimum and maximum in $\mathfrak{Re}(\alpha^*)$. Switching the sign of ω_R will have a similar effect to switching between $\alpha < \beta$ and $\alpha > \beta$.

In the bulk geometry switching the sign of ω_R can easily be done by switching the direction of the current in the y-direction. In the thin film geometry this may not have the desired effect, as the current controlling the strength of RSOC is also intertwined with the strength of the STT and by switching the direction of j_x we will also change the value of ω. The phase diagrams obtained numerically in the next section, determining when the STO phase occurs, are consistent with these analytical considerations of the role played by RSOC.
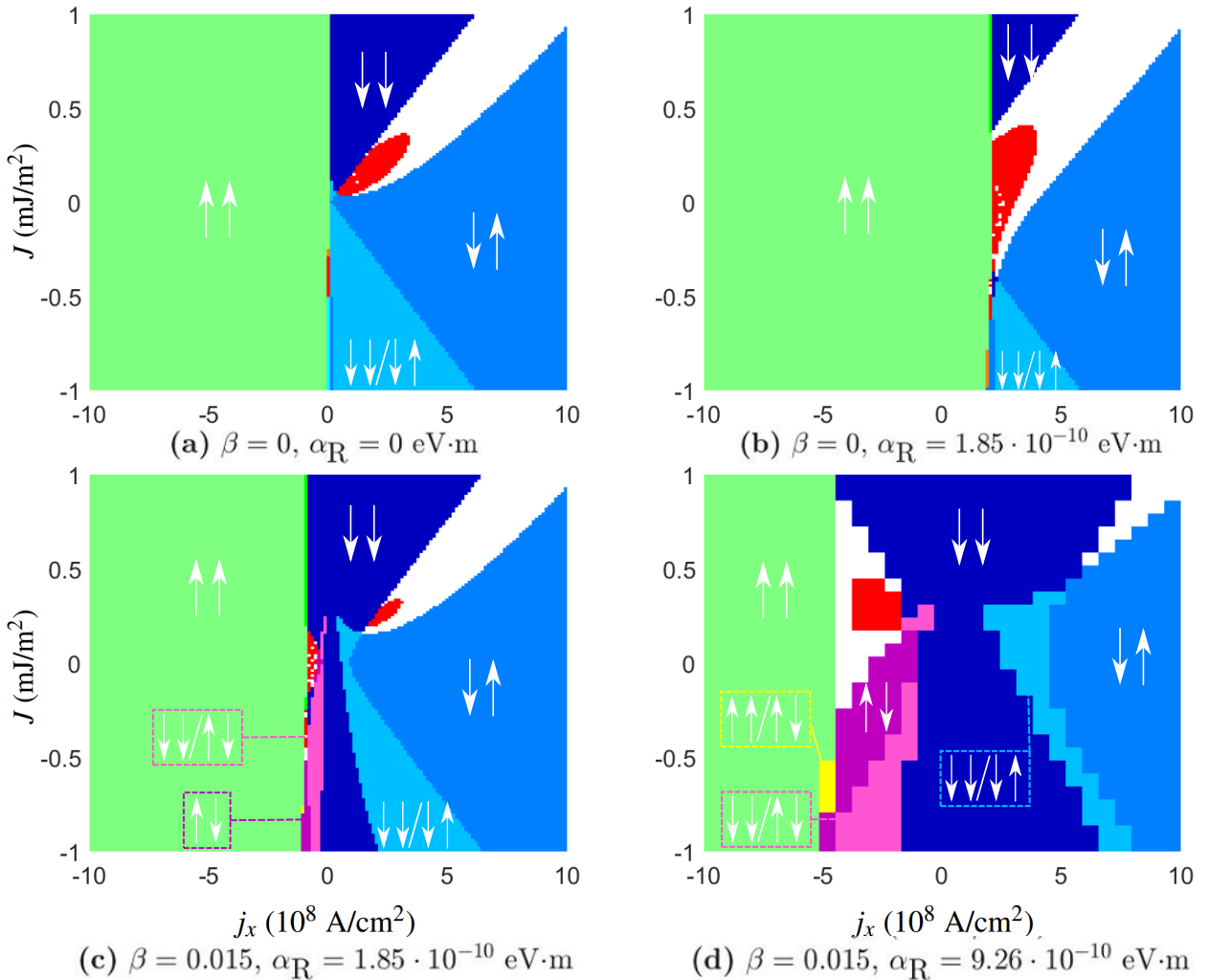
Figure 2. Phase diagrams for the bulk geometry. For all phase diagrams the values $\alpha = 0.01$, $P = 0.5$, $j_y = 10^9$ A/cm^2, $K = 8 \cdot 10^4$ J/m^3, $d = 3$ nm are assumed. The red regions indicate an STO phase, while the white regions are canted states.

Results

Based on the results presented so far, we will now calculate the phase diagrams to determine when the different collinear states are stable. This is done by solving (5) for all combinations of λ_1 and λ_2, and checking the sign of the imaginary component of ω. In addition, to be able to separate the STO and canted phase from one another, we solve the LLGS equation numerically and analyze the results. We classify the system to be in an STO state if the variance of the latter part of the solution is above some minimal value (set to be 10^{-6} per time unit), and that the variance does not decrease faster than a cutoff factor (set to be 0.9). For an easy comparison to previous results, we use the same set of parameters as Zhou *et al.*[18] for our simulations, but additionally include the effect of spin–orbit torques. These parameters are $\alpha = 0.01$, $P = 0.5$, $K = 8 \cdot 10^4$ J/m^3, $d = 3$ nm, $J \sim 1$ mJ/m^2, $j_x \sim 10^8$ A/cm^2, $M_s = 127$ kA/m. We will also perform fast Fourier transforms of the numerical solution along given lines in the phase diagram, to analyze the effects of RSOC on the frequency spectrum.
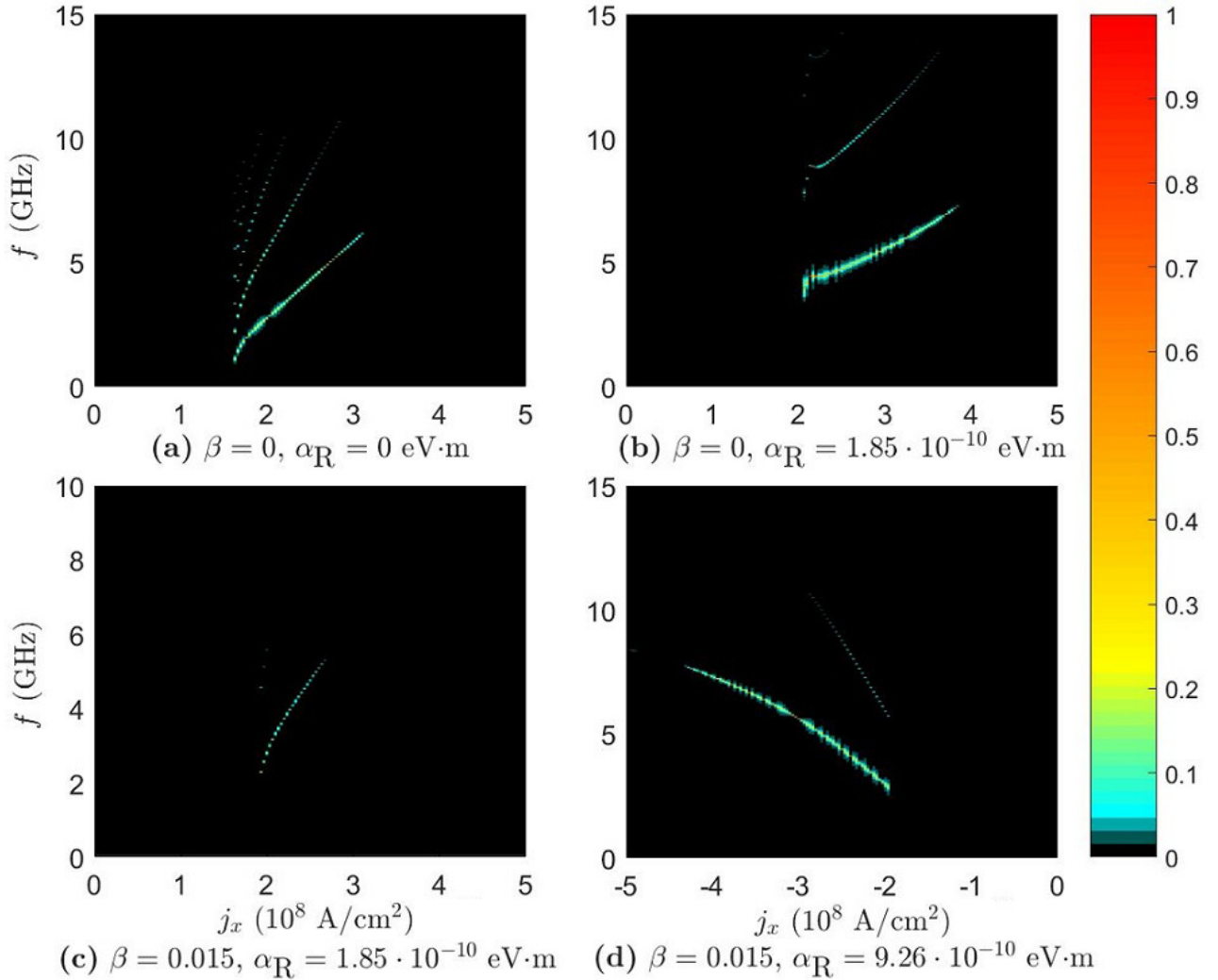
Figure 3. The one sided spectra of the Fourier transform of $\mathbf{m}_0 \cdot \mathbf{m}_1$ in the bulk geometry. The Fourier transform was taken along the $J = 0.25$ mJ/m^2 line in the phase diagrams.

Bulk geometry

A combination of the analytical and numerical calculations yield the results shown in Figure 2 for the bulk geometry. We have here used a current density $j_y = 10^9$ A/cm^2 that is responsible for the SOC. The strength of the Rashba-parameter α_R is chosen large enough to have considerable impact, but kept at a realistic order of magnitude. As an example, α_R has been found to be $\sim 3.7 \cdot 10^{-10}$ eV·m at the surface of Bi/Ag alloy.[23] The value $\alpha_R = 9.26 \cdot 10^{-10}$ eV·m exceeds this value and thus corresponds to a rather large value of the Rashba-parameter. For the bulk geometry this is of no concern, as we can achieve the same results

for lower values of α_R by increasing the current density j_y, but this is not possible in the thin film geometry where spin-transfer torques and RSOC can not be separated in the same manner.

To benchmark our numerical results, we reproduce the phase diagram found by Zhou *et al.* in the absence of spin–orbit interactions in Figure 2a. When Rashba spin–orbit coupling is present, it is seen from Figure 2b that the STO phase becomes larger. In addition, the STO phase also extends into the antiferromagnetic regime ($J < 0$), and even occurs in the absence of any RKKY interaction between $\mathbf{m}_1$ and $\mathbf{m}_2$ ($J = 0$). In the article by Zhou *et al.*, the border between the unstable region (STO and canted phases) and the $\uparrow\downarrow$ state was found to be approximately

$$\omega_J = \sqrt{4\omega_0^2 + \left(\omega_j^{(x)}\right)^2} - 2\omega_0 + \alpha \frac{\omega_0^2}{\omega_j^{(x)}}. \tag{12}$$

The effect of the term proportional to α can be seen by the slight increase of the border between the unstable region and the $\uparrow\downarrow$ state as $j_x \to 0^+$ in Figure 2a. In Figure 2b, however, the border decreases as $j_x \to 0^+$. This is in agreement with what we have discussed earlier, namely that the effect of RSOC in the present system is equivalent to a modification of the Gilbert damping, even to the extent where it takes on negative values. This seems to be the case in this phase diagram where $\mathrm{Re}(\alpha^*)$ becomes minimal when $\beta < \alpha$. We also predicted above that one could move from $\mathrm{Re}(\alpha^*) < \alpha$ to $\mathrm{Re}(\alpha^*) > \alpha$ by letting $\beta > \alpha$, assuming $\mathrm{Re}(\alpha^*) < \alpha$ for $\beta < \alpha$. This is illustrated in Figure 2c and 2d, where the border between the unstable region and the $\uparrow\downarrow$ state is lifted with respect to the border in Figure 2a. The size of the STO phase also decreases in this maximal region of $\mathrm{Re}(\alpha^*)$ ($\mathrm{Re}(\alpha^*) > \alpha$), which is not an unexpected consequence from an increase in the Gilbert damping. This does not mean that cases where $\beta > \alpha$ are of no interest, however. As noted, we are able to move back to a minimal region of $\mathrm{Re}(\alpha^*)$ in the bulk geometry by switching the direction of the current applied in the y-direction.

Moving on to the frequency spectrum of the STO phase in the presence of RSOC, we consider fast Fourier transforms of the quantity $\mathbf{m}_0 \cdot \mathbf{m}_1$ along the $J = 0.25$ mJ/m^2 line in the phase diagrams. These results are presented in Figure 3. The fast Fourier transforms of $\mathbf{m}_1 \cdot \mathbf{m}_2$ are not presented as they show the same frequency spectrum as $\mathbf{m}_0 \cdot \mathbf{m}_1$, but with different amplitudes. The system with RSOC has fewer frequencies, as can be seen by comparing Figure 3a and 3b. In addition, the oscillations in the system with RSOC can have a higher amplitude than the system without RSOC, as illustrated in Figure 3b and 3d. It is also seen that the presence of RSOC allows us to achieve slightly different frequency outputs than a system without RSOC. This will increase the tunability of the spin torque oscillator, as we can also adjust the strength of the RSOC via j_y, in addition to the modulation of the frequency via j_x and the anisotropy strength K as done in Ref.[18]

Thin film geometry

(a) $\beta = 0$, $\alpha_R = 9.26 \cdot 10^{-10}$ eV·m

(b) $\beta = 0.005$, $\alpha_R = 9.26 \cdot 10^{-10}$ eV·m
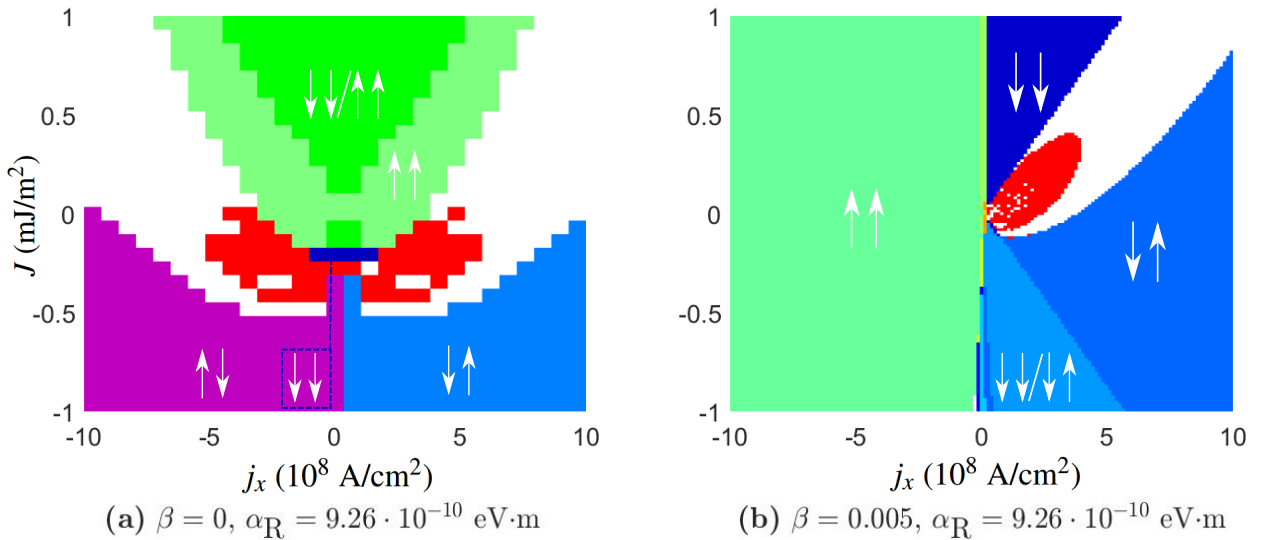
Figure 4. Phase diagrams for the thin film geometry. For all phase diagrams the values $\alpha = 0.01$, $P = 0.5$, $K = 8 \cdot 10^4$ J/m^3, $d = 3$ nm are assumed. The red regions indicate an STO phase, while the white regions are canted states.

In the thin film geometry, both the spin-transfer torques and spin–orbit coupling are controlled by the same current j_x. This gives us a different behavior than the one in the bulk geometry, as seen in Figure 4. For low values of α_R the behavior
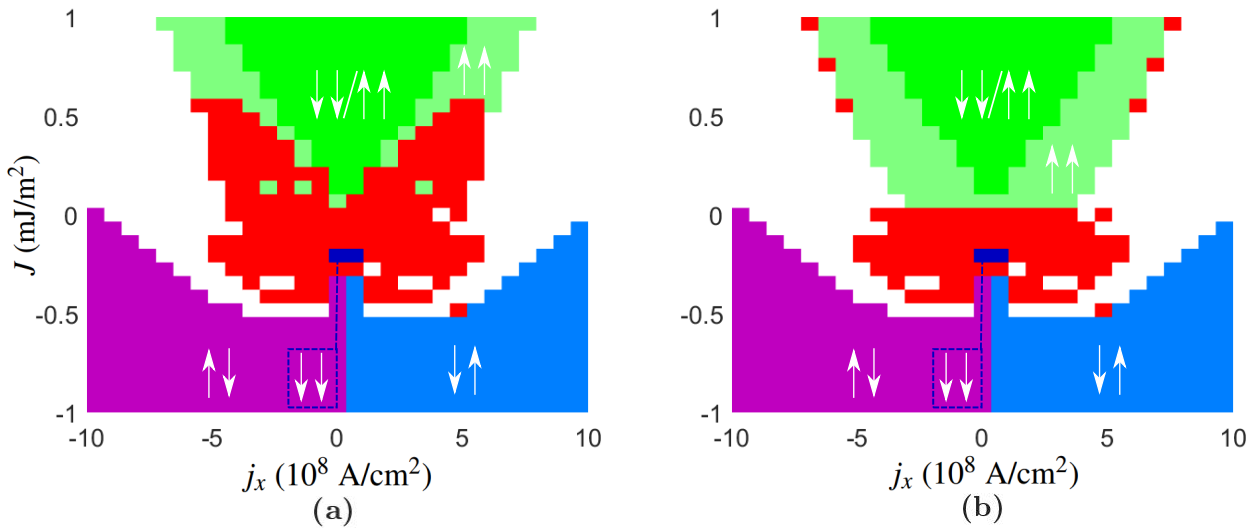
is quite similar to a system without RSOC, but as we increase α_R interesting effects appear. When we let $\alpha_R = 9.26 \cdot 10^{-10}$ eV·m and $\beta = 0$, we get the phase diagram shown in Figure 4a. In this phase diagram the STO phase is symmetric in j_x, and the STO phase is located in the antiferromagnetic regime ($J < 0$). When we let $\beta = \alpha/2 = 0.005$ the phase diagram becomes similar to the case without any RSOC again, but there is still a significant increase in the STO phase which extends into the antiferromagnetic regime. The decrease in the border between the unstable region and the ↑↓ state as $j_x \rightarrow 0^+$ is also not existent in the thin film geometry, as the effects of RSOC are proportional to j_x.

The STO phase in Figure 4 (and Figure 2) is only registered where there are no stable collinear states according to the analytical calculations, as we only want to classify a state as being STO if there is not a possibility of the system stabilizing in a collinear state. The stability of the collinear states are determined analytically, while the STO phase is found numerically. If we include all the points the numerical calculations registered as being an STO phase, even at points where the analytical calculations show one or more collinear states to be stable, the phase diagrams become like the ones shown in Figure 5

We see that the STO phase also extends into the region where ↑↑ is a stable state when the initial state is not close to this state. It is therefore also possible to get an STO phase in the ferromagnetic regime for this case, depending on the initial state of $\mathbf{m}_1$ and $\mathbf{m}_2$. The reason why the initial state does not relax to the ↑↑ state even if this is a stable solution can be seen from the size of the imaginary component of ω in this region. While the imaginary component of ω belonging to ↑↑ in this region is negative, its magnitude is only 10^{-2}. In comparison the other collinear states have an imaginary component ranging up to a magnitude of 10^1. If $\mathbf{m}_1$ and $\mathbf{m}_2$ are not close to being in the ↑↑ state initially, it is therefore not given that they will relax to this state, and can end up in an oscillating or canted state.

This sensitivity issue concerning the initial state of $\mathbf{m}_1$ and $\mathbf{m}_2$ was only of considerable significance for the ↑↑ state in the thin-film geometry with $\beta = 0$, $\alpha_R = 9.26 \cdot 10^{-10}$ eV·m. There was also some sensitivity for other phase diagrams in the limit $j_x \rightarrow 0$. Regarding the cutoff factors utilized for classifying the numerical solution, there was very little sensitivity with regard to the choice of parameters. The transitional region between an STO state and a canted or collinear state is found to happen on a typical scale of 10^6 A/cm^2 or 10^{-3} mJ/m^2, both of which being very small compared to the magnitude of the parameters considered. As the cutoff factors would primarily have an effect in this transitional region, a change in these parameters would not lead to a significant change in the size of the STO phase. It can also be seen in some of the phase diagrams that there are found to be some canted states in the middle of the STO region, or a single STO state separated from the main STO region. This is discovered to be due to the time interval the system is solved over, as for some parameters it takes longer time for the system to obtain stable oscillations than for others. The time scale that the system was solved over was constrained to some degree, due to the run-time of the solver. It is also observed that the initial state of $\mathbf{m}_1$ and $\mathbf{m}_2$ has some impact on how fast these oscillations become stable. When solving the system over a longer time scale the STO regions should become more or less continuous.

Figure 5. The stability of the ↑↑ state in the thin film geometry for $\beta = 0$, $\alpha_R = 9.26 \cdot 10^{-10}$ eV·m is found to be very dependent on the initial conditions. In **(a)** the initial state is chosen to be close to ↓↓ for $J > 0$, while in **(b)** the initial state is chosen to be close to ↑↑ in the same region. In both cases the initial state is chosen to be close to ↓↑ for $J < 0$.

When considering the frequency spectrum of the STO phase in the thin film geometry in Figure 6 we see that the spectrum of

(a) $\beta = 0$, $\alpha_R = 9.26 \cdot 10^{-10}$ eV·m (b) $\beta = 0.005$, $\alpha_R = 9.26 \cdot 10^{-10}$ eV·m
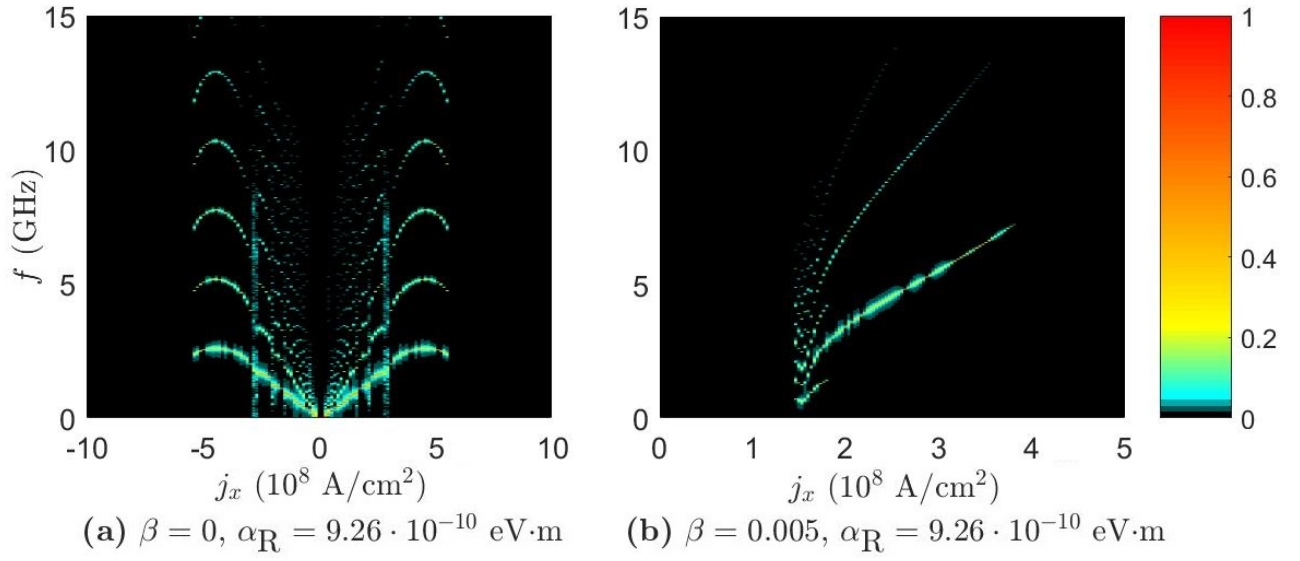
Figure 6. The one sided spectra of the Fourier transform of $\mathbf{m}_0 \cdot \mathbf{m}_1$ in the thin film geometry. The Fourier transform was taken along the $J = -0.2$ mJ/m^2 line in **(a)** and along $J = 0.25$ mJ/m^2 in **(b)**.

the $\alpha_R = 9.26 \cdot 10^{-10}$ eV·m, $\beta = 0$ case shows the same symmetry in j_x as the phase diagram. Moreover, the antiferromagnetic STO phase has a larger set of frequencies than what has been found in the ferromagnetic STO phase and is also, unlike the other plots, symmetric in j_x. When increasing β to 0.005 and considering the frequency spectrum in the ferromagnetic regime, the result is more similar to the bulk geometry case, as seen in Figure 6b. We have fewer and more slowly varying frequencies as a function of j_x, but the amplitude of the oscillations are higher.

Conclusion

We have shown how Rashba spin–orbit coupling can be used to substantially increase the size of the spin torque oscillator phase in both ferromagnetically and antiferromagnetically coupled compensated magnetic moments in a bilayer system. This presumably allows for a better tunability of the frequency output of the oscillator, as the spin–orbit coupling torques can be controlled electrically.

References

1. Slonczewski, J. Current-driven excitation of magnetic multilayers. *Journal of Magnetism and Magnetic Materials* **159**, L1 – L7 (1996). URL http://www.sciencedirect.com/science/article/pii/0304885396000625.

2. Berger, L. Emission of spin waves by a magnetic multilayer traversed by a current. *Phys. Rev. B* **54**, 9353–9358 (1996). URL http://link.aps.org/doi/10.1103/PhysRevB.54.9353.

3. Tsoi, M. *et al.* Excitation of a magnetic multilayer by an electric current. *Phys. Rev. Lett.* **80**, 4281–4284 (1998). URL http://link.aps.org/doi/10.1103/PhysRevLett.80.4281.

4. Myers, E. B., Ralph, D. C., Katine, J. A., Louie, R. N. & Buhrman, R. A. Current-induced switching of domains in magnetic multilayer devices. *Science* **285**, 867–870 (1999). URL http://science.sciencemag.org/content/285/5429/867. http://science.sciencemag.org/content/285/5429/867.full.pdf.

5. Sun, J. Current-driven magnetic switching in manganite trilayer junctions. *Journal of Magnetism and Magnetic Materials* **202**, 157 – 162 (1999). URL http://www.sciencedirect.com/science/article/pii/S0304885399002899.

6. Katine, J. A., Albert, F. J., Buhrman, R. A., Myers, E. B. & Ralph, D. C. Current-driven magnetization reversal and spin-wave excitations in Co /Cu /Co pillars. *Phys. Rev. Lett.* **84**, 3149–3152 (2000). URL http://link.aps.org/doi/10.1103/PhysRevLett.84.3149.

7. Åkerman, J. Toward a universal memory. *Science* **308**, 508–510 (2005). URL http://science.sciencemag.org/content/308/5721/508. http://science.sciencemag.org/content/308/5721/508.full.pdf.

8. Katine, J. & Fullerton, E. E. Device implications of spin-transfer torques. *Journal of Magnetism and Magnetic Materials* **320**, 1217 – 1226 (2008). URL http://www.sciencedirect.com/science/article/pii/S0304885307010189.

9. Parkin, S. S. P., Hayashi, M. & Thomas, L. Magnetic domain-wall racetrack memory. *Science* **320**, 190–194 (2008). URL http://www.sciencemag.org/content/320/5873/190.abstract. http://www.sciencemag.org/content/320/5873/190.full.pdf.

10. Tsoi, M. *et al.* Generation and detection of phase-coherent current-driven magnons in magnetic multilayers. *Nature* **406**, 46–48 (2000). URL http://dx.doi.org/10.1038/35017512.

11. Kiselev, S. I. *et al.* Microwave oscillations of a nanomagnet driven by a spin-polarized current. *Nature* **425**, 380–383 (2003). URL http://dx.doi.org/10.1038/nature01967.

12. Rippard, W. H., Pufall, M. R., Kaka, S., Russek, S. E. & Silva, T. J. Direct-current induced dynamics in $co_{90}fe_{10}/ni_{80}fe_{20}$ point contacts. *Phys. Rev. Lett.* **92**, 027201 (2004). URL http://link.aps.org/doi/10.1103/PhysRevLett.92.027201.

13. Baibich, M. N. *et al.* Giant magnetoresistance of (001)fe/(001)cr magnetic superlattices. *Phys. Rev. Lett.* **61**, 2472–2475 (1988). URL http://link.aps.org/doi/10.1103/PhysRevLett.61.2472.

14. Binasch, G., Grünberg, P., Saurenbach, F. & Zinn, W. Enhanced magnetoresistance in layered magnetic structures with antiferromagnetic interlayer exchange. *Phys. Rev. B* **39**, 4828–4830 (1989). URL http://link.aps.org/doi/10.1103/PhysRevB.39.4828.

15. Silva, T. & Rippard, W. Developments in nano-oscillators based upon spin-transfer point-contact devices. *Journal of Magnetism and Magnetic Materials* **320**, 1260 – 1271 (2008). URL http://www.sciencedirect.com/science/article/pii/S0304885307010153.

16. Sun, J. & Ralph, D. Magnetoresistance and spin-transfer torque in magnetic tunnel junctions. *Journal of Magnetism and Magnetic Materials* **320**, 1227 – 1237 (2008). URL http://www.sciencedirect.com/science/article/pii/S0304885307010177.

17. Klein, C., Petitjean, C. & Waintal, X. Interplay between nonequilibrium and equilibrium spin torque using synthetic ferrimagnets. *Phys. Rev. Lett.* **108**, 086601 (2012). URL http://link.aps.org/doi/10.1103/PhysRevLett.108.086601.

18. Zhou, Y., Xiao, J., Bauer, G. E. W. & Zhang, F. C. Field-free synthetic-ferromagnet spin torque oscillator. *Phys. Rev. B* **87**, 020409 (2013). URL http://link.aps.org/doi/10.1103/PhysRevB.87.020409.

19. Cheng, R., Xiao, D. & Brataas, A. Terahertz antiferromagnetic spin hall nano-oscillator. *Phys. Rev. Lett.* **116**, 207603 (2016).

20. Bychkov, Y. A. & Rashba, E. I. Oscillatory effects and the magnetic susceptibility of carriers in inversion layers. *Journal of Physics C: Solid State Physics* **17**, 6039 (1984). URL http://stacks.iop.org/0022-3719/17/i=33/a=015.

21. Heide, M., Bihlmayer, G., Mavropoulos, P., Bringer, A. & Blügel, S. Spin–orbit driven physics at surfaces. *Newsletter of the Psi-K Network* **78** (2006). URL www.psi-k.org/newsletters/News_78/Highlight_78.pdf.

22. Mihai Miron, I. *et al.* Current-driven spin torque induced by the rashba effect in a ferromagnetic metal layer. *Nat Mater* **9**, 230–234 (2010). URL http://dx.doi.org/10.1038/nmat2613.

23. Manchon, A., Koo, H. C., Nitta, J., Frolov, S. M. & Duine, R. A. New perspectives for rashba spin-orbit coupling. *Nat Mater* **14**, 871–882 (2015). URL http://dx.doi.org/10.1038/nmat4360. Review.

24. Schultz, M. *et al.* Rashba spin splitting in a gated hgte quantum well. *Semiconductor Science and Technology* **11**, 1168 (1996). URL http://stacks.iop.org/0268-1242/11/i=8/a=009.

25. Nitta, J., Akazaki, T., Takayanagi, H. & Enoki, T. Gate control of spin-orbit interaction in an inverted $in_{0.53}ga_{0.47}as/in_{0.52}al_{0.48}as$ heterostructure. *Phys. Rev. Lett.* **78**, 1335–1338 (1997). URL http://link.aps.org/doi/10.1103/PhysRevLett.78.1335.

26. Miron, I. M. *et al.* Perpendicular switching of a single ferromagnetic layer induced by in-plane current injection. *Nature* **476**, 189–193 (2011). URL http://dx.doi.org/10.1038/nature10309.

27. Kim, K.-W., Seo, S.-M., Ryu, J., Lee, K.-J. & Lee, H.-W. Magnetization dynamics induced by in-plane currents in ultrathin magnetic nanostructures with Rashba spin-orbit coupling. *Phys. Rev. B* **85**, 180404 (2012). URL http://link.aps.org/doi/10.1103/PhysRevB.85.180404.

28. Khvalkovskiy, A. V. *et al.* Matching domain-wall configuration and spin-orbit torques for efficient domain-wall motion. *Phys. Rev. B* **87**, 020402 (2013). URL http://link.aps.org/doi/10.1103/PhysRevB.87.020402.

29. Obata, K. & Tatara, G. Current-induced domain wall motion in rashba spin-orbit system. *Phys. Rev. B* **77**, 214429 (2008). URL http://link.aps.org/doi/10.1103/PhysRevB.77.214429.

30. Haney, P. M. & Stiles, M. D. Current-induced torques in the presence of spin-orbit coupling. *Phys. Rev. Lett.* **105**, 126602 (2010). URL http://link.aps.org/doi/10.1103/PhysRevLett.105.126602.

31. Ryu, J., Seo, S.-M., Lee, K.-J. & Lee, H.-W. Rashba spin–orbit coupling effects on a current-induced domain wall motion. *Journal of Magnetism and Magnetic Materials* **324**, 1449 – 1452 (2012). URL http://www.sciencedirect.com/science/article/pii/S0304885311008559.

32. Linder, J. Chirality-sensitive domain wall motion in spin-orbit coupled ferromagnets. *Phys. Rev. B* **87**, 054434 (2013). URL http://link.aps.org/doi/10.1103/PhysRevB.87.054434.

33. van der Bijl, E. & Duine, R. A. Current-induced torques in textured rashba ferromagnets. *Phys. Rev. B* **86**, 094406 (2012). URL http://link.aps.org/doi/10.1103/PhysRevB.86.094406.

34. Hals, K. M. D. & Brataas, A. Phenomenology of current-induced spin-orbit torques. *Phys. Rev. B* **88**, 0Loading...85423 (2013). URL http://link.aps.org/doi/10.1103/PhysRevB.88.085423.

35. Kim, K.-J. *et al.* Electric control of multiple domain walls in pt/co/pt nanotracks with perpendicular magnetic anisotropy. *Applied Physics Express* **3**, 083001 (2010). URL http://stacks.iop.org/1882-0786/3/i=8/a=083001.

36. Linder, J. & Alidoust, M. Asymmetric ferromagnetic resonance, universal walker breakdown, and counterflow domain wall motion in the presence of multiple spin-orbit torques. *Phys. Rev. B* **88**, 064420 (2013). URL http://link.aps.org/doi/10.1103/PhysRevB.88.064420.

37. Ado, I. A., Tretiakov, O. A. & Titov, M. Microscopic theory of spin-orbit torques applied to skyrmion dynamics. *arXiv:1603.07994* (2016).

38. Duan, Z. *et al.* Nanowire spin torque oscillator driven by spin orbit torques. *Nat Commun* **5** (2014). URL http://dx.doi.org/10.1038/ncomms6616. Article.

39. Ralph, D. & Stiles, M. Spin transfer torques. *Journal of Magnetism and Magnetic Materials* **320**, 1190 – 1216 (2008). URL http://www.sciencedirect.com/science/article/pii/S0304885307010116.

Acknowledgements

Author contributions statement

Ø.J. did the analytical and numerical calculations with support from J.L. Both authors contributed to the discussion of the results and the writing of the manuscript.

Additional information

Competing financial interests The authors declare no competing financial interests.